WAKE OF HORIZONTAL AXIS TIDAL-CURRENT TURBINE AND ITS EFFECTS ON SCOUR

CHEN LONG

THESIS SUBMITTED IN FULFILLMENTS OF THE REQUIREMENTS FOR THE DEGREE OF DOCTOR OF PHILOSOPHY

FACULTY OF ENGINEERING
UNIVERSITY OF MALAYA
KUALA LUMPUR
2017

UNIVERSITY OF MALAYA

ORIGINAL LITERARY WORK DECLARATION

Name of Candidate   : Chen Long
Registration / Matric No   : KHA130150
Name of Degree   : DOCTOR OF PHILOSOPHY
Title of Thesis ("this Work"):

WAKE OF HORIZONTAL AXIS TIDAL-CURRENT TURBINE AND ITS EFFECTS ON SCOUR

Field of Study: Water Resource Engineering

I do solemnly and sincerely declare that:

1) I am the sole author/ writer of this Work;
2) This work is original;
3) Any use of any work in which copyright exists was done by way of fair dealing and permitted purposes and any excerpt or extract from, or reference to or reproduction of any copyright work has been disclosed exxpressly and suffciently and the title of the Work and its authorship have been acknowledge in this Work;
4) I do not have any actual knowledge nor do I ought resonable to know that the the making of this work consititutes an infringement of any copoyright work;
5) I hereby assign all and every rights in the copyright of this Work to the University of Malaya ("UM"), who henceforth shall be owner of the copyright in this Work and that any reprodcution or use in any form or by ant means whatsoever is prohibited without the written consent of UM having been first had and obtained;
6) I am fully aware that if in the course of making this Work I have infringed any copyright whether intentionally or otherwise, I may be subject to legal action or any other action as may be determined by UM.

 Candidate's Signature   Date

Subscribed and solemnly declare before,

 Witness's Signature   Date

Name:
Designation:

ABSTRACT

Many large scale tidal current turbines (TCTs) have been tested and deployed around the world. It is foreseeable that tidal current will be a vital natural resource in future energy supplies. The wake generated from the TCT amplifies the scour process around the support structure. It causes sediment transport at the seabed and it may result in severe environmental impacts. The study aims to investigate the generated wake and its effects on the scour process around the support structure of the TCT. An analytical wake model is proposed to predict the initial velocity and its lateral distribution downstream of the TCT. The analytical wake model consists of several equations derived from the theoretical works of ship propeller jets. Axial momentum theory is used to predict the minimum velocity at the immediate plane of the wake and followed by recovery equation to determine the minimum velocity at lateral sections along the downstream of the wake. Gaussian distribution is applied to predict the lateral velocity distribution in a wake. The proposed model is also able to predict wake structure under various ambient turbulence conditions (TI= 3%, 5%, 8% and 15%). The proposed wake model is validated by comparing the results with well-accepted experimental measurements. Goodness-of-fit analysis has been conducted by using the estimator of R-square (R2) and Mean Square Error (MSE). The R2 and MSE are in the range of 0.1684 − 0.9305 and 0.004 − 0.0331, respectively. A TCT model was incorporated in OpenFOAM to simulate the flow between rotor and seabed due to the fact that the flow is responsible for the sediment transport. The axial component of velocity is the dominating velocity of the flow below the TCT. The maximum axial velocity under the turbine blades is around 1.07 times of the initial incoming flow. The

maximum radial and tangential velocity components of the investigated layer are approximately 4.12% and 0.22% of the maximum axial velocity. The acceleration of flow under the rotor changes seabed boundary layer profile. The geometry of the turbine also affects the flow condition. Results showed that the velocity increases with the number of blades. Both the axial and radial velocities were significantly influenced by the number of blades, the tangential velocity was found to be insignificant. A physical model of TCT is placed in a hydraulic flume for scour test. The scour rate of the fabricated model was investigated. The decrease of tip clearance increases the scour depth. The shortest tip clearance results in the fastest and most sediment transport. The maximum scour depth reached approximately 18.5% of rotor diameter. Experimental results indicated that regions susceptible to scour typically persist up to $1.0D_t$ downstream and up to $0.5D_t$ to either side of the turbine support centre. The majority of the scour occurred in the first 3.5 hr. The maximum scour depth reaches equilibrium after 24 hr test. The study correlated scour depth of the TCT with the tip clearance. An empirical formula has been proposed to predict the time-dependent scour depth of the pile-supported TCT.

ABSTRAK

Turbin semasa pasang surut (TCT) yang berskala besar telah banyak diuji dan digunakan seluruh dunia. Boleh diramalkan bahawa tenaga berpunca daripada pasang surut laut akan menjadi satu sumber semula jadi yang penting bagi bekalan tenaga pada masa yang akan datang. Ekoran air yang dihasilkan oleh TCT menggandakan proses kerokan di sekeliling struktur sokongan. Ini menyebabkan pengangkutan sedimen pada dasar laut dan boleh menyebabkan impak alam sekitar yang teruk. Satu model analitikal telah dihasilkan untuk menjangka halaju permulaan dan pengedaran hala di hiliran TCT. Model analitikal ini terdiri daripada beberapa formula yang diperolehi daripada teori jet kincir kapal. Teori momentum digunakan untuk manjangka halaju minima di satah segera *lee wake* dan diikuti dengan persamaan pemulihan untuk menentukan halaju minima di seksyen sisian sepanjang hiliran ekoran air. Pengedaran Gaussian digunakan untuk menjangka halaju sisian dalam satu wake. Model yang dihasilkan berupaya untuk menjangka struktur ekoran air bagi pelbagai keadaan turbulen (TI= 3%, 5%, 8% dan 15%). Model yang dihasilkan telah divalidasi dengan membanding keputusan yang diperoleh dengan eksperimen. Alanisa *Goodness-of-fit* telah dibuat dengan menggunakan jangkaan Kuasa Dua R (R2) dan Ralat Min Kuasa Dua (MSE). R2 dan MSE adalah dalam julat 0.1684-0.9305 dan 0.004-0.0331. Satu model TCT telah dimasukkan dalam OpenFOAM untuk mensimulasikan aliran di antara pemutar dan dasar laut kerana aliran merupakan factor yang mempengaruhi pengakutan sedimen. Halaju komponen paksi-x merupakan halaju dominan di bawah turbin arus laut. Halaju paksi-x maxima di bawah bilah turbine adalah serata 1.07 kali aliran permulaan. Komponen had laju jejarian dan halaju tangen

maxima bagi lapisan yang dikaji adalah lebih kurang 4.12% dan 0.22% had laju paksi-x maxima. Aliran berubah secara berkadar langsung dengan halaju aliran permulaan. Pecutan aliran di bawah pemutar mengubahkan profil lapisan sempadan dasar laut. Geometri turbin juga mempengaruhi keadaan aliran. Keputusan menunjukkan bahawa halaju meningkat dengan bilangan bilah. Kedua-dua halaju paksi-x dan jejarian dipengaruhi dengan ketara oleh bilangan bilah, dan halaju tangen pula didapati tidak akan dipengaruhi secara ketara. Satu model TCT fisikal telah diletakkan dalam satu flum untuk menguji kerokan. Kadar kerokan bagi model ini telah dikaji dalam flum tersebut. Pengurangan kelegaan hujung meningkatkan kedalaman kerokan. Kelegaan hujung yang paling kecil menyebabkan pengangkutan sedimen yang paling banyak dan cepat. Kedalaman kerokan maxima mencapai 18.5% diameter pemutar. Keputusan ini menunjukkan kawasan yang terdedah kepada kerokan adalah berkadar langsung dengan diameter turbin, dan biasanya berterusan sehingga $1.0D_t$ di hilir dan $0.5D_t$ di sebelah pusat sokongan turbin. Kebanyakan kerokan wujud dalam 3.5 jam pertama. Kedalaman kerokan mencapai keseimbangan selepas 24 jam ujian. Kajian ini adalah untuk mengaitkan kedalaman kerokan TCT dengan kelegaan hujung. Satu formula empirikal untuk menjangka kedalaman kerokan bergantung kepada masa bagi TCT yang disokong oleh cerucuk telah dicadangkan.

ACKNOWLEDGEMENTS

TABLE OF CONTENTS

LIST OF FIGURES

LIST OF TABLES

LIST OF SYMBOLS AND ABBREVIATIONS

A	Area of actuator disc
a	Pier width/diameter
b	Flume width
c	Wake growth factor
C	Tip clearance
C_T	Thrust coefficient
D	Width/diameter of pile/pier
D_t	Diameter of the turbine disc
D_p	Diameter of the propeller
E_o	Hashimi efflux coefficient
F_r	Froude number of incoming flow
F_o	Densimetric Froude number
I	Turbulence intensity
U_1	Axial velocity in at location 1
U_2	Axial velocity in at location 2
U_3	Axial velocity in at location 3
U_4	Axial velocity in at location 4
V_a	Axial velocity
V_o	Efflux velocity
V_∞	Free stream velocity
V_{max}	Maximum lateral distribution velocity
V_{min}	Minimum axial velocity
$V_{x,r}$	Lateral distribution velocity
V_a	Axial velocity
V_r	Radial velocity
V_t	Tangential velocity
x	Longitudinal /downstream distance
y	Lateral (spanwise) distance
n	Rotational speed in rev/s
P_1	Pressure in Pa at location 1
P_2	Pressure in Pa at location 2
P_3	Pressure in Pa at location 3
P_4	Pressure in Pa at location 4
r	Radial distance in metres
R_t	Radius of turbine rotor
R_p	Radius of propeller
Re_D	Reynolds number
R_{mo}	Location of efflux velocity from rotational axis
S	Scour Depth
S_t	Scour depth at time t
T	Thrust in Newton
Tw	Wave period of incoming flow in seconds
K_s	Correction factor of pier shape

K_θ	Correction factor of flow angle
K_b	Correction factor of bed condition
K_d	Correction factor for size of bed material
K_y	Correction factor for flow depth
K_σ	Correction factor for sediment grading
K_β	Correction factor for pier alignment
K_I	Correction factor for flow intensity
K_G	Correction factor for channel geometry
K_w	Correction factor for pier with/ pile diameter
K_v	Correction factor accounting for wave action
K_h	Correction factor accounting for piles that do not extend over the entire water column
u_f	Approach shear velocity
u_{cr}	Critical shear velocity
U_{cr}	Threshold depth averaged current velocity
U_c	Depth averaged current velocity
U_{uc}	Undisturbed current velocity
U_m	Maximum value of the undisturbed orbital velocity at the sea bottom
R_b	Bulk Reynold number
R_T	Turbine rotor Reynolds number
R_{eD}	Pile Reynold numb*er*
$R_{e\delta}$	Boundary layer Reynolds number
Q_w	Flow discharge
U	Velocity at the edge of the bed boundary layer
v	Kinematic viscosity of water
θ	Angle of attack
L	Pier length
h	Flow depth
h_p	Pile height
I_x	x-component of turbulence intensity
I_y	y-component of turbulence intensity
I_z	z-component of turbulence intensity
I	Turbulence intensity
u'	x-components of turbulence
v'	y-components of turbulence
w'	z-components of turbulence
V_{ref}	Reference mean velocity
ξ	Stewart efflux coefficient
ε_m	Maximum depth of scour
δ	Blockage ratio
d_{16}	Sediment size is 16% finer by weight
d_{50}	Median sediment grain size
d_{84}	Sediment size is 84% finer by weight
g	Acceleration due to gravity
σ_g	Geometric standard deviation of sediment particles
$\Delta\rho$	Difference between the mass density of the sediment and the fluid

ρ	Density of fluid
ρ_w	Density of water
ρ_s	Density of sand
μ_t	Turbulent viscosity
C_μ	Empirical constant
f_i	Predicted value
y_{av}	Mean of measured value
y_i	Measured value
w_i	Weighting applied to each data point
m	Total numbers of measured value
AMI	Arbitrary Mesh Interface
BAR	Blade area ratio
CFD	Computational fluid dynamics
EIA	Environmental impact assessment
KC	Keulegan-Carpenter number
LDA	Laser Doppler Anemometer
MCT	Marine Current Turbine Ltd
MSE	Mean square error
RANS	Reynolds-averaged Navier–Stokes
SSE	Sum of squares due to errors
TTS	Total sum of squares
TI	Turbulence intensity
TSR	Tip speed ratio
TCT	Tidal current turbine
ZFE	Zone of flow establishment
ZEF	Zone of established flow

CHAPTER 1: INTRODUCTION

1.1 Background of Study

The energy crisis is one of the major problems that humans have to deal with as people rely heavily on electricity (Rocks and Runyon, 1972). The world population has an average growth rate of 0.9% per year. It was estimated it will reach 8.7 billion in 2035. The energy demands will remarkably increase when more people move to urban areas (EIA, 2013). There are many untapped natural resources in the ocean. These resources are potential to be harnessed and make a contribution to future energy supplies. Marine current power is one of the possible resources to generate electricity. It has some advantages over other renewable energy sources as it is easier to be predicted and quantified (Watchorn et al., 2000). Many studies of the tidal or marine current energy have been carried out in the past decade. It is foreseeable that marine current will be a vital natural resource in future energy supplies (Rourke et al., 2010). Many of large-scale tidal/marine current turbines have been tested and deployed around the world (OES-IA Annual Report, 2011, 2012, 2013, 2014).

Malaysia is a tropical country that has a long coastline. The country has high potential to develop marine renewable energy. The support of the research and development in the renewable energies from Malaysian government is rather strong. In the year 2011, Renewable Energy Act and Sustainable Energy Development Authority Act have been enacted. The acts are the catalyst for the industry of renewable energy in Malaysia (Chong and Lam, 2013). Tidal energy extraction in a few locations in Malaysia can generate electricity up to 14.5 GW h annually (Lim and Koh, 2010). Tidal

energy is a promising ocean resource available in Malaysia for future energy supplies (Hashim and Ho, 2011).

The interaction between tidal turbines with ambient environment is interest to many researchers. Installation of a TCT accelerates the vicinity flow leading to the change of surrounding environment (Xia et al., 2010; Shields et al., 2011). Collision risk, acoustic emission, sediment dynamics and morphodynamics of such device have long been identified (Neill et al., 2012). Continuous assessment of environmental impacts of such device is acting a barrier to obtaining permission from relevant authorities. (Hill et al., 2014). Marine Current Turbine Ltd. (MCT) and Verdant Power have had cost a multi-million dollar to monitor environment impacts (Neill et al., 2009). Environmental impact assessments (EIAs) have to be conducted before the application of this technology. The interaction between tidal turbines with ambient environment is unclear at present. Affordable and environmental friendly tidal energy could strengthen the confidence of interested parties to install tidal turbines in potential sites.

1.2 Problem Statement

The presence of tidal stream device could accelerate the flow in its vicinity and lead to local scour around the TCT (Xia et al., 2010; Shields et al., 2011). Scour around marine structures have been well recognized as an engineering issue which causes structural instability (Hoffmans and Verheij, 1997). It is crucial to ensure the structural safety of the TCT during the operation phase to avoid disturbance of energy transmission. Scour related foundation and scour protection is costly, it takes account 30% of the total cost in wind turbine industry (Sumer, 2007). Repair of coastal structure failure due to

scouring is considerably high, where USD 2-10 million is the cost per failure (Lillycrop and Hughes, 1993). The change of the seabed topology may worsen the flow speed and direction. The change of the environment after installation of the TCT should not affect the performance of the turbine.

Scour at bridge piers have been studied extensively in the past (Breusers and Raudkivi, 1991; Melville and Coleman, 2000). Scour around the foundation of offshore wind turbine also attracts researcher attention. Researchers proposed effective scour protection techniques to mitigate the impact of scouring on the stability and dynamic behavior of the offshore wind turbine (De Vos et al. 2011). The scour behavior of TCT has not been well understood (Vybulkova, 2013). Also, it has been reported that the sediment transport in the energy extraction region may have adverse environmental impacts (Shields et al., 2011). Scour leads to the change of sea floor topography which may result in negative consequences for the indigenous marine flora and fauna. If vegetation present at the seabed, the plants are exposed to high shear stress. The survivability of the vegetation is being affected as well as the food-supply of marine fauna. (Vybulkova, 2013). The nature of the interactions between flow generated from the rotor and seabed is not clear at present.

Some knowledge gaps have also been identified, such as the wake and scour prediction. No model is available to predict the wake structure under various turbulence conditions. The flow between turbine rotor and seabed is responsible for the sediment transport and the information of the flow is limited. The time-dependent scour profile

around the support of tidal current turbine is not studied, while no model is available to predict the maximum scour depth around the support of TCT.

1.3 Research Objectives

The study aims to quantify the effect of the flow generated by the rotor on the scour behaviour of the TCT. The generated wake may affect the velocity near seabed. The sediment at seabed could be severely eroded. Comprehensive understanding the wake structure and scour nature of TCT enables engineers to offer a cost-effective design for the foundation and scour protection. Documentation of the flow near the turbine and seabed also gives profound insights on the environmental monitoring. The research objectives are listed as follows:

    a)   To develop an analytical wake model of TCT

    b)   To apply a TCT model for the characterization of the flow between rotor and seabed

    c)   To identify the effects of rotor tip clearance on the scour depth of the TCT

    d)   To examine the temporal variation of the scour profiles of the TCT

    e)   To correlate the rotor tip clearance with the time-dependent maximum scour depth

The results, analytical and numerical models are presented as engineering tools to predict, design and mitigate the wake and its associated effects of TCT in the future.

1.4 Scope of Research

The first objective is to propose an analytical model to predict the initial velocity and its lateral distribution downstream of TCT. The analytical wake model consists of several equations derived from the research works of ship propeller jets assuming a Gaussian distribution for the lateral velocity distribution in a wake. The prediction of wake velocity requires the efflux velocity as an initial input. The recovery of the minimum velocity equation is based on empirical results. The model also aims to predict the wake structure under various ambient turbulence of TI=3%, 5%, 8% and 15% when incoming flow is uniform. The applicability of the proposed model to predict the velocity distribution of turbine wake in the condition of non-uniform incoming flow is not testified in the study.

The study simulates the three-dimensional flow, namely the axial, radial and tangential velocity components below turbine blades with different tip clearances. The tip clearances for simulation are $1.0D_t$, $0.8D_t$, $0.6D_t$ and $0.4D_t$. The turbine rotor is duplicated based on the NACA 63418 hydrofoil profile. Design of turbine rotor is out of the scope of the thesis. The effects of support structure on the flow between rotor and bed are not discussed in the study. The study also investigates the influence of the number of blades on the flow between rotor and seabed. Besides, it also intends to examine the boundary layer development around TCT.

The third, fourth and fifth objectives are to investigate the scour pattern around the support structure of the TCT. The physical model TCT is placed in a hydraulic flume for scouring test. The scour rate of the physical model under the clear water condition has

5

been investigated. The scour rate of scour profile of the TCT is investigated. The effects of rotor tip clearance on the scour profile are identified. The study correlates the scour depth of the TCT with the tip clearance. The relation of the scour depth with tip clearance is only valid for horizontal axis TCT with pile-supported structure.

1.5 Significance of Study

Prediction of the wake is important to understand the flow condition behind a TCT. The proposed model offers a simple, rapid and cost-effective manner to predict the velocity profile of the wake at lateral sections of downstream. The velocity of the wake is a vital factor to decide the spacing among each turbine at a tidal farm. The proposed model also provides an initial input for the scour prediction around the support of TCTs. The numerical model applied to characterize the flow below rotor can be an engineering tool for future flow simulation. The flow conditions help engineers to understand the flow that may affect the sediment transport around the tidal turbine. The scour prediction model enables the monitoring of temporal maximum scour depth. The scour pattern of the TCT can be instructions for the engineers to mitigate severe sediment transport at energy extraction site. All the research outcomes could help with the design of more affordable and environmentally friendly tidal current energy.

1.6 Outline of Thesis

The thesis consists of five chapters. Chapter 1 presents a brief introduction to the concepts of TCT and its importance for human beings to overcome the energy crisis. Chapter 1 also summarizes the objectives and states the overview of this thesis. Chapter 2 documents the backgrounds of tidal current energy and available source in Malaysia. It also covers the state-of-art research of tidal energy in the aspects of the wake and environmental impacts. Chapter 3 presents the methods employed in the study. Chapter 4 documents the findings of the study. Chapter 5 presents the conclusions and contribution, with the recommendation for future work. List of publications have been included after the reference section. Appendix presents the photos of the instruments used in the experimental tests.

CHAPTER 2: LITERATURE REVIEW

2.1 Overview

This section summarizes the relevant research works up to date. Section 2.2 briefly introduces tidal current energy and its advantages over other renewable resources. Section 2.3 identifies the potential sites of tidal stream energy in Malaysia. Sections 2.4, 2.5 and 2.6 document the characteristics of wake and ship propeller jets. These three sections also realize the similarities among these two fluids. Section 2.7 introduces the types of support structures of TCT. It also includes the general seabed response of each support structure. Section 2.8 presents the scour pattern around the support of TCT. Section 2.9 summarizes the equations of scouring prediction for pier/pile and discusses the applicability of existing empirical equations for scour prediction of TCT.

2.2 Background of Tidal Current Energy

Tidal current energy comes from the relative motions of the Earth-Moon system. The tidal movements are cyclic variations in the level of the seas and oceans (Williams, 2000). Tidal current energy is principally harnessing the kinetic energy of moving water to power turbines. It is in a similar manner to wind turbines that use moving air (Hassan et al., 2012). TCTs are usually installed in high-velocity areas where the water flows are concentrated. The potential places for tidal turbine installation are such as entrances to bays and rivers or between land masses (Fraenkel, 2002).

The horizontal axis TCT is a type of hydrofoil-shaped blades applied in tidal current energy devices (Bryden et al., 1998). The horizontal axis tidal turbines rotate about a horizontal axis which is parallel to the current stream (Camporeale and Magi, 2000; Bahaj et al., 2007). The companies actively engaged in TCT development are Aquamarine Power Ltd. (UK), Atlantis Resource Corporation PTE Ltd.(Singapore), Blue Energy Ltd.(Canada), Hammerfest Storm AS(Norway), Lunar Energy Ltd.(UK), Marine Current Turbines Ltd.(UK), Ocean Flow Energy Ltd. (UK), Open-Hydro Ltd.(Ireland), Pulse Generation Ltd.(UK), SMD Hydrovision Ltd. (UK), Tidal Energy Ltd.(UK) and Verdant Power Ltd.(USA). These companies designed various types of tidal current energy device. The tidal turbines in detail which including their dimensions, features and status of development can be found in the work of Rourke et al. (2010) and Bahaj (2011).

Figure 2.1 shows a horizontal axis tidal turbine deployed by Marine Current Turbine Ltd. It is a second generation device consisting of a piled twin rotor two-bladed horizontal axis turbine converter of an installed capacity 1.2 MW. The tidal turbine is the world's first commercial-scale tidal turbine prototype to generate electricity onto the grid (Bahaj, 2011). Atlantis Resource Corp designed a commercial-scale horizontal axis turbine AR1000 for open ocean deployment, as shown in Figure 2.2. The first AR1000 was successfully and commissioned at the Europe Marine Energy Center (EMEC) facility during summer of 2011 (Atlantis Resource, 2015).

Figure 2.1: The tidal turbine SeaGen rated 1.2MW in Strangford Lough (Image courtesy of MCT Ltd)

Figure 2.2: Atlantis Resource Corp, AR1000 1MW before installation (Image courtesy of Atlantis Resource Corp).

2.3 Potential Tidal Stream Energy in Malaysia

Lim and Koh (2011) conducted an analytical study coupled POM to determine the tidal energy density profile of Malaysia (see Figure 2.3). It was concluded that Pontian, Kapar, Tanjung, Alor Star, Karang, Semporna, Kota Blud, Kuching and Sibu were the locations with high potential for tidal energy extraction. The amount of tidal energy that can be extracted at these places is mainly dependent on the features of the designed turbine. Lim and Koh (2011) assumed twin rotor horizontal axis turbines employed. The factors that influence the energy supplied by the turbine are the cut-in speed of turbines, the swept area of turbines and the power efficiency. Lim and Koh (2011) eventually identified that Sibu, Pulau Jambongan and Kota Belud are the locations with great potential for tidal energy extraction with the prior assumptions. The total amount of electricity that can be generated by tidal turbines at those places is about 14.5 G Wh/year.
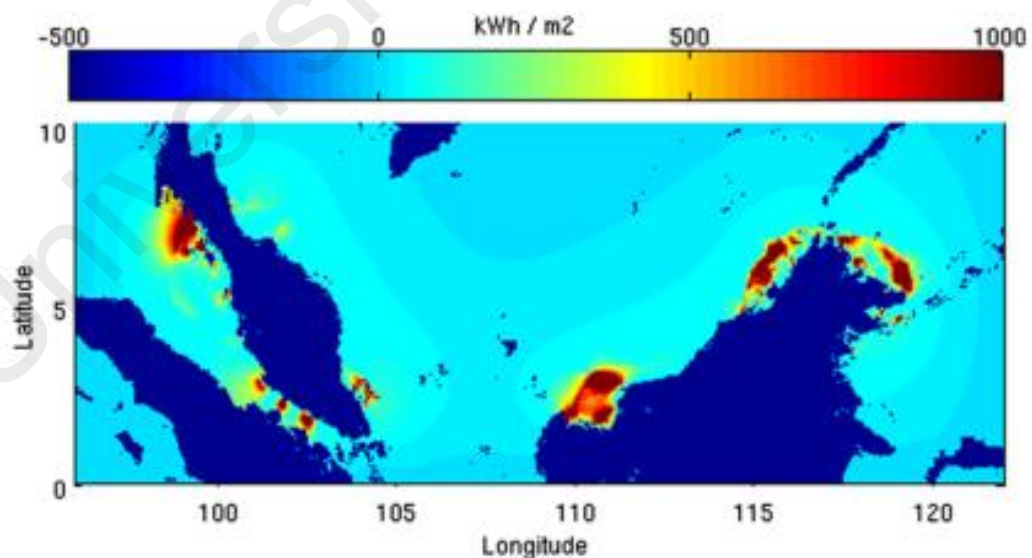
Figure 2.3: Energy density profile of tidal current across Malaysia (Lim and Koh, 2011)

In addition, researchers (Chong and Lam, 2012; Sakmani et al, 2013) claimed the Straits of Malacca is a potential site for the development of tidal energy. It is the longest Straits in the world and it has a constant minimum flow of 0.5m/s with maximum up to 4m/s in particular regions (Chong and Lam, 2012). Sakmani et al. (2013) used the data from acoustic Doppler current profiler (ADCP) and with the considerations of environmental issue and cost-effectiveness. They proposed Pulau Pangkor as the potential site for tidal stream energy development. The efforts from Lim and Koh (2011), Chong and Lam (2012) and Sakmani et al. (2013) offer insight for Malaysia to realize the potential of tidal energy for future energy supplies.

2.4 Wake of TCT

2.4.1 Wake Characteristics and Its Recovery

Mayers and Bahaj (2010) stated that the fluids passing through the rotor plane region experience velocity reduction and form an expanding wake. The velocity deficit influences the performance of the turbines in tandem and thus affects the overall efficiency of tidal-current turbines in arrays. Myers and Bahaj (2012) reported that proper spacing of TCTs in the upstream may enhance the available kinetic energy of the downstream up to 22%. It is therefore of significant importance to study the wake characteristics as it will ultimately affect the output of tidal array farms.

The first attempt to study wake is Myers and Bahaj (2007) performed wake studies of a 0.4 m diameter horizontal axis marine current turbine in a circulating channel. The measurements indicated that the variations of water surface elevation and flow velocity could occur. Sun et al. (2008) applied the absorption disc representing the TCT to

investigate the near wake of the tidal turbine. It was focused on the effects of wake on the free-surface and flow velocity close to the disc. Sun et al. (2008) claimed that fluid reaches the disc it accelerates as it passes through. The speed then reduced directly behind the disc. Their findings also showed that a drop in the free-surface behind the disc occurred. The study of Myers and Bahaj (2010) performed experimental analysis of the flow field around the TCT by using disk rotor simulators. It declared that closer seabed proximity causes different mass flow below the rotors. It could result in the wake further persist downstream and slow down the wake recovery process. The lesser flow below turbine blades the more delayed of wake recovery. The flow pattern underside of the wake and within the wake could be affected by the vertical location of the disks (see Figure 2.4).
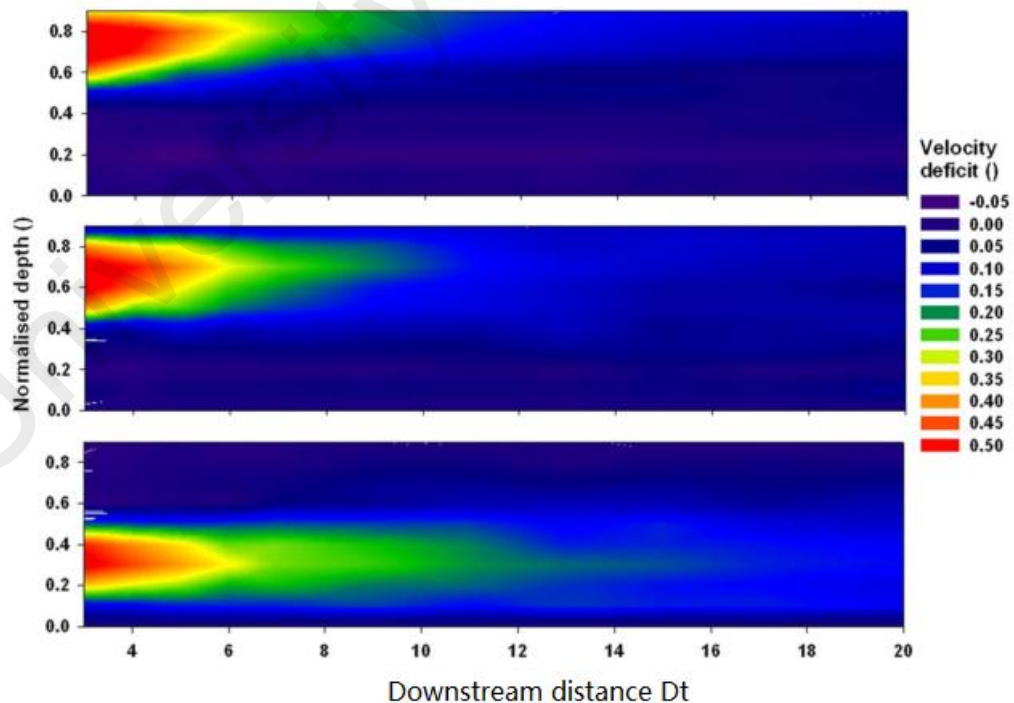
Figure 2.4: Centre plane velocity deficit for varying disk submersion depth. The disk center at $0.75H$ (top), $0.06H$ (centre) and $0.33H$ (bottom).

Pinon et al. (2012) conducted wake study of three-bladed TCT in uniform free upstream current. The axial velocity profiles at different locations behind the turbine have been illustrated in Figure 2.5, where r is the radial distance, R_t is the radius of the turbine, D_t is the diameter of the turbine, V_a is the axial velocity, V_∞ is the free stream velocity. The wake has approximately 50% velocity deficit in near wake region (x/D_t=1.2). The maximum velocity deficit occurs at near centre of the rotation axis. The velocity deficit decreases at a slow rate along the downstream. It is in line with observation reported by Myers et al. (2008) and Myers and Bahaj (2010). The wake (Figure 2.5) is not fully covered even at $8.0D_t$ downstream. It has approximately 35% velocity deficit. The recovery of wake velocity to free stream velocity can be further downstream. Results from Batten et al. (2013) showed that up to $22D_t$ downstream the wake velocity has not been fully recovered to the upstream velocity.
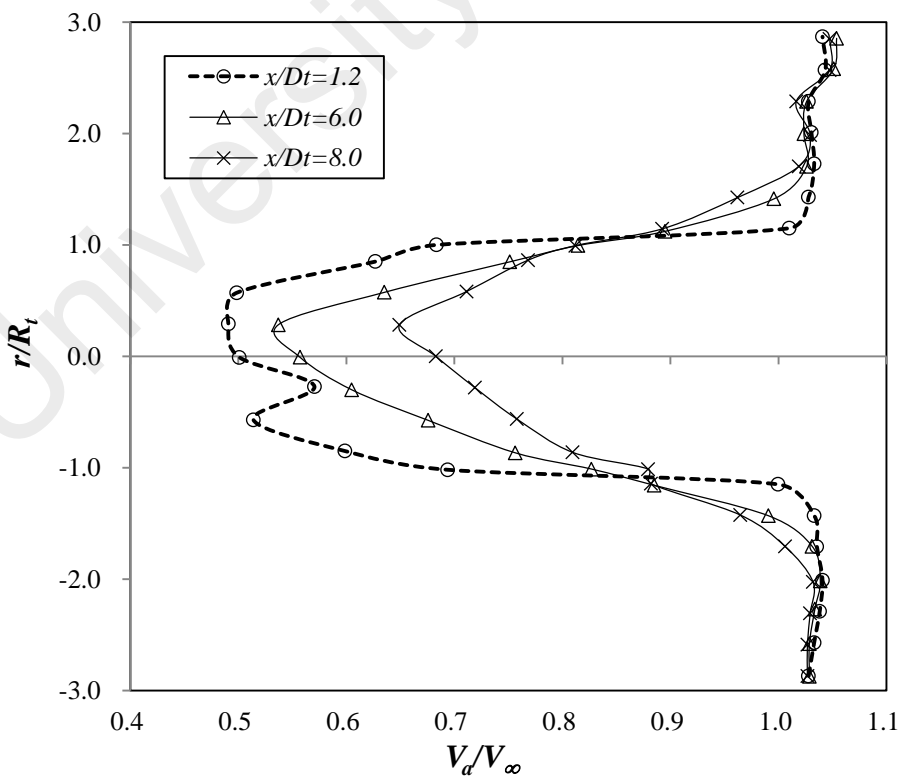
Figure 2.5: Wake characteristics of horizontal axis tidal-current turbine.

According to Pantan (Lam et al., 2012c), turbulence intensity can be defined for each velocity component as the root mean square (RMS) referenced to a mean flow velocity (V_{ref}), as Equation (2.1).

$$I_x = \frac{\sqrt{u'}}{V_{ref}}, \ I_y = \frac{\sqrt{v'}}{V_{ref}}, \ I_z = \frac{\sqrt{w'}}{V_{ref}} \tag{2.1}$$

where I_x, I_y, I_z are the x-component, y-component and z-component of turbulence intensity, respectively. The overall turbulence intensity is defined by Equation (2.2).

$$I = \frac{\sqrt{\frac{1}{3}(u' + v' + w')}}{V_{ref}} \tag{2.2}$$

where I is the overall turbulence intensity, u', v', w' are the x-,y-,z-components of turbulence and V_{ref} is the reference mean velocity.

Ambient turbulence intensity has a crucial role on the wake shape behind the TCT. The studies of Maganga et al. (2010), Myers and Bahaj (2010), and Mycek et al. (2014) highlighted that the ambient turbulence intensity influences the wake structure. The detail experimental work from Mycek et al. (2014) pointed out the significant role of ambient turbulence on the behaviour of a three-blade turbine. Their results showed that the wake shape, length, and strength largely depended on the upstream turbulence conditions. The wake remained pronounced ten diameters downstream of the turbine with almost 20% velocity deficit when I=3%. On the other hand, the wake recovers much faster with a higher turbulence intensity I=15%. The upstream conditions including velocity, turbulence and shear stress are almost fully recovered six diameters

downstream. However, high turbulence condition may cause more force fluctuations and thus decrease the lifespan of the blade.

2.4.2 Wake Modelling

Extensive efforts of analytical, numerical and experimental studies have been done in the past to understand the nature of wake. Perforated disks can provide appropriate physical knowledge to understand turbines behavior. It also has been widely applied in turbine simulations in wind turbine experiments (Builtjes 1978; Sforza et al., 1981; Vermeulen and Builtjes, 1982). Sun et al. (2008) firstly applied the absorption disc representing the turbine to study the near wake. Sun et al. (2008) believed that thrust force on the turbine is of principal importance in the wake development. A series of thrust forces on a real turbine can be simulated by perforated disk with a range of porosities.

Myers and Bahaj (2010) also highlighted that investigations of such technology at medium or large scale at basic research level is infeasible. The work of wake investigation needs to focus on small scale testing, which is able to conduct at laboratory. Myers and Bahaj (2010) also doubted the modelling of horizontal axis rotors at very small scale. They believed that the channel flow properties cannot scale down precisely while maintaining rotor thrust, power, and tip speed without remarkably changing aspects of the downstream flow field. Accurate tip speed scaling of a 100 mm diameter rotor would require the rotor to have a rotational speed up to 1500 rpm if the rotor needs to maintain a typical full-scale tip speed of 10 m/s. It is the main reason that

16

Myers and Bahaj (2010) employed a mesh disk to identify the governing parameters affecting the wake.

Harrison et al. (2010) conducted CFD simulations using an actuator disc and compared to the experimental results of Myers and Bahaj (2010). It discovered that the trend of wake recovery and turbulence levels is qualitatively similar in the CFD and experimental results. There are significant computational benefits in approximating the turbine as a disc rather than modelling its geometry in full in a RANS simulation. A full model of the rotor requires mesh resolution at the blade surface to be sufficient to capture the boundary layer and separation. This requires a very large number of mesh elements and computational efforts. Furthermore, modelling a rotating turbine requires that the model be unsteady and the blades change position with every time step.

The actual representation of the flow generated by rotor turbine is still achievable, many numerical and experimental efforts to study the tidal turbine wakes by using real turbine rotor have been also carried out (Maganga et al., 2010; Mycek et al. 2011, 2014; Pinon et al., 2012; Stallard et al., 2011, 2013; Batten et al., 2013;Tedds et al., 2014). The size of the turbines incorporated in all these studies ranges from 0.27 to 0.8 m. Pinon et al. (2012) developed a particle method to model unsteady three-dimensional wake flows of tidal turbine other than actuator disc. The velocity of the wake of the turbine has good agreement with experiments up to ten diameters downstream of the turbine. The one from Tedds et al. (2014) challenged those researches used disks modelled turbine and claimed that their approaches may not predict the turbulent kinetic energy decay rate of HATT wakes precisely.

Although numerical and experimental techniques have become sophisticated and accurate in recent years, a simple analytical model is still useful to predict the wake profile of tidal current turbines as its simplicity and cost-effective. Many analytical investigations have been conducted on wind turbine wakes. One of the pioneering analytical wake models is proposed by Jensen (1983).The most recent one is from Bastankhah and Porté-Agel (2014) proposed a new analytical model for wind turbine wakes by applying conservation of mass and momentum. They assumed a Gaussian distribution of the velocity deficit in the wake. The tidal turbine and wind turbine operate in the different ambient environment. The flow direction and turbulence in river and marine currents are far more consistent and predictable compared to wind in the atmospheric boundary layer. The analytical tools may be more suitable to be applied in tidal turbine wake.

The pioneering model in predicting lateral velocity behind tidal turbine is proposed previously by Lam and Chen (2014). They also assumed a Gaussian distribution for the wake velocity and validated the proposed equation by comparing to experimental data of Maganga et al. (2010). The predicted mean stream wise velocity agrees well with the experimental data when the I=8%. Better understanding of the wake characterization is also critical to quantify the potential effects on the sediments transport capacity. The sediment transport in the energy extraction region has negative environmental impacts (Shields et al., 2011). The analytical model for tidal turbine wake prediction could help the engineers rapidly to calculate the wake velocity and identify the transport capacity of the water column along the downstream of turbine wake.

2.5 Flow Condition between Rotor and Seabed

As presented in Section 2.4, a velocity deficit occurs behind a turbine and gradually the velocity increases along the downstream of the wake. The formation of wake will affect the flow close to the seabed. However, to date, little work has been done to present the flow behaviour under a rotor. Myers and Bahaj (2007) reported wake studies of a 1/30th scale horizontal axis tidal turbine and found that the blockage-type effects took place. The measured velocity is greater than the incoming flow around the sides of the rotor. Sun (2008) simulated turbine by using actuator mesh disk and claimed that localised flow acceleration occurs during the energy extraction of the turbine. Chamorro et al. (2013) performed velocity measurements in the near wake of a 3-bladed turbine. It was found that tangential component was to be remarkably insignificant at the turbine tip radius and higher radial velocity was observed near the turbine tip.

No information was found on the flow pattern further closer to the seabed. The flow between rotor and seabed are responsible for the sediment transport. The flow is also of importance when determining TST effects on ecosystem health and morphodynamics. The nature mechanism of the turbine may also impose tangential and radial velocity components in the water flow. All these factors may have environmental impacts on the region of energy extraction. The flow below the rotor is responsible for the scour and sediment transport as some sediment may lift up. Better understanding of the flow pattern below rotor could offer critical insights into the influence of rotor on the scour mechanism and sediment transport in the near flow field of the TCT.

2.6 Ship Propeller Jets and its Induced Scour

2.6.1 Nature of Ship Propeller Jets

The well-established knowledge of ship propeller jets could be a benchmark for investigation of the wake development and scour nature of the TCT. This section aims to review the fundamental knowledge of ship propeller jets and to figure out the similarities between ship propeller jets and turbine wake. Ship propeller has a reverse mechanism as TCT. A TCT harnesses kinetic energy from the current flow (He et al., 2011). A ship propeller converts the torque of a shaft to produce axial thrust for propulsion (Lam et al., 2010; He et al., 2011). Tidal-current turbine produces the wake and the ship propeller produces the jets during operations, respectively. Lam et al. (2010) conducted Laser Doppler Anemometry (LDA) measurements and stated that the axial component of velocity is the primary contributor to the velocity magnitude at the initial plane of a ship's propeller jet. The tangential and radial components are the second and third-largest contributors to the velocity magnitude.

Lam et al. (2011) reviewed the equations used to predict the velocity distribution within a ship's propeller jet. The study found that the rotational and radial components of velocity are still poorly understood compared to the axial component of velocity. The accuracy of the entire jet relies on the initial prediction of efflux velocity (Stewart, 1992; Lam et al. 2011). Efflux velocity is defined as the maximum velocity taken from a time-averaged velocity distribution along the initial propeller plane (Ryan, 2002). Equations for predicting efflux velocity have been proposed Hamill (1987), Stewart (1992) and Hashimi (1993), as shown in Table 2.1. These studies have found that the

efflux velocity of propeller jets was associated with thrust coefficient (C_t), speed of rotation of propeller in revolutions per second (n) and propeller diameter (D_p). Stewart (1996) reported that the coefficient used in the equation to predict efflux velocity was not a constant. This coefficient depends on the propeller characteristics.

Table 2.1: Equations for efflux velocity

Proposed Equation	Notation
Hamill (1987)	
$$V_o = 1.33 n D_p \sqrt{C_t}$$	V_o is efflux velocity, n is speed of rotation of propeller in revolutions per second, D_p is propeller diameter and C_t is thrust coefficient.
Stewart (1992)	
$$V_o = \xi n D_p \sqrt{C_t}$$ $$\xi = D_p^{-0.0686} \left(P/D_p \right)^{1.519} BAR^{-0.323}$$	ξ is Stewart's efflux coefficient, P/D_p is the pitch ratio of the propeller, BAR is the blade area ratio (ratio of projected area of all blades to the total area of the propeller disc).
Hashimi (1993)	
$$V_o = E_o n D_p \sqrt{C_t}$$ $$E_o = \left(D_p/D_h \right)^{-0.403} C_t^{-1.79} BAR^{0.744}$$	E_o is Hashimi's efflux coefficient, D_h is the diameter of propeller hub.

Many researchers claimed that that the velocity magnitude of a ship's propeller jet tends to decay along the longitudinal axis from the initial plane immediately downstream of the propeller jet (efflux plane)， (Blaauw and van de Kaa, 1978; Hamill, 1987; Stewart, 1992; McGarvey, 1996). The fluid in this region has high viscous shear and it causes the fluid mix with surrounding water. The fluid within the propeller jet gradually decelerates with longitudinal distance from the propeller face. The still ambient fluid slowly accelerates at the same time (Brewster, 1997). A ship propeller jet consists of two zones, namely the zone of flow establishment (ZFE) and the zone of

established flow (ZEF). Figure 2.6 depicts the schematic diagram of these two regions. The jet forms the zone of flow establishment initially while the propeller is rotating. Because the hub is at the center of the propeller, the propeller jet forms a low velocity core along the axis of rotation within the zone of flow establishment. The velocity profiles of propeller jets within the zone of flow establishment have two peak ridges. The influence of the hub disappears gradually along longitudinal axis due to the mixing of fluid in high velocity and fluid in low velocity central core (Hamill, 1987). The fluid is mixing with the surrounding water both inwardly and outwardly along the axis of rotation at the beginning (McGarvey, 1996; Lam et al., 2011). The flow will only be mixed outwardly at a certain distance downstream. It is the region called the zone of established flow. There is only one maximum velocity peak located at the axis of rotation in this region (McGarvey, 1996; Lam et al. 2011).
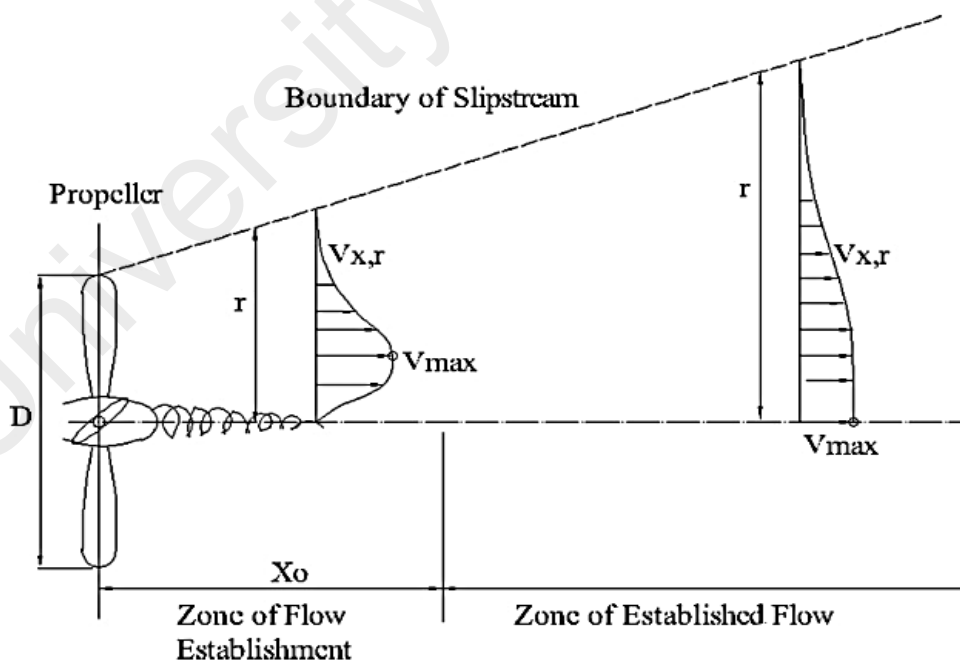
Figure 2.6: Schematic view of propeller jet (Hamill, 1987)

Lam et al. (2012a) presented fluids flow in the zone of flow establishment from a ship propeller. The measurements at two locations in the zone of flow establishment have been selected and demonstrated in Figure 2.7, where R_p is radius of propeller, D_p is diameter of propeller, V_o is efflux velocity for ship propeller jets and free stream velocity for turbine wake. The axial velocity at x/D_p=0.79 and x/D_p=1.05 have little differences. It shows two-peaked ridges velocity profile with a low velocity core at the centre. The axial velocity distribution of turbine wake ($1.2D_t$) presented in Figure 2.7 shows reverse velocity distribution as ship propeller jets. It has two dips of velocity deficit and a high core velocity near the centre. The axial velocity of turbine wake further downstream shows one dip only. The propeller and the turbine both have three blades. The diameter of the propeller (76 mm) is much smaller that of turbine (700 mm). The experiment conducted by Lam et al. (2012) is in "bollard pull" condition (zero advance speed). The velocity outside the jets is zero which is different with the flow field outside the turbine wake. The velocity distribution of turbine wake (x/D_t=1.2) has been inverted in order to compare with that of ship propeller jets. The inverted axial velocity profile of turbine wake has a similar pattern as the velocity distribution of ship propeller jets (see Figure 2.7). It is foreseeable the velocity profile of ship propeller jets and inverted wake will be more identical if the propeller and turbine have similar geometrical characteristics.

23
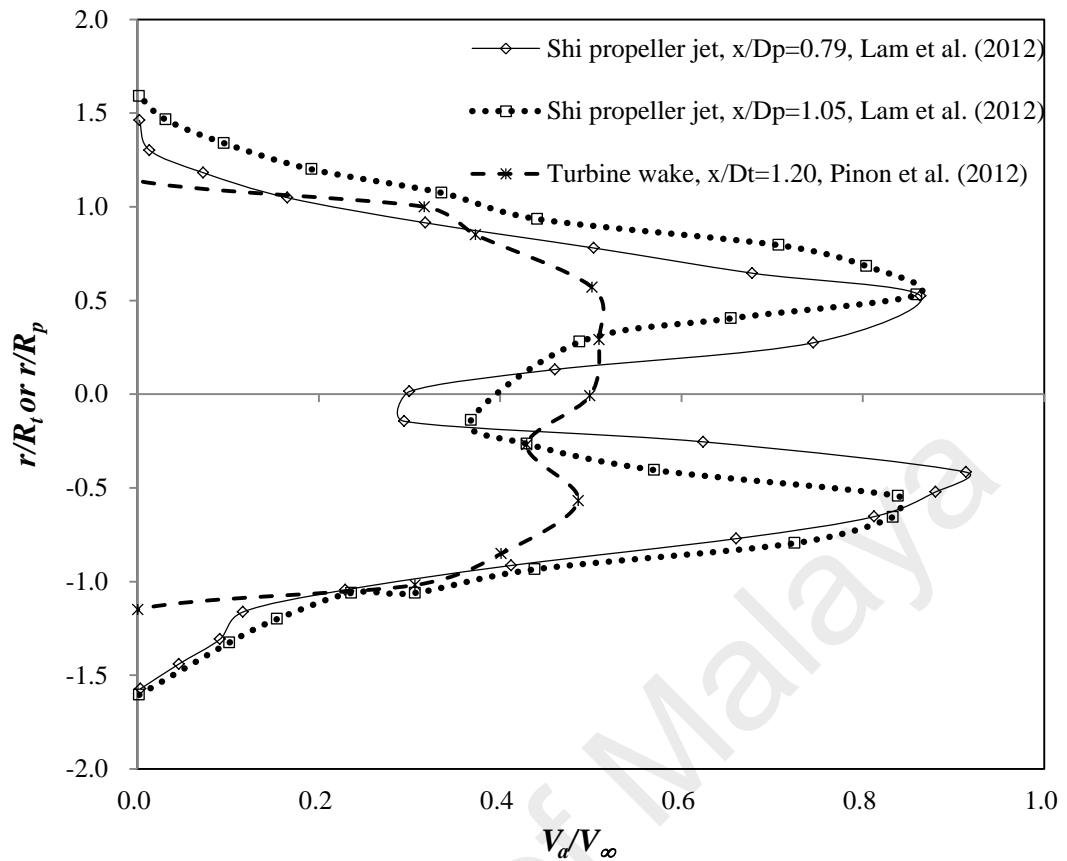
Figure 2.7: Comparison of velocity profile between a ship propeller jet and turbine wake

2.6.2 Ship's Propeller Jets Induced Scour

The velocity investigation of ship's propeller jets has been discussed in the preceding section. Sumer and Fredsøe (2002), Whitehouse (1998) and Gaythwaite (2004) claimed that the velocity prediction within a ship's propeller jet is the initial step to investigate the seabed scouring. Blaauw and van de Kaa (1978), Verhey (1983), and Aberle and Soehngen (2008) focused on the prediction of the maximum scour depth in the absence of berthing structure. Hamill (1987) carried out an extensive study to investigate seabed scour due to the propeller jet by using both the fine and coarse sands. The temporal development of maximum depth of scour was examined and it can be written in a dimensional consideration, as shown in Table 2.2. Hamill (1987) suggested that the

scour depth relates to the densimetric Froude number, size of sediment and the clearance between the propeller and seabed. The maximum velocity and its distribution of a jet mainly depend on the characteristics of a turbine. Hamill et al. (1999) extended their earlier studies by including the effect of propeller jets on quay walls. They showed that the densimetric Froude number (F_o) plays the most important role in affecting scour depth through dimensional analysis. Hong et al. (2013) studied the development of a scour hole with non-cohesive sediments due to the jet induced by a rotating propeller, which focused on the influences of various parameters on the time-dependent maximum scour depth.

Table 2.2: Scour Depth Predictions

Proposed Equation	Notation
Hamill (1987)	
$$\frac{\varepsilon_m}{D_p} = f\left[F_o, \frac{D_p}{d_{50}}, \frac{C}{d_{50}}\right]$$ $$F_o = \frac{V_o}{\sqrt{g d_{50} \frac{\Delta\rho}{\rho}}}$$	ε_m is maximum depth of scour, F_o is densimetric Froude number, d_{50} is median sediment grain size, C is clearance between the propeller tip and the seabed, g is acceleration due to gravity, $\Delta\rho$ is difference between the mass density of the sediment and the fluid, and ρ is density of fluid.
Hong et al. (2013)	
$$\frac{S_t}{D_p} = k_1 \left[\log_{10}\left(\frac{V_0 t}{D_p}\right) - k_2\right]^{k_3}$$ Where $$k_1 = 0.014 F_0^{1.120}\left(\frac{C}{D_p}\right)^{-1.740}\left(\frac{C}{d_{50}}\right)^{-0.170}$$ $$k_2 = 1.882 F_0^{-0.009}\left(\frac{C}{D_p}\right)^{2.302}\left(\frac{C}{d_{50}}\right)^{-0.441}$$ $$k_3 = 2.477 F_0^{-0.073}\left(\frac{C}{D_p}\right)^{0.53}\left(\frac{C}{d_{50}}\right)^{-0.045}$$	S_t is the scour depth at time t, D_p is the diameter of propeller. The equation is valid only for $0.5 < \frac{C}{D_p} < 2.87$ and $5.55 < F_0 < 11.1$.

2.7 Seabed Scour for Different Type of Support Structures

2.7.1 Support Structures of TCT

The technological development of the horizontal type does seem more mature compared with the vertical type due to its high promised performance. The established commercial turbines of Seaflow (2003) and SeaGen (2008) are both horizontal axis marine current turbines. The development of tidal energy technologies includes the design of a robust support structure to hold the turbines safely. The support structure for horizontal axis turbine can be categorised into four main types as shown in Figure 2.8 (Rourke et al., 2010).

Gravity Structure Monopile Structure Piled Jacket Structure Floating Structure
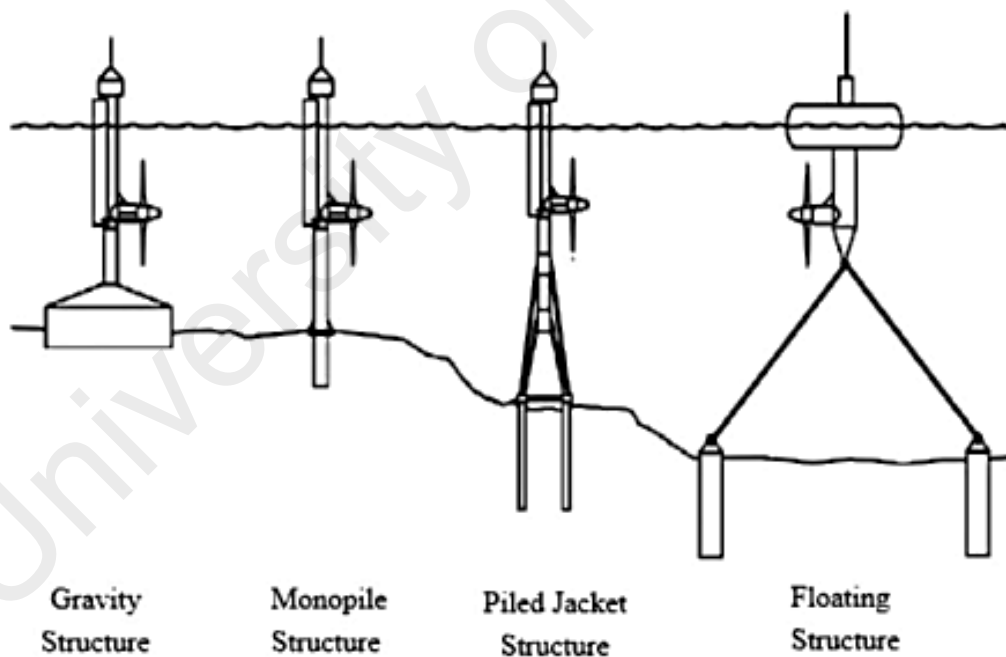
Figure 2.8: Different types of support structures with horizontal marine current turbines

(1) Gravity structure: The gravity structure is a concrete or steel structure to hold the turbine by its self-weight to resist overturning.

(2) Monopile structure: The monopile structure is a large steel beam with a hollow section penetrating to a depth of seabed between 20 and 30 m for a soft seabed. The processes of predrilling, positioning and grouting are required for the seabed condition of hard rock.

(3) Tripod/Piled Jacket structure: The tripod Jacket structure anchors each corner of the basement to the seabed by using steel piles. These steel piles are driven in between 10 and 20 m into the seabed to hold the structure firmly. Tripod Jacket structure is a well-established technology in the application of oil and gas industry.

(4) Floating structure: Floating structure is suitable for the application of deep water. The floating device appears at the surface of the water to hold the submerged turbine structure in the water. The submerged structure is locked to the mounting device at the seabed by using chains, wire or synthetic rope.

2.7.2. Scour Behaviour of Different Types of Support Structures

Rambabu et al. (2003) stated the fluid flow, geometry of foundation and seabed conditions are the governing factors for the seabed scouring. The characteristics of fluid flow include the current velocity, Reynolds number of model and Froude number of the flow. The abovementioned four types of foundations have different areas of contact with the seabed. The selection of support structures leads to different flow patterns occurring at the foundation of with different formation of flow-induced vortices in the vicinity of support structures. Different foundation geometries cause different scouring patterns.

The gravity structure is most susceptible to seabed scouring due to its large contact area with the seabed compared to the other three types of foundation. The determination of geometry size and seabed preparation is required to implement the gravity structure as the foundation of horizontal axis TCT. The monopile is less susceptible to scour compared to gravity structure due to its small contact area with the seabed (Rourke et al., 2010). McDougal and Sulisz (1989) stated the floating structure gives lowest impact on the seabed scour due to the low area of contact between the structure base and seabed. However, it may have less advantage on the positioning of the turbine in harsh marine environment.The scour of piled jacket structure is more complicated than the other structures due to its footing shape (Rudolph et al., 2009).

The seabed preparation is time-consuming and the construction process of the foundation is costly. The potential sites for marine current energy have fast flowing fluid, which may be dangerous for divers. Gravity structure may be suitable for the sites without excessive seabed preparation. Monopile structure can be used to replace the gravity structure as no seabed preparation is required prior to the installation (Rourke et al., 2010). The piled Jacket and floating structures are both alternatives without seabed preparation. The floating structure needs stable points at the seafloor, fixing the structure to the seabed through chains.

The scour development around monopile structures has been studied extensively for the foundation of offshore wind turbine in the past few decades (Sumer, 2007; Rudolph et al., 2009). The application of monopile structures in TCT is suggested for both the cost and structural stability (Fraenkel, 2002). The first tidal turbine in the world (300kW

Seaflow) is supported by a monopile, which generated electricity successfully (Fraenkel, 2007). The monopile structure is analogous to the bridge piers and piles which have been studied for more than a hundred years. The knowledge pool of the bridge piers and piles study is the references to the monopile structures of TCT.

2.8 Scour Nature of TCT

Neill et al. (2009) developed large grid cell (km-scale) simulations to explore the impacts of array turbine farm on sediment dynamics. It claimed that small amount of energy extracted from a site might affect the erosion and deposition pattern over a long distance from the point of energy extraction. The effects may up to 50 km in the case of the Bristol Channel. Vybulkova (2013) modified vorticity transport model to simulate wake and its interactions with local sediment. The results show that the flows downstream of the rotor affect the marine environment over scales of a few centimetres. Hill et al. (2014) conducted a study on the scour of an axil-flow hydrokinetic turbine under clear water and live-bed conditions. Results indicate that the rotor of turbine increases the local shear stress of sediment around the turbine. The velocity deficit in the wake region leads to the flow acceleration below the rotor. The local scour of the turbine is accelerated and expanded when compared to bridge scour. Results indicate that regions susceptible to scour typically persist up to 2 times turbine diameters downstream and up to 1.5 times turbine diameter to either side of the turbine centre location. Within the regions, results showed scour depths approaching 12-15% of turbine diameter from small scale experiment and 30-35% of turbine diameter from the large-scale experiments. Future work is required to investigate the temporal evolution of

29

tidal turbine scour process. It is also recommended to identify the effects of tip clearance on the scour rate of TCT.

2.9 Scour Prediction of TCT

2.9.1 Empirical Equations for Scour Prediction of Pile/Pier

Numerous equations and relations have been proposed to estimate the scour depth of a pier or pile in the previous studies, as shown in Table 2.3. Neill (1973) proposed a simple equation in 1973 to relate the depth of scour to the diameter of penetrated structure to be a constant (K_s). K_s is the correction factor for pier shape, which is a constant depending on the shape of the penetrated structure. Neill (1973) proposed the correction factor K_s=1.5 for round-nose pier or circular pier and K_s =2.0 for rectangular pier. The study of Neill has been the foundation for the works of Richardson et al. (1975) at Colorado State University (CSU), Breusers et al. (1977) , Breusers and Raudkivi (1991), Ansari and Qadar (1994) and Richardson and Davis (2001). These researchers included more parameters to consider the incoming flow, water depth, bed condition and size of sediment to enhance the Neill's equation.

Table 2.3: Summary of equations for predicting scour around piles/piers

Existing Equations	Notation
Neill 1973	
$$\frac{S}{D} = K_s$$	S is the vertical distance between the maximum depth in scour hole in equilibrium situation and the surrounding undisturbed bed, D is pile diameter, and K_s is the correction factor of pier shape.
Richardson et al. 1975 CSU	
$$\frac{S}{D} = 2.0K_s K_\theta \left(\frac{h}{D}\right)^{0.35} F_r{}^{0.43}$$ $$K_\theta = (\cos\theta + \frac{L}{a}\sin\theta)^{0.65}$$ $$F_r = \frac{U_c}{(gh)^{0.5}}$$	K_θ is the correction factor for flow angle of attack, h is water depth, F_r is the Froude number of incoming flow, θ is angle of flow attack, L is pier length, a is pier width/diameter, U_c is depth-averaged current velocity and g is gravitational acceleration.
Breusers et al. 1977	
$$\frac{S}{D} = 1.5K_s K_\theta K_b K_d \tanh\left(\frac{h}{D}\right)$$ $$K_b = 0, \quad if\ \frac{U_c}{U_{cr}} < 0.5$$ $$K_b = 2\left(\frac{U_c}{U_{cr}}\right) - 1, \quad if\ 0.5 \ll \frac{U_c}{U_{cr}} < 1$$ $$K_b = 1, \quad if\ \frac{U_c}{U_{cr}} \gg 1$$	K_b is the correction factor for bed condition, K_d is the correction factor for size of bed material (U_c is the depth-averaged current speed and U_{cr} is the threshold depth-averaged current speed.
Breusers and Raudkivi 1991	
$$\frac{S}{D} = 2.3K_y K_s K_d K_\sigma K_\beta$$	K_y is the correction factor of flow depth, K_d is the correction factor of pier and sediment size, K_σ is the correction factor of sediment grading and K_β is the correction factor of pier alignment.
Sumer et al.1992	
$$\frac{S}{D} = 1.3\{1 - \exp(-m(KC - 6))\}$$ $$KC = \frac{U_m T_w}{D}$$	m is an empirical factor determined from experiments as a constant of 0.03, KC is Keulegan-Carpenter number (drag force / inertia force of flow), U_m is amplitude of the wave velocity variations near the bed in absence of pile (statistic parameter), T stands for wave period of incoming flow in second.
Ansari and Qadar 1994	
$$\frac{S}{D} = 0.86D^2\ , where\ D < 2.2m$$ $$\frac{S}{D} = 3.06D^{-0.6}\ , where\ D > 2.2m$$	D is projected width of pier.

, Summary of equations for predicting scour around piles/piers

Melville 1997	
$$\frac{S}{D} = K_y K_s K_d K_I K_\beta K_G$$	K_I is the correction factor of flow intensity, K_G is the correction factor of channel geometry
Richardson and Davis 2001	
$$\frac{S}{D} = 2.0 K_s K_\theta K_b K_d K_w (\frac{h}{D})^{0.35} F_r^{0.43}$$	K_w is the enhance correction factor for pier width/pile diameter.
Sumer and Fredsøe 2002	
$$\frac{S}{D} = 1.3\{1 - exp(-A(KC - B))\}$$ $$for \ KC \geq B$$ $$A = 0.03 + \frac{3}{4}U_{cw}^{2.6}$$ $$B = 6exp(-4.7U_{cw})$$ $$U_{cw} = \frac{U_{uc}}{U_{uc} + U_m}$$	U_{uc} is the undisturbed current velocity, and U_m is the maximum value of the undisturbed orbital velocity at the sea bottom (statistic parameter).
Raaijmakers and Rudolph 2008	
$$\frac{S}{D} = 1.5 K_v K_h \ tanh(\frac{h}{D})$$ $$K_h = (\frac{h_p}{h})^{0.67}$$ $$K_v = 1 - exp(-A)$$ $$A = 0.012KC + 0.57KC^{1.77}U_c^{3.67}$$	K_v is correction factor accounting for wave action, K_h is correction factor accounting for piles that do not extend over the entire water column, h_p is pile height and not over h.

Richardson et al. (1975) at Colorado State University (CSU) improved Neill's equation by considering the water depth and incoming flow. The angle attack of the incoming flow and the water depth are both being considered in Richardson's equation. Richardson's equation proposed that the ratio of the depth of scour to the diameter of the pier is two times of the multiplication of four dimensionless terms. These dimensionless terms are term of pier geometry, term of angle attack, term of water depth over diameter ratio and term of Froude number of flow.

Breusers et al. (1977) improved the empirical equation for predicting the scour depth based on experimental observations with consideration of tidal flow in 1977. The bed conditions, size of bed sediment and water depth were included in Breusers's equation. The inclusion of the bed condifreplacetions and size of sediment is important to relate the source of scour (incoming flow) to the area being scoured (seabed). Breusers and Raudkivi (1991) included the consideration of the water depth (K_y) as Richardson's equation (1975) and the group of pier alignment (K_β). The correction factor of bed conditions proposed by Breusers et al. (1977) was replaced by an analogous correction factor, namely sediment grading (K_σ). The correction factor of grading considers the seabed with various layers, which is vulnerable to be scoured, rather than only the top layer of bed. The consideration of sediment grading is essential at the seabed with non-uniform sediments. Melville (1997) proposed another analogous scour estimator with extra factors such as flow intensity (K_I) and channel geometry (K_G).

Sumer et al. (1992) carried out the experimental investigation into scour around piles exposed to waves. His research suggested that the effects of particlelee wake and horseshoe vortex are the two crucial components related to scour process. The horseshoe vortex contributes to the scour in front of the structure, whereas the lee wake forms the vortex shedding contributing the scour at the back of the structure. The conditions of horseshoe vortex and lee wake depend on the Keulegan-Carpenter (KC) number (Sumer et al., 1992). Sumer et al. (1992) also proposed KC number can be used to relate to the equilibrium scour depth on live beds. KC number is a ratio of the amplitude of wave velocity variations and the wave period of the incoming flow to the diameter of a pile, as shown in Table 2.3.

Ansari and Qadar (1994) estimated the ultimate depth of local scour at bridge piers based on his empirical study of field measurements. The equation is developed based on the curves of the envelope from the field data with the consideration of a wide range of parameters. The scour depth is related to solely one parameter, which is the diameter of pier. The development of the equation may be transferable to produce the scour equation to tidal current energy. However, the sufficient scour data of TCT may be required for the development by using the approach of Ansari and Qadar (1994).

Richardson and Davis (2001) proposed an enhanced equation to determine the ultimate scour depth for both live-bed and clear-water scours in 2001. The equation considers the large particle as the sediment at the seabed and the wide pier in the scour process. The large particle may reduce the scour depth at seabed compared with the small particle as sediment. For the consideration of wide piers, Richardson and Davis (2001) conducted the flume studies to investigate the scour depth by using wide piers in shallow water. The results from experimental study are compared to the field measurement of the scour depth at bascule piers (a type of wide pier). The enhanced correction factor of pier width (K_w) is proposed in addition to the correction factor of pier shape (K_s) in 1975 to consider the impact of wide piers to the scour depth. The K_w can be applied when the following conditions are matched: (1) the ratio of flow depth (H) to pier width/pile diameter (D) is less than 0.8; (2) the ratio of pier width to median diameter of bed material (d_{50}) is greater than 50; (3) the Froude number of flow is subcritical.

Sumer and Fredsøe (2001) carried out the investigation to include the influences of current to the ocean wave induced-scour proposed in 1992. The equation is derived from the experiments in the range of KC in between 5 to 30 for the live-bed condition. The tidal current changes with time in a day and therefore the orbital velocity (velocity of particles due to wave motion) is used for the equation derivation. The time-averaged

34

velocity has been used to consider the current speed in the equation. Sumer and Fredsøe (2001) also suggested that the depth of time-averaged current-induced scour is 1.3 times the diameter of the pile (S/D=1.3) with a standard deviation of 0.7. Other than that, den Boon et al. (2004) proposed that the maximum depth of scour around a monopile with sole consideration of current is 1.75D when no protective unit is used at the seabed.

The prediction of scour depth for full water depth piles is well developed. All the aforementioned predictors apply to full water depth piles. However, if the pile height-to-diameter ratio is smaller than a critical value, the size of the horseshoe vortex in front of the pile will decrease with a decrease in pile height (Sumer, 2002). Therefore, the scour depth in front the cylinder will reduce with decrease in pile height. The decrease of pile height also weakens the vortex shedding behind the cylinder, which results in the reduction of scour depth behind the structure. More and more attention has been drawn to quantify the effect of pile height to scour depth. Raaijmakers and Rudolph (2008) proposed an equilibrium scour depth equation with considerations of wave action and pile height lower than the water level. The equation is applicable to anyone of following conditions: 1) the KC number is small; 2) the height of pier is lower than the water depth; 3) the pile is relatively wide compared to the water depth. More recently, Simons et al. (2009) presented experimental works on scour development around truncated cylindrical structures. Their results show that depth and extent of scour are largely reduced for the cylinder height less than one cylinder diameter compared to tests with a full water depth cylinder. Besides, their study demonstrated the scour depth concerning tidal flow condition. The tests indicate that scour is remarkably reduced with bi-directional tidal condition compared the equivalent unidirectional current. The flow condition at potential sites plays a crucial role for the scour around the support structure of TCT.

The previous studies demonstrated that the depth of scour for piers or piles is significantly influenced by the geometry of the structure, condition of incoming flow, seabed condition, seabed material, and water depth. These parameters will give the analogous impacts to the seabed scour for the TCT. The rotating rotor of the TCT influences the scour mechanism around the support structures, especially when the rotor is close to the seafloor. The rotor of the TCT becomes an additional factor for the scour process. The well-established knowledge on the turbine wake and ship propeller jets could offer a critical insight on the hydrodynamics of flow disturbed by the rotor.

2.9.2 Applicability of Existing Models for Predicting Scour of TCT

This section aims to identify the appropriateness of existing approaches for predicting scour depth around pile-supported TCT. Many empirical methods are available as presented in section 2.9.2. Rudolph et al. (2004) conducted a comparison between the existing empirical equations and the results of field study and concluded that the empirical equation from Breusers (1977) can be used to predict the scour depth effectively.

Breusers's equation does not include a Froude number in his expression. The inclusion of a Froude number is important as a determination of the nature of flow (Harris et al., 2010). Richardson and Davis (2001) adopted Froude number in his expression. Potential TCT sites have deep water. For an instance, the, the water depth of potential location for tidal energy extraction in Malaysia can up to 93 m (Kota Belud). The Froude number is quite small unlike in river. In the case of deep water, the Froude number may not need to be taken into consideration when comes to the prediction of scour depth. However, the free surface in proximity to rotor allows the water depth to

vary and the consideration of gravity cannot be ignored. The extraction of energy from a flow results in channel head drop. The head drop for a single turbine unit in a large channel is quite small. The effects could be aggravated in array TCT farm. A row of TCTs cause a significant change of water depth in the downstream as well as the increase of flow speed. It subsequently results in pronounced variation in Froude number (Bahaj et al., 2007).

Breusers's (1977) and Richardson and Davis's (2001) equations have been selected as two of the proposed equations to develop an engineering model named scour time evolution predictor (STEP) to predict the development of scour evolution of offshore structures. In STEP, the comparison of these two empirical equations against experimental measurement has been made (Harris et al., 2010), as shown in Figure 2.9. In Figure 2.9, the variation between the empirical equations and the experimental measurements can be found. Harris et al. (2010) stated that the empirical scour depth predictors have a reasonable agreement with the experimental measurements. These empirical equations are a reasonable starting-point to develop a time-varying model, which includes the scour depth due to tide, wave and their combination. This scour time evolution model has been applied in the offshore wind turbine studies.
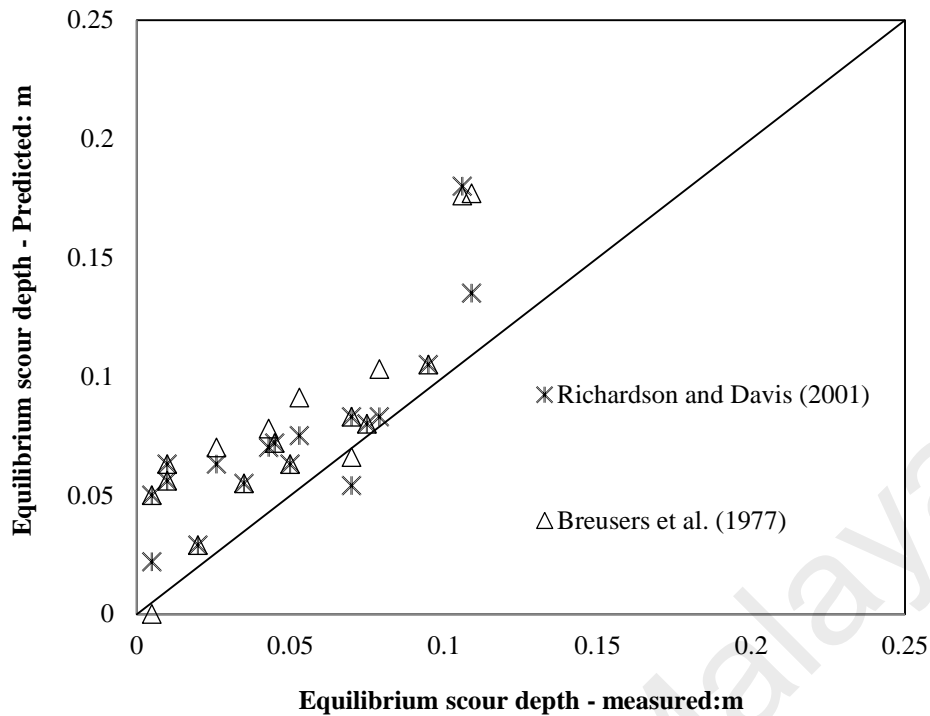
Figure 2.9: The comparison of predicted scour depth with measured scour depth.

Annandale (2006) proposed an approach to estimate the potential erosion of complex soils by relating the stream power (river) to the soil resistance of scour. Harris et al. (2010) applied Annandale's approach to the marine environment with modifications. Harris et al. (2010) called this modified method as Earth Materials approach, which can be used to assess the scour in complex marine soils. Harris's approach requires information of soil properties. The seabed is a formation of soil with different layers, which the depth of each layer needs to be used as an input. The depth of each layers need to be obtained through site investigation. Richardson and Davis's (2001) equation has been adopted to calculate the maximum depth of scour in the Earth Materials approach.

Equations from Breusers (1977) and Richardson and Davis (2001) have been widely used in the prediction of scour depth. If the clearance between the rotor and

seabed is relatively high, the flow suppression at seabed may become insignificant. The consideration of rotor on the seabed scouring is therefore negligible. The equations from Breusers (1977), Richardson and Davis (2001) are still the best equations to date as it has been widely applied in offshore engineering. However, the scour process around the support of TCT is relatively complicated. The development of scour not only depends on a range of tidal, seasonal and long terms variations in currents, wave action and water depth at the site but also the rotating of rotor. No empirical equation to date was found to quantify the influence of rotors to TCT induced scour. It is suggested to include the effect of the rotor in the scour prediction of TCT.

2.9.3 Computational Fluid Dynamic Software and Scour Prediction

Despite many empirical methods for prediction of scour depth are available, Computational Fluid Dynamic (CFD) is getting popular due to its reduction of the cost and time in the simulation process. CFD can also be used to simulate a full-scale structure virtually without consideration of the scaling effect (Zhao et al. 2010). Olsen and Melaaen (1993) was the earliest simulated a three-dimensional scour hole development around the base of a circular pier. Roulund et al. (2005) also numerically simulated local scour around a vertical pile. They suggested that the boundary-layer-thickness-to-pile diameter ratio and the Reynolds number affected the horseshoe vortex and the bed shear stress. However, numerical models for scour require using empirical equations for sediment transport rates which are obtained from experiments.

Deltares, Wallingford and DHI developed many scour models in operation. These models took into account the constantly changing hydrodynamics. Nielsen and Hansen (2007) from DHI Water & Environment developed an engineering model named WiTuS (Wind Turbine Scour). Their model took into account both the constantly changing hydrodynamics and seabed material properties. The simulation results showed that the scour depth will be approximately 0.3 times of pile diameter for the condition of a larger wave period in the North Sea. It is significantly smaller than 1.3 times of pile diameter, which is the industry standard. It demonstrated that larger wave period decreases the scour depth considerably in a combined wave-current condition. Nielsen's colleagues Dixen et al. (2012) developed tables of scour rate to predict long time span of scour around the foundation of the offshore wind farm. Dixen's method can be used to predict the scour development at different stages. The tables of scour rate were developed based on the results from 3D simulations. The development of scour hole with times can be predicted as the flow characteristics at different times are known. The predicted results are in good agreement with the experimental data. The new method can also be used to estimate the backfilling of a scour hole for any given structure (Dixen et al., 2012; Sumer et al., 2012).

Deltares implemented the software "OSCAR" for scour assessment in the tender phase. This software is based on the empirical-mathematical relations. On the other hand, Deltares developed a flexible integrated modelling feature called Delft3D. This modelling feature has a non-hydrostatic option linked to a Z-model approach. It has been successfully implemented in the process of sediment transport. Delft3D-FLOW is now applicable to a wide range of scour problems around the offshore structures

(Deltares). Zhang et al. (2015) developed a numerical model based on commercial CFD package FLOW-3D to simulate the current induced scour around the support of tidal turbine. The model is validated by comparing the numerical results with Zhao et al. (2010). The experiment conducted by Zhao et al. (2010) is a test of seabed scour around a monopile foundation. The comparison does not approve that the numerical model is applicable to investigate the scour induced by tidal turbine. The simulation also only lasts for 30 min. The scour depth does not reach equilibrium state. Investigate the scour depth until it is equilibrium through numerical methods usually take long time.

OpenFOAM as an open source CFD software has been widely applied in today's research and engineering work. Higuera et al. (2013) demonstrated that the OpenFOAM can be successfully simulating some costal engineering cases. Mulualem et al. (2013) developed an Immersed Body Force model via OpenFOAM to examine the performance of a tidal turbine. The greatest advantage of OpenFOAM is that the users are able to modify the source code to satisfy their respective simulation objectives. Liu (2008) also proposed a numerical model FOAMSCOUR through OpenFOAM. It is a numerical model for local scour of pile with the free surface and automatic mesh deformation. The free surface is modelled by VOF method while the scour process is modelled by moving mesh method. Liu (2008) stated that coupled simulations of flow with sediment transport usually take long time. Besides, Harrison et al. (2010) also claimed that a full model of the rotor requires mesh resolution at the blade surface to be sufficient to capture the boundary layer and separation. This requires a very large number of mesh elements and computational efforts. Modelling a rotating turbine also requires that the model be unsteady and the blades change position with every time step.

The incorporation of the rotor into scour model further increases the computational power. The scour mechanism of TCT is more complex than those conventional bridge/pile scour. A combination of physical scale model and CFD model may be alternative to solve the scour issue of tidal turbine in terms of time and cost-effectiveness at the current stage.

CHAPTER 3: METHODOLOGY

3.1 Overview

The main methodologies employed in the study are analytical approach, numerical simulation and physical modelling. The analytical approach is based on the established knowledge from ship propeller jets proposing equations for predicting lateral velocity distribution of the wake (Section 3.2). The numerical simulation focuses on the simulation of the flow field below turbine blades (Section 3.3). The experimental work intends to investigate the scour nature of the TCT (Section 3.4 and Section 3.5). Figure 3.1 shows the flowchart of the overall methodology of the study.

```
                        ┌─────────────────────┐
                        │    Methodology      │
                        └─────────────────────┘
                                  │
          ┌───────────────────────┼───────────────────────┐
          │                       │                        │
          ▼                       ▼                        ▼
┌──────────────────┐   ┌──────────────────────┐  ┌──────────────────────┐
│ Wake model by    │   │ Numerical simulation │  │ Experiment: scour    │
│ analytical       │   │ OpenFOAM:            │  │ evolution of         │
│ derivation       │   │ flow condition       │  │ pile-supported tidal │
│                  │   │ between rotor and    │  │ current turbine      │
│                  │   │ bed.                 │  │                      │
└──────────────────┘   └──────────────────────┘  └──────────────────────┘
          │                       │                        │
          ▼                       ▼                        ▼
┌──────────────────┐   ┌──────────────────────┐  ┌──────────────────────┐
│ Axial momentum   │   │ Geometry creation by │  │ IFREMER-LOMC         │
│ theory,          │   │ Salome, k-e          │  │ turbine with         │
│ equations of     │   │ turbulence model     │  │ Dₜ=0.2m, support     │
│ Hamill (1987),   │   │ with modified        │  │ structure D=0.02m    │
│ empirical        │   │ pimpleDyMFoam solver │  │                      │
│ experimental     │   │                      │  │                      │
│ results of wake  │   │                      │  │                      │
│ recovery         │   │                      │  │                      │
└──────────────────┘   └──────────────────────┘  └──────────────────────┘
          │                       │                        │
          ▼                       ▼                        ▼
┌──────────────────┐   ┌──────────────────────┐  ┌──────────────────────┐
│ Efflux velocity, │   │ Different tip        │  │ Flume in hydraulic   │
│ wake recovery    │   │ clearances,          │  │ lab of University of │
│ rate, lateral    │   │ different number of  │  │ Malaya (1m wide,     │
│ wake equations   │   │ blades               │  │ 1 m high, 16m long)  │
└──────────────────┘   └──────────────────────┘  └──────────────────────┘
          │                       │                        │
          ▼                       ▼                        ▼
┌──────────────────┐   ┌──────────────────────┐  ┌──────────────────────┐
│ Analytical wake  │   │ Axial, tangential    │  │ Different tip        │
│ model for        │   │ and radial           │  │ clearances;          │
│ various ambience │   │ component of         │  │ Time dependent scour │
│ turbulence       │   │ velocity, boundary   │  │ profile (3.5, 7.0    │
│ (TI=3%, 5%, 8%,  │   │ layer                │  │ and 24 hr); Maximum  │
│ 15%).            │   │                      │  │ scour                │
└──────────────────┘   └──────────────────────┘  └──────────────────────┘
          │                       │                        │
          ▼                       ▼                        ▼
┌──────────────────┐   ┌──────────────────────┐  ┌──────────────────────┐
│ Validated by     │   │ Validated by         │  │ Correlated           │
│ comparing with   │   │ comparing with       │  │ time-dependent scour │
│ experimental     │   │ experimental data&   │  │ depth with tip       │
│ data             │   │ mesh independence    │  │ clearance            │
│                  │   │ study                │  │                      │
└──────────────────┘   └──────────────────────┘  └──────────────────────┘
```

Figure 3.1: Flowchart of the research

3.2 Derivation of Analytical Wake Model

3.2.1 Efflux Velocity

The Axial momentum theory is used to derive the efflux velocity equation. Figure 3.2 shows the TCT actuator disc model with the change of current flow pattern in one direction. Due to the assumption that neither the upstream nor the downstream region consist of any work done, the Bernoulli function is applied to the two control volumes on each side of the turbine rotor to produce Equations (3.1) and (3.2). Equation (3.1) shows the relationship between the pressures and velocities upstream of the disc.

$$P_1 + \frac{1}{2}\rho U_1{}^2 = P_2 + \frac{1}{2}\rho U_2{}^2 \tag{3.1}$$

Equation (3.2) shows the relationship between the pressures and velocities downstream of the turbine disc.

$$P_3 + \frac{1}{2}\rho U_3{}^2 = P_4 + \frac{1}{2}\rho U_4{}^2 \tag{3.2}$$

where ρ is the density of the fluid in kg/m^3, P_1, P_2, P_3 and P_4 are the pressures in Pa, and U_1, U_2, U_3 and U_4 are the axial velocities in m/s at the respective locations shown in Figure 3.2.
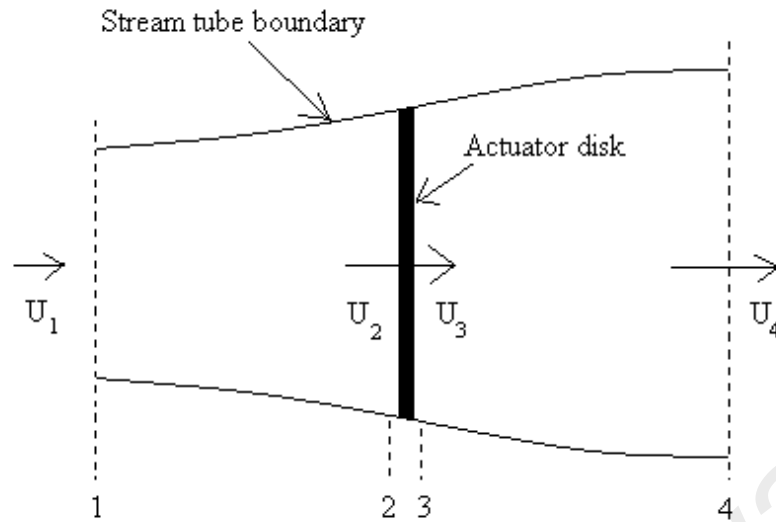
Figure 3.2: A tidal-current turbine actuator disc model.

The thrust is then expressed as the net sum of the forces on each side of the actuator disc as shown in Equation (3.3).

$$T = A(P_2 - P_3) \qquad (3.3)$$

where T is the thrust, A is the area of the actuator disc, and P_2 and P_3 are the respective pressures located at the two side of the turbine disc. It is assumed that the far upstream and far downstream pressures are equal $P_1 = P_4$ and that the velocity across the disc remains the same, $U_2 = U_3$. Equation (4) is obtained by solving $P_2 - P_3$ using Equations (3.1), (3.2) and (3.3).

$$T = \frac{1}{2}\rho A\left(U_1{}^2 - U_4{}^2\right) \qquad (3.4)$$

Lam and Chen (2014) assumed that the dimensional analysis of thrust on the turbine disc, giving consideration to density, rotational speed and diameter, is similar to the dimensional analysis of thrust on the propeller disc. As a result, the deduced thrust coefficient equation is as shown in Equation (3.5).

$$C_t = \frac{T}{\rho n^2 D_t{}^4} \tag{3.5}$$

where C_t is the thrust coefficient, ρ is the density of fluid in kg/m^3, D_t is the diameter of the turbine disc in metres, n is the rotational speed in rev/s, and T is the thrust in Newtons. Equation (3.6) is obtained by equating the thrust equations, Equations (3.4) and (3.5), with the substitution of A by the equation of the area of a circle, $(\pi D_t{}^2)$ /4.

$$C_t \rho n^2 D_t{}^4 = \frac{1}{2}\rho \left(\frac{1}{4}\pi D_t{}^2\right)\left(U_1{}^2 - U_4{}^2\right) \tag{3.6}$$

However, the assumption of simulating the area of the rotor disc as a circle is not satisfactory. The real cross section area of a tidal turbine is rather smaller than the circle. The tidal turbines operate at lower speed compare to ship propellers. In order to eliminate the flaws of the term "A" and rotational speed "n" in the derivation, the authors applied the thrust coefficient of the turbine as Equation (3.7):

$$C_t = \frac{T}{\frac{1}{2}\rho A U^2} \tag{3.7}$$

Equation (3.8) is obtained by equating the thrust equations, Equations (3.4) and (3.7), with the substitution of U by the upstream velocity U_1.

$$\frac{1}{2}C_t \rho A U_1{}^2 = \frac{1}{2}\rho A\left(U_1{}^2 - U_4{}^2\right) \tag{3.8}$$

Equation (3.8) is rearranged to obtain Equation (3.9).

$$U_4 = \sqrt{U_1{}^2 - U_1{}^2 C_t} \tag{3.9}$$

Taking the efflux velocity as V_0 and the free stream velocity as V_∞, substituting into Equation (3.9) produces Equation (3.10).

$$V_0 = V_\infty \sqrt{1 - C_t} \tag{3.10}$$

3.2.2 Wake velocity distribution

The Albertson et al. (1950) applied the axial momentum theory and used a plain water jet to study the velocity distribution within the jet. According to the Gaussian probability distribution and the research work conducted by Albertson et al. (1950), Lam and Chen (2014) proposed Equation (3.11) which could be applied to predict the wake velocity distribution behind the TCT.

$$V_{x,r} = V_\infty - (V_\infty - V_{min})e^{\left[-\left((r+0.081x-(D_t/2))^2/(2(0.081x)^2)\right)\right]} \tag{3.11}$$

Berger et al. (1981) highlighted the presence of hub so that the flow pattern along the ration axis of a ship propeller jet is different from a plain water jet. Hamill (1987) realised the assumption of the plain water jet that the maximum axial velocity at any lateral section occurs at the rotation axis cannot be right. He refined Albertson's (1950) work and suggested two equations (Equations 3.12 and 3.13) to estimate the lateral distribution at cross sections within the zone of flow establishment.

$$\frac{V_{x,r}}{V_{max}} = e^{\left[-(1/2)((r-R_{mo})/(R_{mo}/2))^2\right]} \tag{3.12}$$

Equation (3.12) was applicable to distances up to $0.5D_t$ downstream of the propeller. The distribution of axial velocity for the remainder in the zone of flow establishment can be determined using Equation (3.13).

$$\frac{V_{x,r}}{V_{max}} = e^{\left[-(1/2)((r-R_{mo})/((R_{mo}/2)+0.075(x-R_t)))^2\right]} \tag{3.13}$$

The turbine wake's lateral velocity distribution equation was derived by referring to the research work carried out by Hamill et al. (1987). For the turbine disc, the velocity deficit occurred behind the turbine. The minimum axial velocity, V_{min}, was considered and was included in Equations (3.12) and (3.13) to form Equations (3.14).

$$V_{x,r} = V_\infty - (V_\infty - V_{min})e^A \tag{3.14}$$

when $x \le 0.5Dt$

$$A = [-0.5((r - R_{mo})/(\tfrac{R_{mo}}{2}))^2] \tag{3.15}$$

when $x > 0.5D_t$

$$A = [-0.5((r - R_{mo})/((\tfrac{R_{mo}}{2}) + 0.075(x - R_t)))^2] \tag{3.16}$$

where V_∞ is the free stream velocity, V_{min} is the minimum velocity, R_t is the radius of the turbine disc, D_t is the diameter of the turbine disc, x is axial distance, r is the radial distance. R_{mo} is defined as the location of efflux velocity from the rotational axis.

Lam and Chen (2014) described that the efflux velocity of a turbine is the minimum velocity taken from a time-averaged velocity distribution along the initial turbine face. Equation (3.13) was used to predict the velocity distribution of a ship's propeller jet within the zone of flow establishment. The equation may be invalid for the prediction of wake profile at the region further downstream. The experimental results from Maganga et al. (2010) showed that the minimum velocity will locate at the rotational axis at region $x/D_t>3.0$. Equation (3.6) is initially rearranged as Equations (3.17):

when $0.5D_t < x \le 3.0D_t$

$$A = [-0.5((r - R_{mo})\big/((^{R_{mo}}/_2) + 0.075(x - R_t)))^2] \tag{3.17}$$

It is assumed that the minimum velocity took place at rotational axis as many studies of wake characterisation (Maganga et al., 2010; Pinon et al., 2012; Jo et al., 2014) showed the fact particularly at the region $x/D_t > 3.0$. The term "R_{mo}" in Equation (3.16) is zero to produce Equation (3.18):

when $x > 3.0 D_t$

$$A = [-0.5(r/(0.075(x - R_t)))^2] \qquad (3.18)$$

3.2.3 Position of Efflux Velocity

Lam et al. (2011) reviewed the equations used to predict the position of efflux velocity with a ship's propeller jet. Berger et al. (1981) suggested that the location of maximum axial velocity at the efflux plane can be predicted by the following equation:

$$R_{mo} = 0.67 (R_p - R_h) \qquad (3.19)$$

where R_p is the radius of the propeller and R_h is the radius of the propeller hub. Prosser (1986) further investigated the position of efflux velocity and suggested that the maximum axial velocity in the jet took place at approximately 60% of the blade radius from the hub. Hamill et al. (2004) proposed that the maximum axial velocity occurred at about $0.7(R_p - R_h)$. The above equations used to predict the position of efflux velocity within a ship's propeller jet are being used to predict the location of efflux velocity (V_{min}) at efflux plane of the tidal turbine's wake.

3.2.4 Recovery of Minimum Axial Velocity

The prediction of lateral velocity behind tidal turbines is based on predicting the minimum velocity at various sections. Once the minimum velocity at a certain cross-section is attained, the lateral distribution at the plane can be approximated using the developed equations. The minimum velocity at various sections is not constant. It changes along the downstream as the water in the wake region mixes with ambient fluids. An empirical equation is derived from the experimental data of Maganga et al. (2010) to provide a useful method to predict the recovery rate of minimum velocity at downstream of the turbine wake. The recovery of minimum velocity at downstream of the turbine wake from Maganga et al. (2010) is shown in Figure 3.3
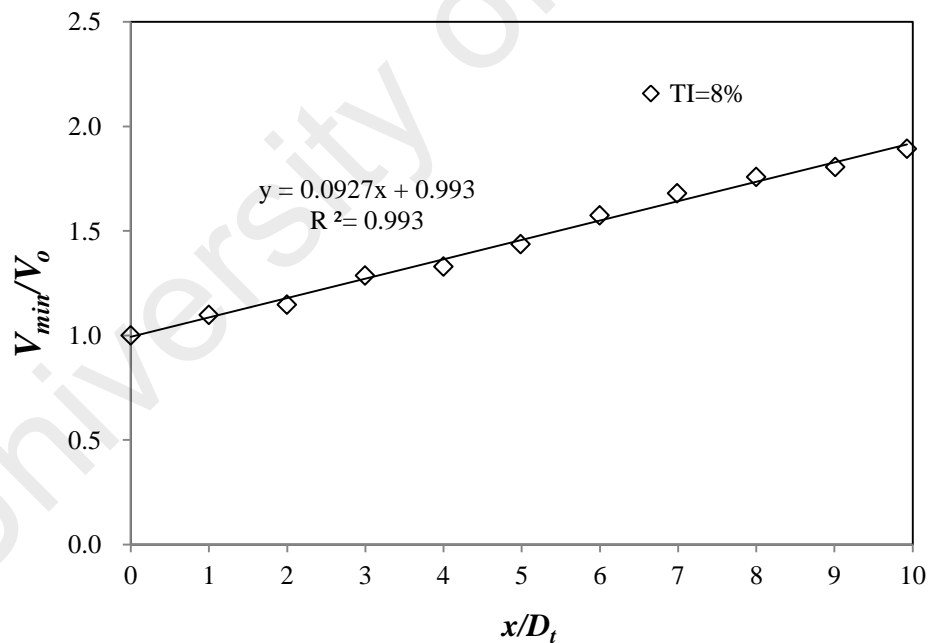
Figure 3.3: Dimensionless minimum axial velocity recovery of turbine wake (TI=8%).

A linear relationship between V_{min}/V_o and x/D_t with correlation coefficient R^2=0.993 is proposed to predict minimum velocity from efflux plane x/D_t=0.

$$V_{min}/V_o = 0.0927 \left(x/D_t\right) + 0.993 \qquad (3.20)$$

Equation (3.20) can be used to predict the minimum velocity along the downstream of turbine wake when the ambient turbulence intensity is approximately 8%. The obtained minimum velocity at each lateral section is an initial input to estimate the lateral velocity distribution.

3.2.4.1 Influence of Turbulence Intensity

The turbulence intensity (TI) is not a globe constant, or even a geographical site constant. According to Mac Enri et al. (2013) presented that the turbulence intensity varies from 3.2% to 7.1% depending on the mean velocity, edd and flood or neap and spring tides. Therefore, the analytical wake model aims to predict wake velocity under various ambient turbulent intensity (TI=3%, 5%, 8% and15%). The turbulence intensity is commonly occurred in the real site. Figure 3.4 presented the dimensionless minimum axial velocity recovery under low turbulence condition (TI=3%). The recovery rate is rather slow in the near wake region (x/D_t<4). The recovery of minimum axial velocity is getting faster in the region x/D_t>4. It may be due to lack of mixing under the low turbulence intensity. Empirical equations are proposed to predict the minimum axial velocity at each lateral section under low turbulence conditions (TI=3%).
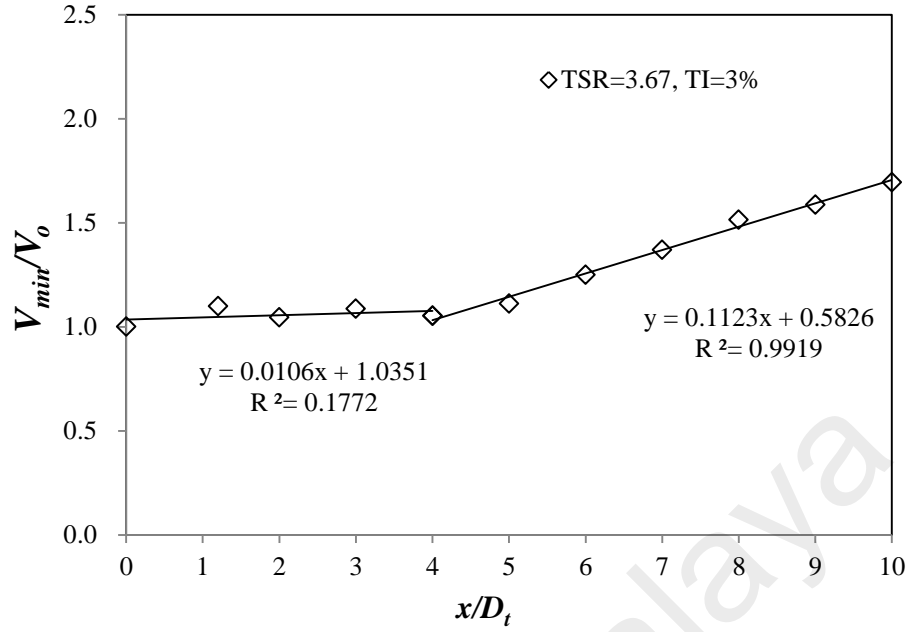
Figure 3.4: Dimensionless minimum axial velocity recovery of turbine wake

(TI=3%)

$$0 < {x}/{D_t} \leq 4$$
$$V_{min}/V_o = 0.0106 \left({x}/{D_t}\right) + 1.0351 \tag{3.21}$$

$$\frac{x}/{D_t} > 4$$
$$V_{min}/V_o = 0.1123 \left({x}/{D_t}\right) + 0.5826 \tag{3.22}$$

Figure 3.5 illustrated the dimensionless minimum axial velocity recovery under ambient turbulence intensity TI=15%. The ambient turbulence is high so that the water in the wake region has strong mixing with ambient fluids. The recovery rate in the near wake region is much faster than that of the previous two conditions. Empirical equations are proposed to predict the decay of minimum axial velocity as follows:

$$0 < \frac{x}{D_t} \leq 4$$

$$\frac{V_{min}}{V_o} = 0.1505 \left(\frac{x}{D_t}\right) + 0.8597 \tag{3.23}$$

$$\frac{x}{D_t} > 4$$

$$\frac{V_{min}}{V_o} = 0.0372 \left(\frac{x}{D_t}\right) + 1.4085 \tag{3.24}$$
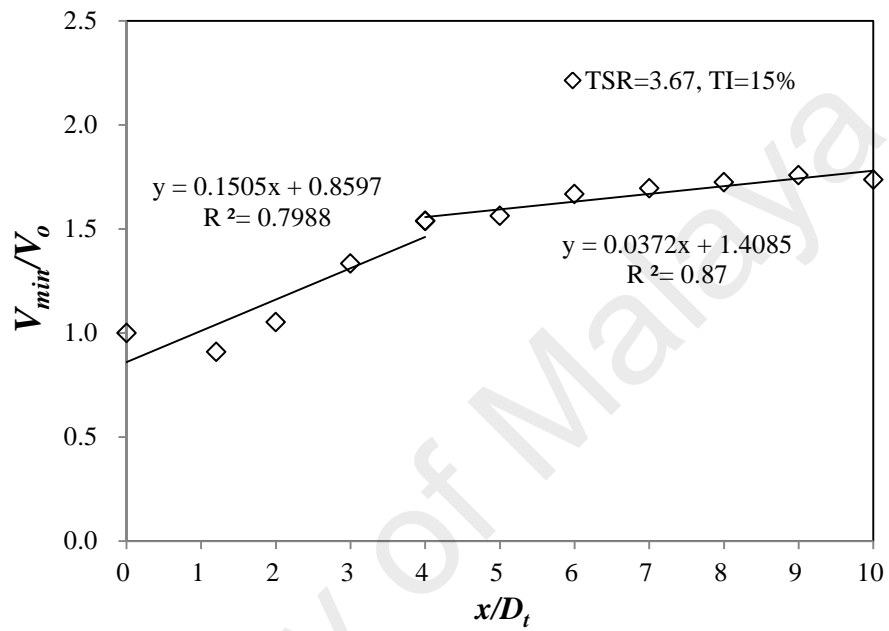
Figure 3.5: Dimensionless minimum axial velocity recovery of turbine wake

(TI=15%)

3.3 Numerical Simulation

3.3.1 OpenFOAM

The OpenFOAM toolbox is a free, open source CFD software package produced by OpenCFD Ltd (OpenFOAM, 2015). The CFD package should be able to provide a reliable prediction of the velocity field around the rotor discs of tidal turbines and able to recreate the turbine geometry similar to the prototype. The OpenFOAM users are able to modify the source code to satisfy their respective simulation objectives. It is a great advantage which makes many challenging simulations of engineering issues achievable. The solver employed in the current study is so called pimpleDyMFoam. It is a transient solver for incompressible, flow of Newtonian fluids on a moving mesh. The solving algorithm is PIMPLE, as it is a new algorithm merged from PISO (pressure implicit with a splitting of operators) and SIMPLE (semi-implicit method for pressure linked equations) algorithms (Higuera et al., 2013). The "DyM" in pimpleDyMFoam stands for dynamic meshes. Hence, it is capable of simulating the rotating movement of turbine rotors. It also can simulate the dynamic mesh refinement along the surface of the turbine blades.

3.3.2 Governing Equations

The governing equations for the fluid are the RANS equations. The details of the equations can be found in the OpenFOAM source code. The equations are solved in ensemble-averaged form, including appropriate models for the effect of turbulence (OpenFOAM, 2015). The turbulence in the fluid is estimated by the standard $k - \varepsilon$ turbulence model (Launder and Spalding, 1972). It is a well-established turbulence

model. The two equations allow the turbulent velocity and length scales to be independently determined. This model is semi-empirical and solved flows based on the assumption that the rate of production and dissipation of turbulent flows are in near-balance in energy transfer. The dissipation of the energy, ε can be expressed as Eq. (3.25):

$$\varepsilon = \frac{k^{3/2}}{l} \tag{3.25}$$

where k represents the kinetic energy of the flow and l is the length scale involved. This is related to the turbulent viscosity, μ_t based on the Prandtl Mixing length model as Equation. (3.26).

$$\mu_t = \rho C_\mu \frac{k^2}{\varepsilon} \tag{3.26}$$

where C_μ is an empirical constant and ρ is the density of the flow. The standard k − ε model uses the following transport equations for k and ε (Equations (3.27) and (3.28)).

$$\frac{\partial(\rho k)}{\partial t} + \text{div } (\rho k \boldsymbol{u}) = \text{div}[\frac{\mu_t}{\sigma_k} grad(k)] + 2\mu_t E_{ij} \times E_{ij} - \rho\varepsilon \tag{3.27}$$

and the ε equation as

$$\frac{\partial(\rho k)}{\partial t} + \text{div } (\rho\varepsilon \boldsymbol{u}) = \text{div}[\frac{\mu_t}{\sigma_\varepsilon} grad(\varepsilon)] + C_{1\varepsilon}\frac{\varepsilon}{k}2\mu_t E_{ij} \times E_{ij} - C_{2\varepsilon}\rho\frac{\varepsilon^2}{k} \tag{3.28}$$

Transient term   Convection term   Diffusion term   Production term   Destruction term

where E_{ij} is the mean rate of deformation of a fluid element in a turbulent flow (Versteeg and Malalasekera, 1995).

The k and ε equations are developed by inserting them into the transport equations. The transport equation has the transient term, convection term, diffusion term, production term and destruction term. The production term in the k equation is to transfer the energy from the mean flow to the turbulence whereas the destructive term is responsible for the dissipation of energy, into heat due to the viscous nature of the flow. The constants in the equations have been given after a wide range of examinations for turbulent flows, where C_μ=0.09; $C_{1\varepsilon} = 1.44$; $C_{2\varepsilon} = 1.92$ $\sigma_k = 1.00$; σ_ε=1.30.

3.3.3 Geometry Creation

The blade geometry of turbine was generated based on the IFREMER-LOMC configuration as shown in Pinon et al. (2012). The origins of the turbine blade were from Tidal Generation Limited. Table 3.1 shows the IFREMER-LOMC configuration of the turbine blade. The turbine blades were designed according to a NACA 63418 profile which has been widely used. The duplication of the turbine blade was done by using the open source software SALOME. The turbine geometry was created in stereo lithography (STL) format and imported to OpenFOAM. Figure 3.6 shows the turbine geometries with different number of blades.

Table 3.1: General blades geometry description for IFREMER-LOMC configuration

Description	IFREMER-LOMC
Rotor radius (R_t)	350mm
Hub radius	46mm
Hub length	720mm
Pitch (set angle)	0°
TSR (Tip Speed Ratio)	3.67
Sense of rotation	Anti-clockwise
Reynolds number	$\approx$280,000

Figure 3.6: The geometry of turbines with different blade numbers.

3.3.4 Boundary and Initial Conditions

Parameters have to be determined before the setting of the boundary and initial conditions. The Tip Speed Ratio (TSR) is one of the parameters and defined as:

$$TSR = \frac{\Phi R_t}{V_\infty} \tag{3.29}$$

where R_t is the turbine radius in meter, Φ is the rotational speed in radian per second and V_∞ is the upstream current velocity in meter per second. The TSR for IFREMER-LOMC case equals to 3.67. According to the radius of the turbine and inlet flow velocity 0.8 m/s, it is known that the turbine rotates at a constant speed of 480 deg/s.

A seabed was virtually created and was modelled using the no-slip boundary condition. The no-slip seabed condition allows the viscous effects of seabed faces and lead to the formation of a boundary layer. The setting of no-slip condition at the bottom wall is due to such a fact that a boundary layer occurs at the seabed in real world case. In addition, the free surface interface between the water and air was not included in the numerical model in order to reduce the computational time. The sliding mesh modelling technique was used in the simulation case. The Arbitrary Mesh Interface (AMI) was applied between the rotor and stator sub-domains. AMI is a technique that allows the numerical simulation across disconnected mesh domains in adjacent region. The domains can be stationary or move relative to one another (OpenFOAM, 2015). The external boundary conditions are tabulated in Table 3.2. The dimensions of the computational domain are 2.86D_t and 2.86D_t, 3.00D_t in the *x-*, *y-* and *z*-directions, respectively (see Figure 3.7). The flow direction is from –*x* to *x*.

Table 3.2: Boundary condition of domain

Designation	Description	Boundary condition
AA1BB1	Inlet	fixedValue
AA1DD1	Side wall	No slip (fixed wall)
DD1EE1	Outlet	inletOutlet
BB1EE1	Side wall	No slip (fixed wall)
ABDE	Top wall	No slip (fixed wall)
A1B1D1E1	Bottom wall	No slip (fixed wall)
G	Turbine	AMI
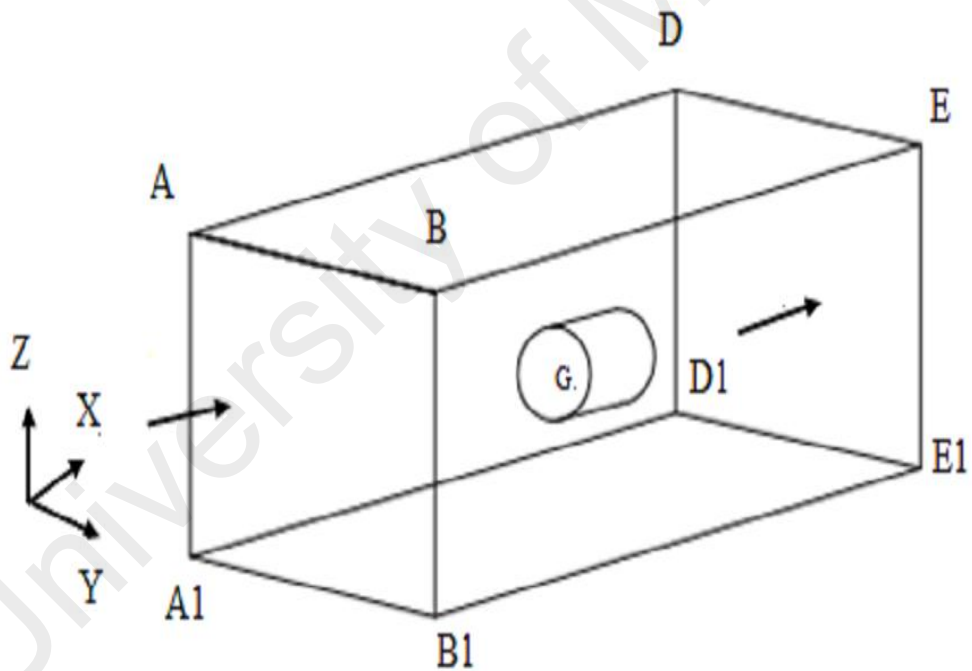
Figure 3.7: The computational domain.

3.3.5 Meshing

The meshing of the rotor and stator domain was done by executing the SnappyHexMesh utility code. The snappyHexMesh utility generates 3-D meshes containing hexahedra (hex) and split-hexahedra (split-hex) automatically from triangulated surface geometries in STL format. The mesh approximately conforms to the surface by iteratively refining a starting mesh and morphing the resulting split-hex mesh to the surface (OpenFOAM, 2015). The rotor mesh density is higher than the stator mesh density to produce a better texture of the turbine blade surface during meshing. The validity of the mesh has been checked through commanding the utility "checkMesh". The output reported the mesh quality is satisfactory. The slice section of the mesh is shown in Figure 3.8.
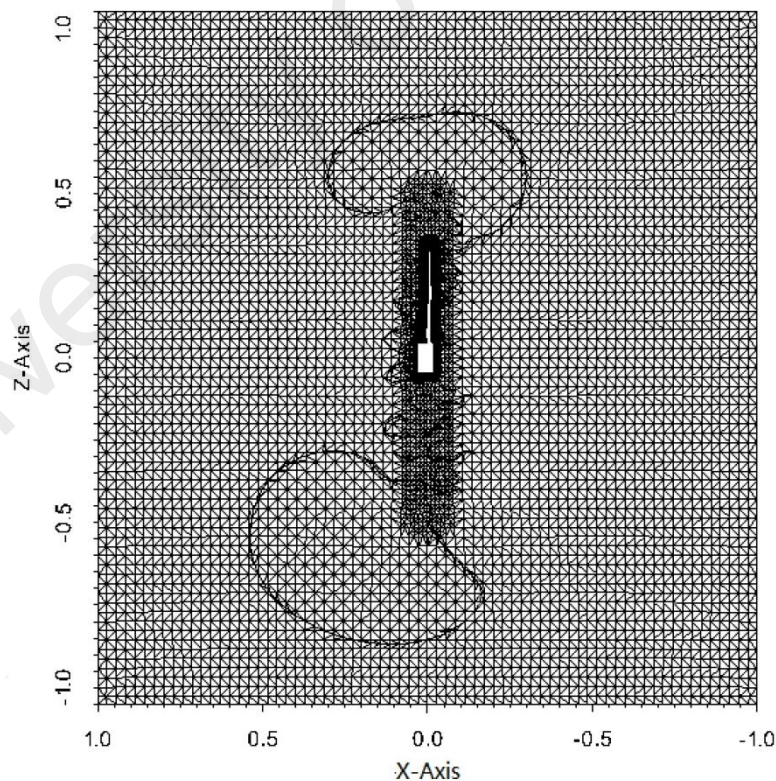
Figure 3.8: Slice section of the mesh domain along the X-axis direction

3.4 Experiment Set-up for Scour Test

A series of clear water scour tests have been performed in the Hydraulic Laboratory of University of Malaya, Malaysia. The flume is 16 m long and 1 m wide, built with transparent glass wall for flow visualization (See Figure 3.9). The turbine positioned 5 m downstream of the channel origin (x=0 m). The incoming flow was conditioned using a porous mattress to break the turbulence structures created from the pump and supply pipes, therefore offering uniform flow for the test section. The turbine support tower and nacelle were made from PVC pipe. The turbine rotor was fabricated by rapid prototyping using ABS material. The turbine was outfitted with a miniature DC motor for voltage measurements. Reasonable tip speed ratios were maintained by the internal resistance of the device. The flow depth was maintained by the tailgate, while the water was supplied by three pumps.
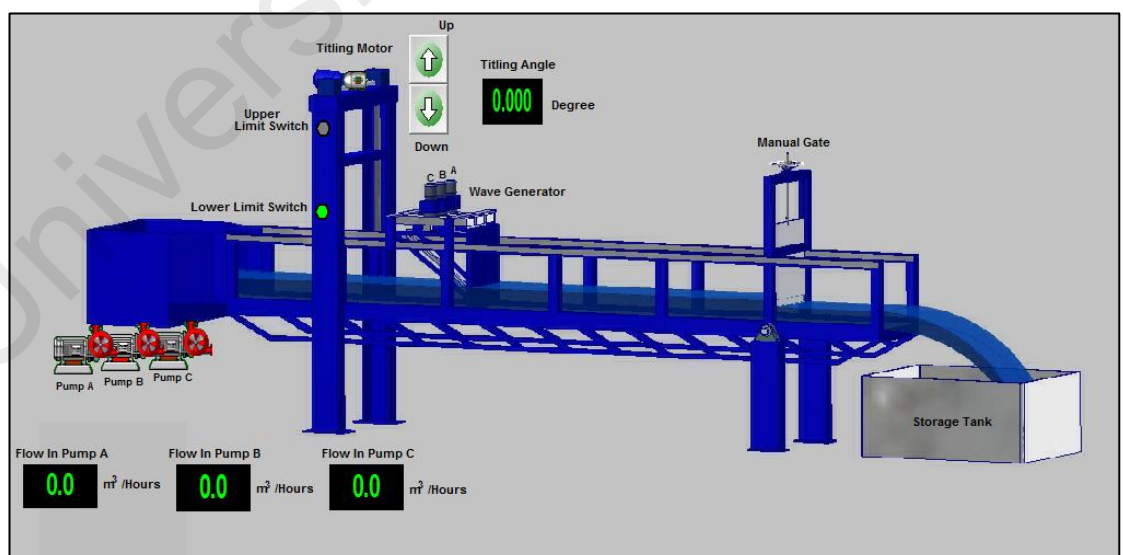
Figure 3.9: Tilting flume in Hydraulic Laboratory, University of Malaya

The turbine model used during the experimental testes was a three bladed axis flow turbine with rotor diameter D_t = 0.2 m. The diameter of the turbine support tower was 0.02 m. The flow depth 0.45 m was maintained by adjusting the tailgate at the end of flume. The approaching velocity 0.23 m/s was also maintained constantly during the experiments. The velocity of the incoming flow is monitored by the 2D mini LDV system (See Figure 3.10). At 1:70th geometric scaling the experiments in the scour investigation represents a 14 m diameter turbine in water depth of 31.5 m and applying Froude similitude, a mean velocity of 1.92 m/s. The experimental scaling issue of tidal turbine has been highlighted by Harrison et al. (2010) and Myers and Bahaj (2010). High Froude numbers often take place in laboratory that may lead to alteration of water surface. Froude similarity is normally maintained between model system and prototype. Myers and Bahaj (2010) also stated that discrepancy in Reynolds numbers between prototype and model is acceptable for the scaling of hydraulic channels under the following two conditions: 1) Froude similarity is maintained; 2) both full-scale and model Reynolds numbers are within the same turbulent region.

A sediment recess 0.1 m deep, 5.0 m long and 1.0 m wide was constructed inside the flume. Before commencement of each experiment, the sediment was first levelled using a sand leveller. The turbine position and test section were selected to be within an area where the flow and the underlying bed topography were sufficiently far from inlet and outlet of the flume. During the tests, the TCT was embedded in the middle of the bed sediment recess. The flume was slowly filled with water from both upstream and downstream pipes at a low rate. It prevents the disturbance of the levelled sand bed. Once the predetermined water depth was reached, the pump will be on and the experimental run was started by adjusting the flow rate at the inlet.

The water was carefully drained off from the flume at the end of each test to prohibit the disturbance to the scour profiles. The scour profiles around the pile-supported TCT are measured by a laser distance meter with an accuracy of 0.1 mm. The laser distance meter measured the bed elevation for each 1 cm in length and 1 cm in width. The detailed parameters of the experiments are presented in Table 3.3.

Figure 3.10: mini LDV measurement system

The geometric standard deviation was calculated from $\sigma_g = (d_{84}/d_{16})^{0.5} = 1.3$ which is smaller than 1.4. It is indicating that the sand was uniformly graded (Barkdoll et al. 2007). The flow depth was also set to ensure approach section the incoming flow velocity at the approach section (u_f) was below the critical incipient velocity (u_{cr}) ($u_f<u_{cr}=0.032$ m/s, for the sand bed-material of $d_{50}=1.0$ mm) based on the Shield curve (Wu and Wang, 1999). Figure 3.11 presents a schematic diagram of the test section, turbine and instrumentation used during the experimental tests. Figure 3.12 illustrates the photo of turbine model and flume.

Table 3.3: Turbine, flow flume and sediment parameter used during the experiment

Variable	Value
Turbine parameters	
D_t (m)	0.2
Hydrofoil	NACA 63418
Hub length (m)	0.1
C/D_t	0.25, 0.50, 0.75
TSR	4.2
Flow, flume and sediment parameters	
H (m)	0.45
Q_w (m^3/s)	0.117
b (m)	1.0
δ (%)	7
F_r	0.11
R_b	1.04×10^5
R_T	4.6×10^4
$V\infty$ (m/s)	0.23
u_{cr} (m/s)	0.032
d_{50} (mm)	1.0
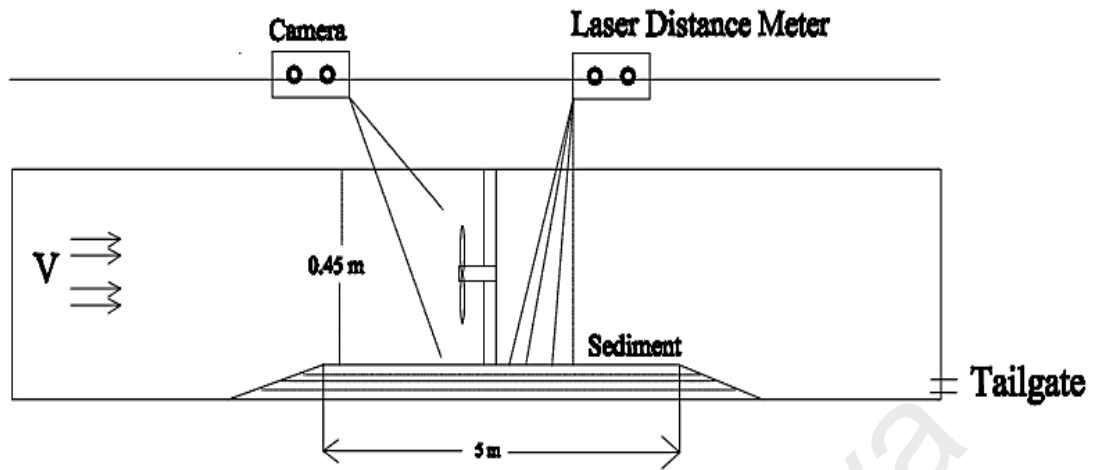
Figure 3.11: Schematic view of scour experiment

Figure 3.12: Photo of turbine model ($D_t = 0.2$ m) and flume

CHAPTER 4: RESULTS AND DISCUSSION

4.1 Overview

This chapter documents the results and relevant discussion of the study. Section 4.2 shows the validation of the proposed model. Despite the direct comparison of predicted velocity with experimental data, a goodness of fit test is also conducted to testify the level of accuracy of the proposed model. Section 4.3 documents the characterization of the flow below turbine rotor. Axial, radial and tangential component of velocity below the turbine rotor are illustrated. Section 4.4 presents the scour evolution and profile around the support structure of tidal current turbine.

4.2 Wake Prediction

4.2.1 Position of Efflux Velocity

The experimental results from Maganga et al. (2010), Pinon et al. (2012) and Mycek et al. (2014) are used for the validation of the proposed wake model. The turbine incorporated in their experiments is based on NACA 63418 and the general geometrical properties of the turbine are shown in Table 4.1. The calculated locations of minimum velocities (R_{mo}) in the turbine wake are tabulated in Table 4.2. The R_{mo} was initially assumed to be 0.2.

Table 4.1: General geometric properties of turbine

Rotor diameter	350 mm
Radius of hub	46 mm
Number of blades	3
Position of rotor relative to flume tank	Upstream
Pitch angle (degree)	0

Table 4.2: Position of efflux velocity

Equation	R_{mo}
Berger et al. (1987), R_{mo}=0.67 (R-R_h)	0.20
Prosser (1986), R_{mo}=0.6R	0.21
Hamill et al. (2004), R_{mo}=0.7 (R-R_h)	0.21

4.2.2 Comparison of Results with Previous Model and Experimental Data

The study conducted by Maganga et al. (2010) has been chosen to further testify the validity of the proposed wake model. The previous proposed analytical equation by the Lam and Chen (2014) has also been incorporated in the comparison. Figure 4.1 (a-f) illustrates the comparison of experimental measurements and the theoretical predictions by the authors. The experimental work conducted by Maganga et al. (2010) suggested the wake profiles have two dips at x/D_t=1.0 and x/D_t=2.0.
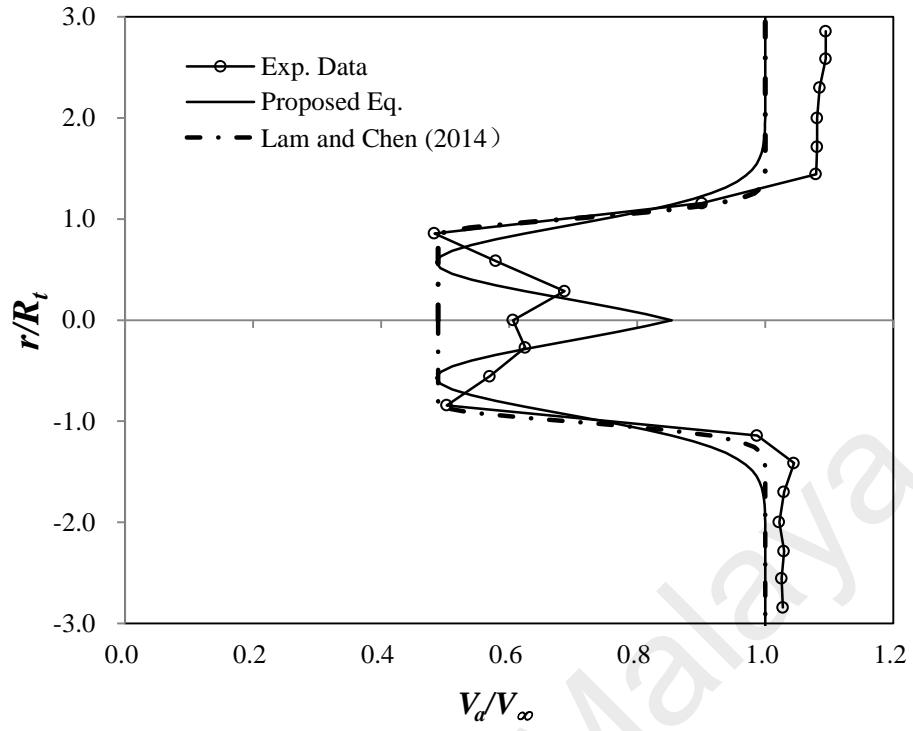
a. x/D_t=1.0
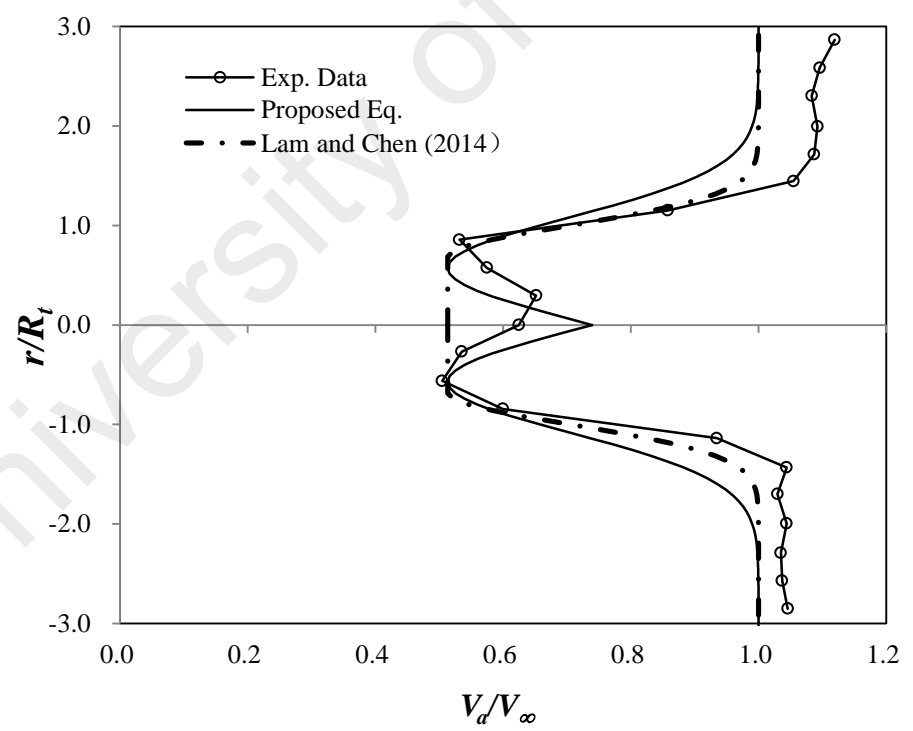
b. x/D_t=2.0

Figure 4.1: Validation of the proposed analytical wake model: (a) x/D_t=1.0; (b) x/D_t=2.0; (c) x/D_t=3.0; (d) x/D_t=5.0; (e) x/D_t=7.0 and (f) x/D_t=9.0

c. x/D_t=3.0

d. x/D_t=5.0

Figure 4.1, continued.

e. x/D_t=7.0

f. x/D_t=9.0
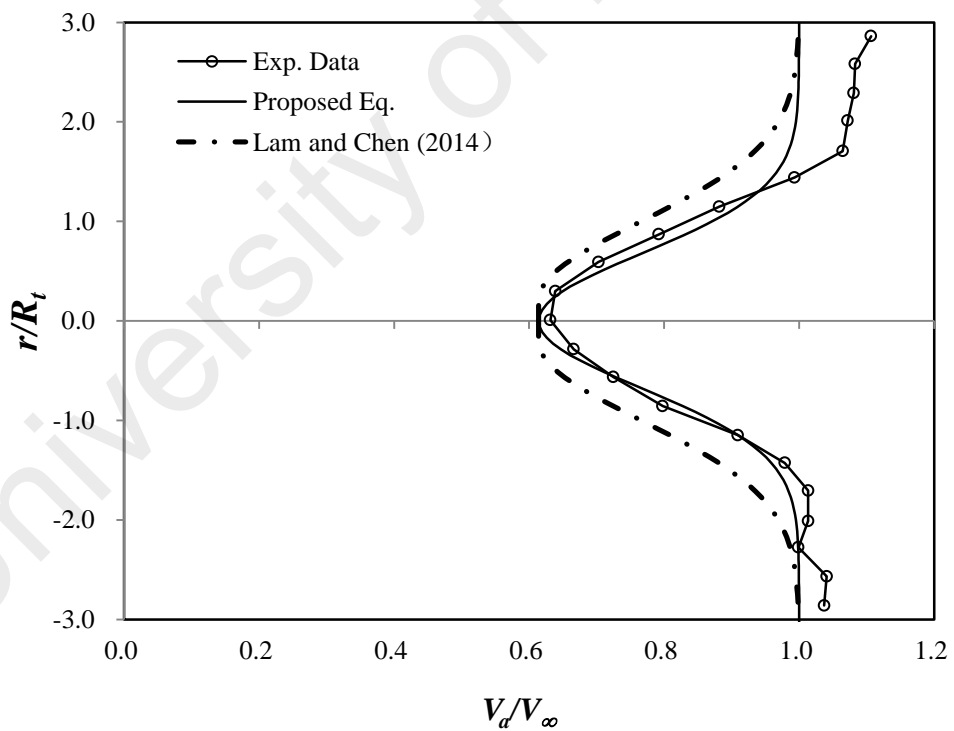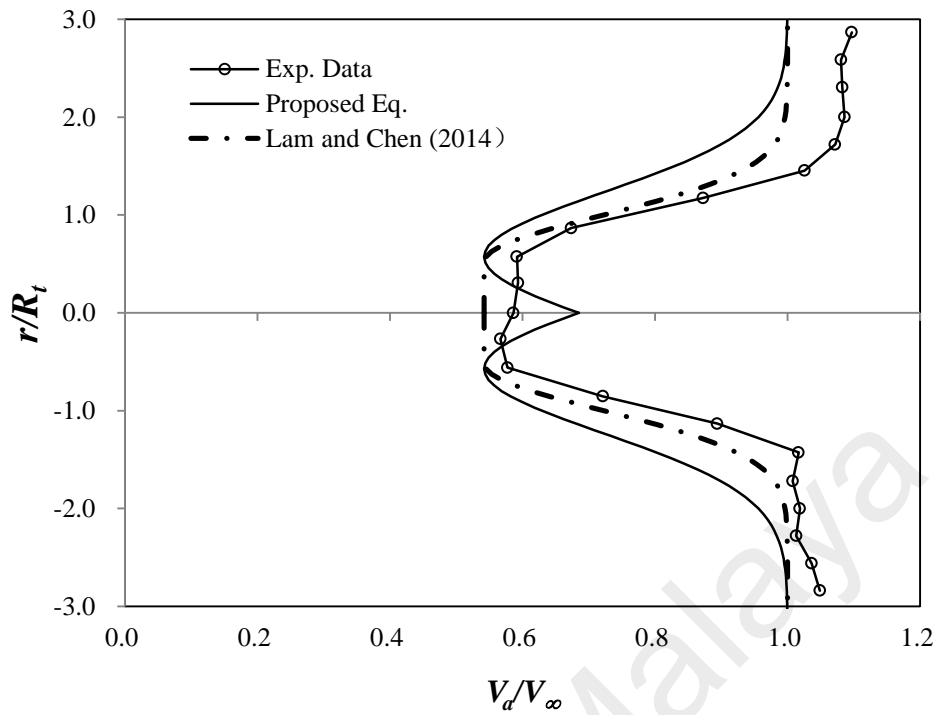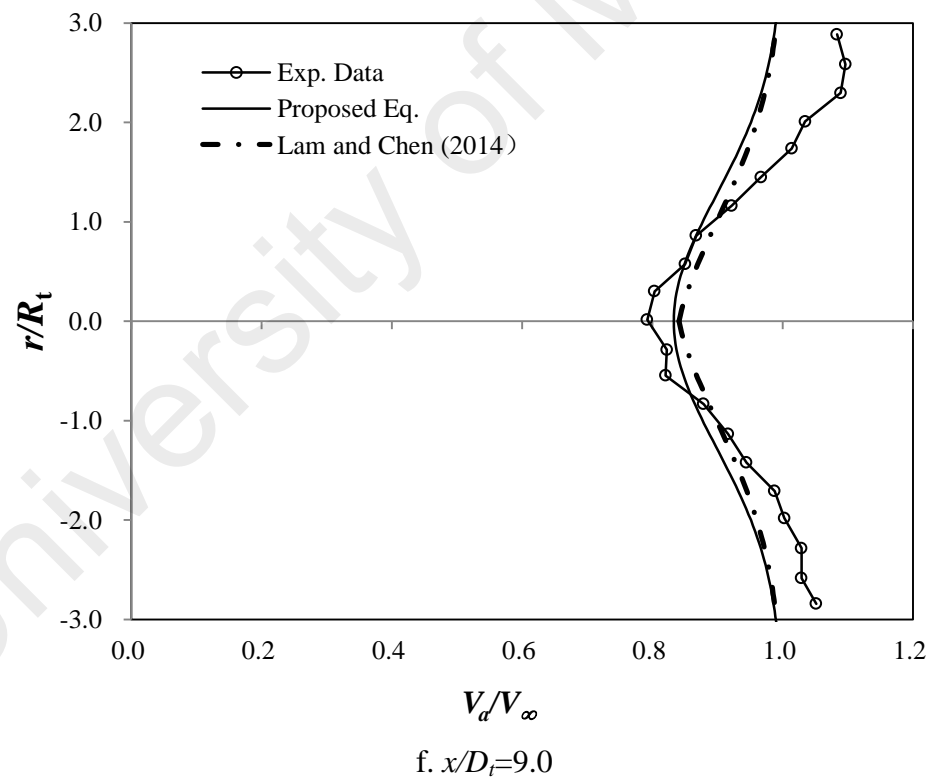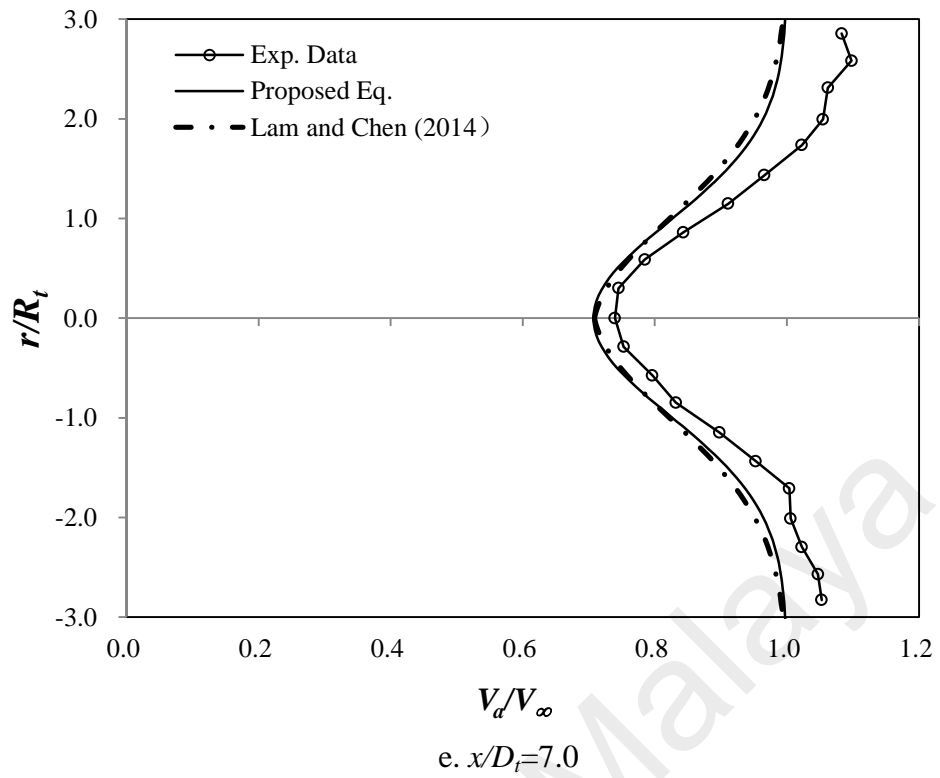
Figure 4.1, continued.

Lam and Chen (2014) discussed this issue based on the experience of ship propeller jets. The influence of the hub disappears gradually along the longitudinal axis due to penetration of high velocity fluid into low velocity central core. The fluids in the ship propeller jet are mixing with the surrounding water both inwardly and outwardly along the rotational axis (Lam et al., 2011). The fluids only mix outwardly at a certain distance downstream where the ship propeller jet is fully expanded. There is only one maximum velocity peak located at the axis of rotation in the zone of established flow (Lam et al., 2011). The dips in the turbine wake also disappear gradually along the longitudinal axis. There is only one minimum velocity located at the rotational axis at further downstream of wake region.

It was noticed that the new theoretical predicted curve at x/D_t=1.0, x/D_t=2.0 and x/D_t=3.0 fits the measured curve principally. The region of r/R_t=1.2 to 3.0 and -1.2 to -3.0 showed some discrepancies between the new theoretical and experimental values of mean streamwise velocity. The largest variation of the theoretical mean streamwise velocity of this region was approximately 8% compared with experimental results. The variation in percentage is calculated by applying the formula shown in Equation (4.1).

$$Variation\ (\%) = \frac{Experimental\ measurement - Theoretical\ prediction}{Experimental\ measurement} \times 100\% \qquad (4.1)$$

This discrepancy might be due to the effect of the free surface. The water surface in the experimental flume may have fluctuation. The support structure of the turbine may be another contributor to the variation. The comparison of experimental results and theoretical predictions at the rotational axis also showed inconformity. The disagreement at the rotational axis at x/D_t=1.0 is high, which is approximately 25%. The high discrepancy at this region might be due to the hub. The length of the hub is equivalent to one diameter of the turbine. The predictions of the new analytical equation

72

and experimental data have a good agreement at the rotational axis at x/D_t=2.0 and x/D_t=3.0.

The newly proposed Equation (3.14) has an advantage over the equation suggested by Lam and Chen (2014). The derivation of the equation from Lam and Chen (2014) is based on the axial momentum theory and plain water jet. In reality, the velocity characteristic of a ship's propeller jet is more complicated than a plain water jet. The dips appearing in the figures were therefore not able to be predicted by the equation proposed by Lam and Chen (2014). The minimum velocities uniformed the velocities in the region from r/R_t=-0.8 to 0.8 in Figures 4.1(a)-4.1(c). The new analytical wake model is a refinement of the previous equations. It is able to predict the lateral velocity distribution behind tidal current turbine with the appearance of dips in the near wake region.

Figure 4.1(e)-4.1(f) illustrate the properties of the lateral velocity distribution at 5.0 D_t, 7.0 D_t and 9.0 D_t downstream, respectively. The wakes are fully expanded and there is only one minimum velocity located at the axis of rotation. The experimental measurements of the wake profiles at downstream distances of 5 D_t, 7.0 D_t and 9.0 D_t produce a classical Gaussian distribution shape. The new wake model is also able to predict the velocity distribution at these locations. The new theoretically predicted curve at the lateral distance x/D_t =5.0 fits the experimental measurement curve well. It has better predictions compared to the previous equations proposed by Lam and Chen (2014). The prediction at the region from r/R_t=0 to r/R_t=-1.0 nearly overlaps with experimental data. The largest variation in mean stream wise velocity between the experimental results and the theoretical predictions is approximately 7%, which is 2% less than the equation proposed by Lam and Chen (2014). The prediction of lateral velocity distribution at x/D_t =7.0 and x/D_t =9.0 has equal performance as the previously

proposed equation. No evident deviation is observed among the two theoretical predictions.

4.2.3 Influence of Turbulence Intensity

4.2.3.1 Turbulence Intensity (TI=3%and 5%)

The experimental results from Mycek et al. (2014) have been chosen to testify the applicability of the proposed equation under ambient turbulence intensity (TI=3%). Wake growth rate c was introduced and is replacing the constant 0.075 in Equation (3.16). Figure 4.2 demonstrates the comparison of predicted wake profile with experimental results under turbulence intensity of 3%. The wake growth rate c=0.065 is suggested to fit the experimental data. The experimental conducted by Pinon et al. (2012) which with 5% ambient turbulence intensity also incorporated in the comparison. The wake shape of the experimental results under TI=3% and TI=5% have similar manner. The variation of these two turbulence levels is not significant. Another possible explanation for this phenomenon is that the ratio of the ambient turbulence intensity to the turbulence added by the tidal turbine itself is small. It is, therefore, the incoming turbulence does not result in many differences in the mixing process. The predicted lateral velocity distributions are in acceptable agreement with experimental results. The major discrepancy occurred at the rotational axis at x/D_t =1.2, x/D_t =2.0 and x/D_t =3.0. It might be due to the flow disturbance caused by the hub.
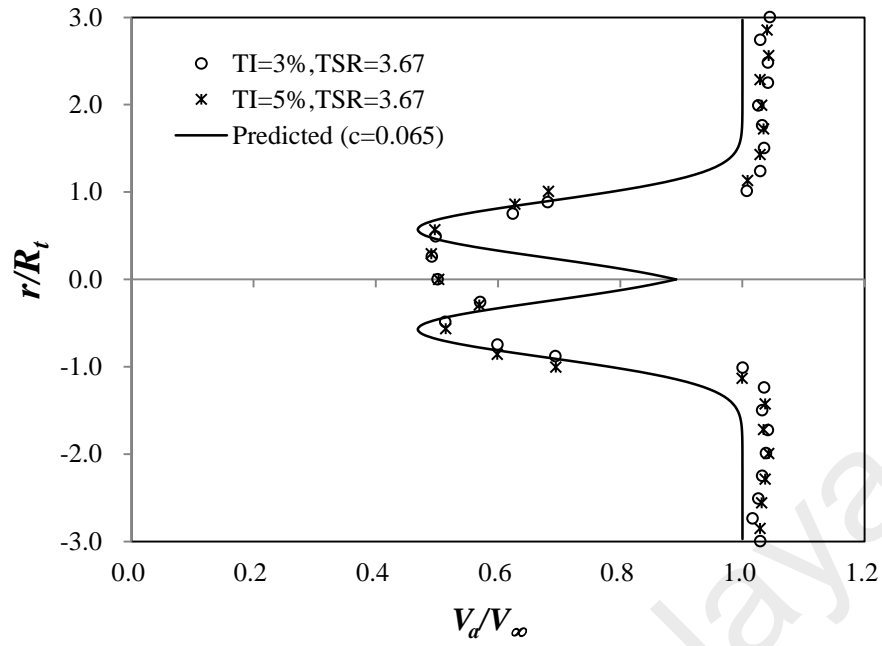
a. x/D_t=1.2
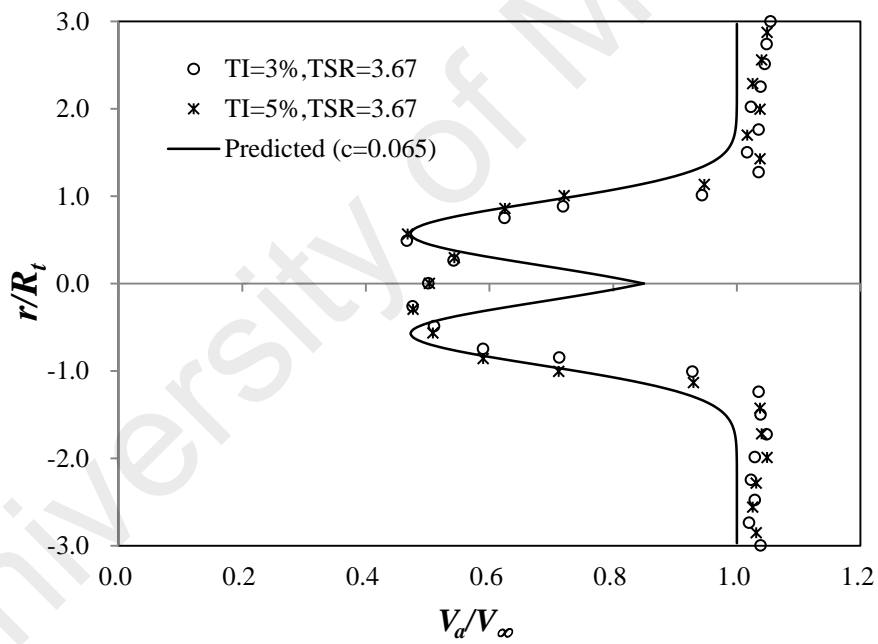
b. x/D_t=2.0

Figure 4.2: Comparison of the wake shape between experimental (TI=3%) and predicted values: (a) x/D_t=1.2; (b) x/D_t=2.0; (c) x/D_t=3.0; (d) x/D_t=4.0; (e) x/D_t=5.0; (f) x/D_t=6.0; (g) x/D_t=7.0 and (h) x/D_t=8.0.
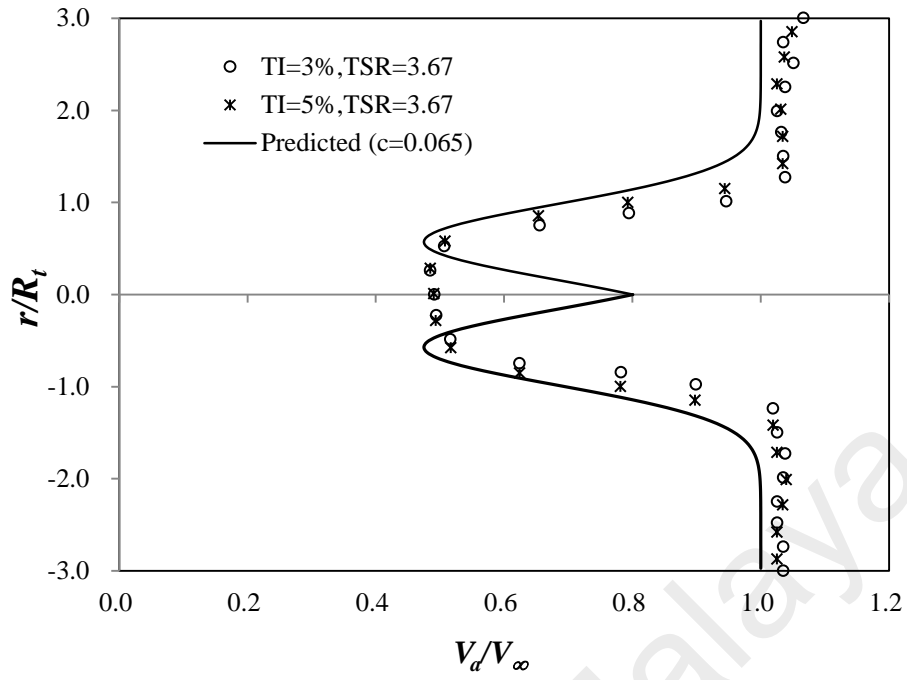
c. x/D_t=3.0
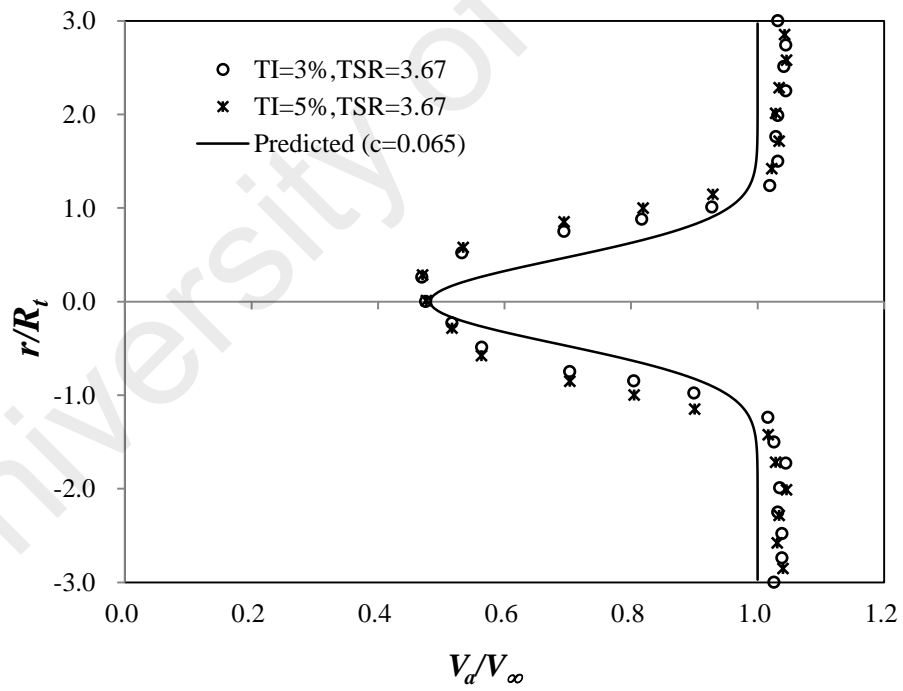
d. x/D_t=4.0

Figure 4.2, continued
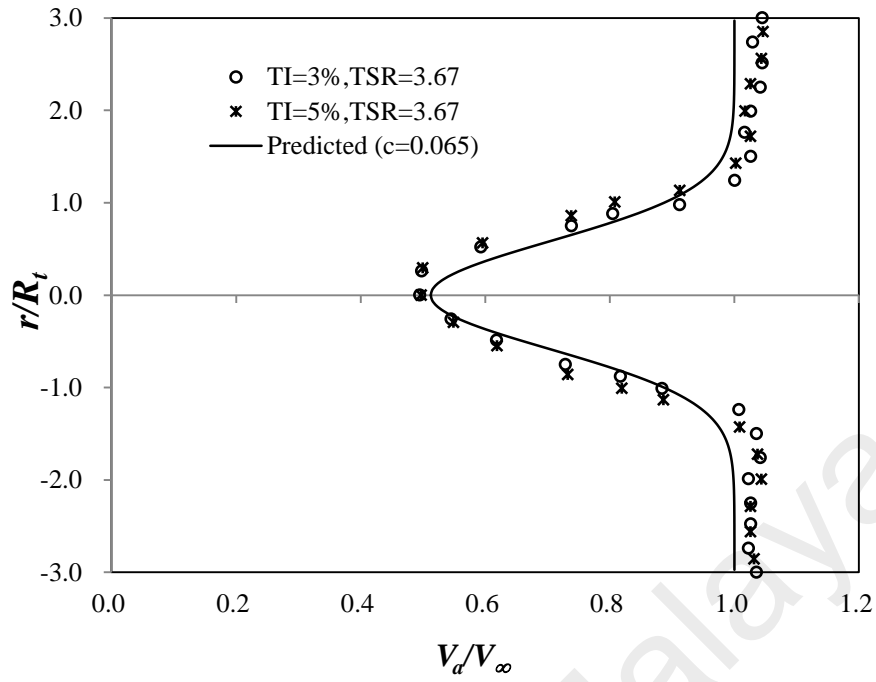
e. x/D_t=5.0
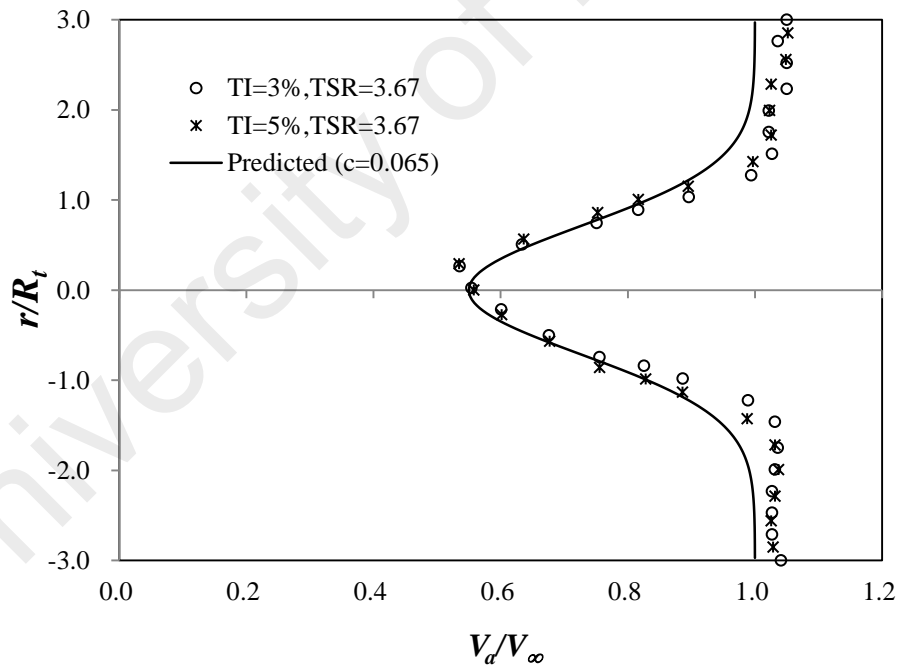
f. x/D_t=6.0

Figure 4.2, continued.

g. x/D_t=7.0

h. x/D_t=8.0
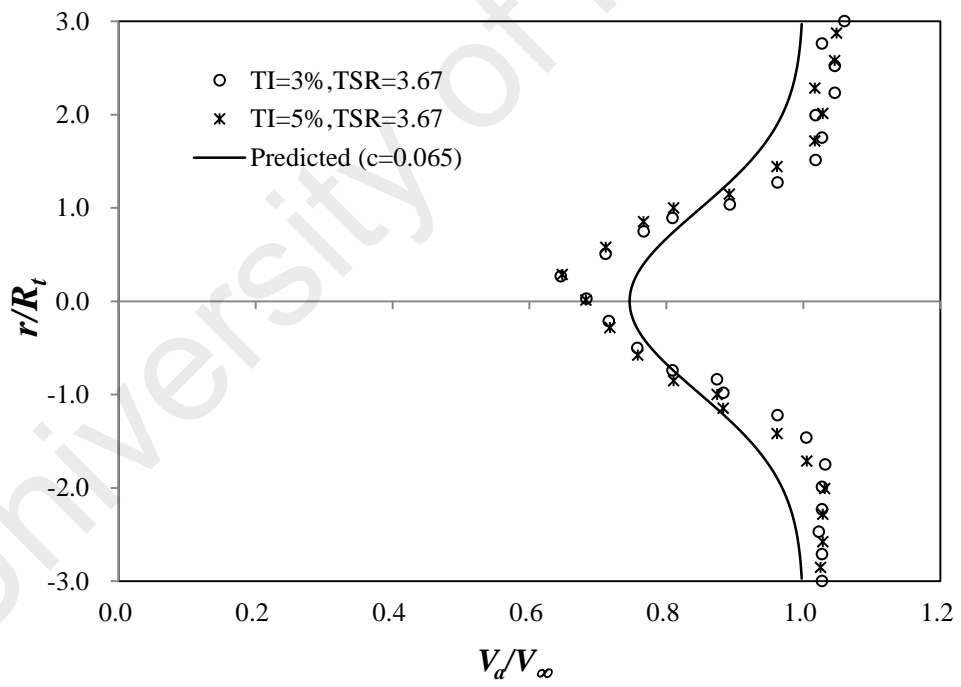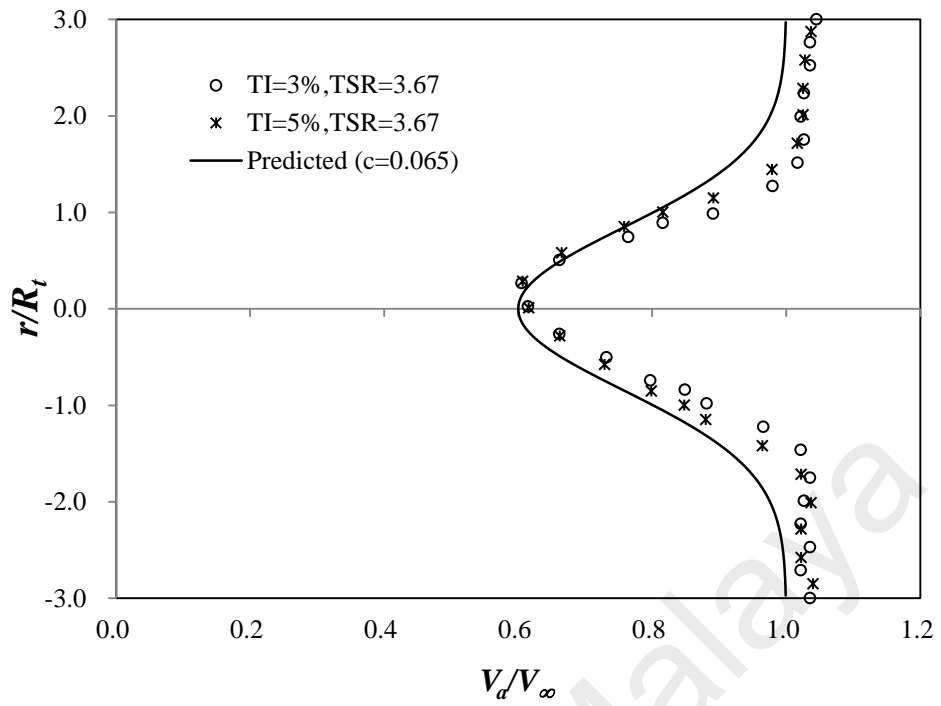
Figure 4.2, continued.

4.2.3.2 High Turbulence Intensity (TI=15%)

Figure 4.3 demonstrates the comparison of predicted wake profile with high ambient turbulence intensity (TI=15%). The experimental data of velocity distribution at these locations have not shown the appearance of two dips. The two dips merged as one dip at the region near to the rotational axis. The strong mixing of the wake with ambient fluids results in the earlier disappearance of two dips. Equation (3.14) and (3.18) are used to predict the wake profile at high turbulence level. The proposed curve shows discrepancies at x/D_t=1.2, x/D_t=2.0 and x/D_t=3.0. It overestimates the velocity from r/R_t=0 to r/R_t=1.0. The water in the wake region has strong mixing with ambient fluids. The water is highly turbulent and the properties are not feasible to be measured. Numerical technique is recommended to capture the disappearance of two dips at high ambient turbulence intensity. However, the predicted wake shapes are in line with the velocity distribution at far wake region under TI=15% (x/D_t =4.0, 5.0, 6.0, 7.0 and 8.0). The wake recovers rapidly at this turbulence level and the mixing in the far wake region tends to be weaker.
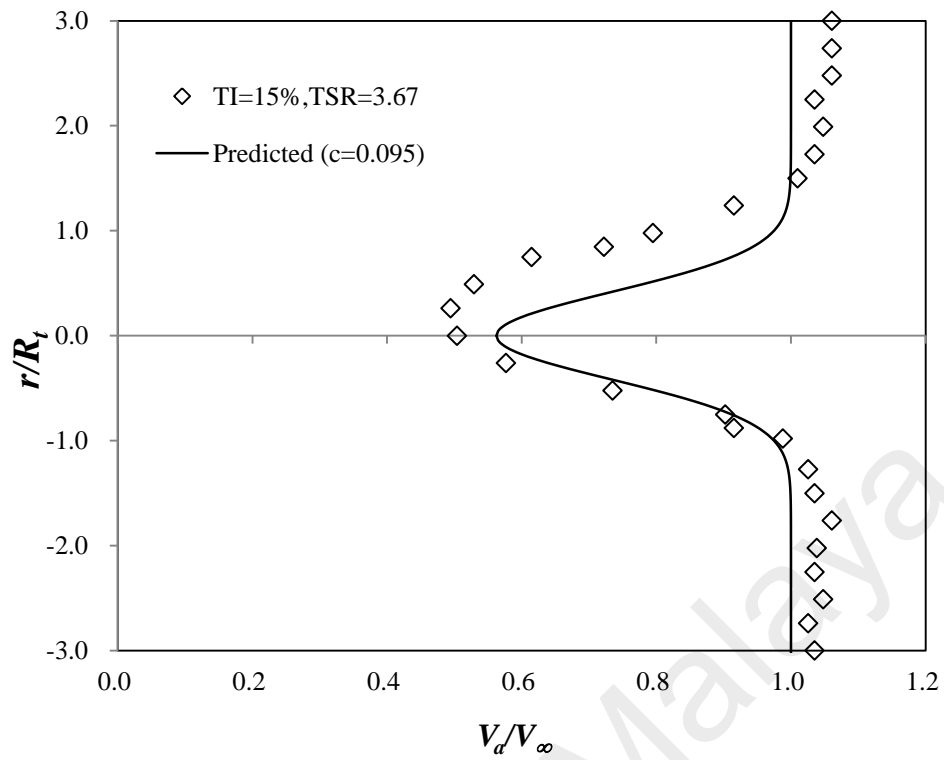
a. x/D_t =1.2
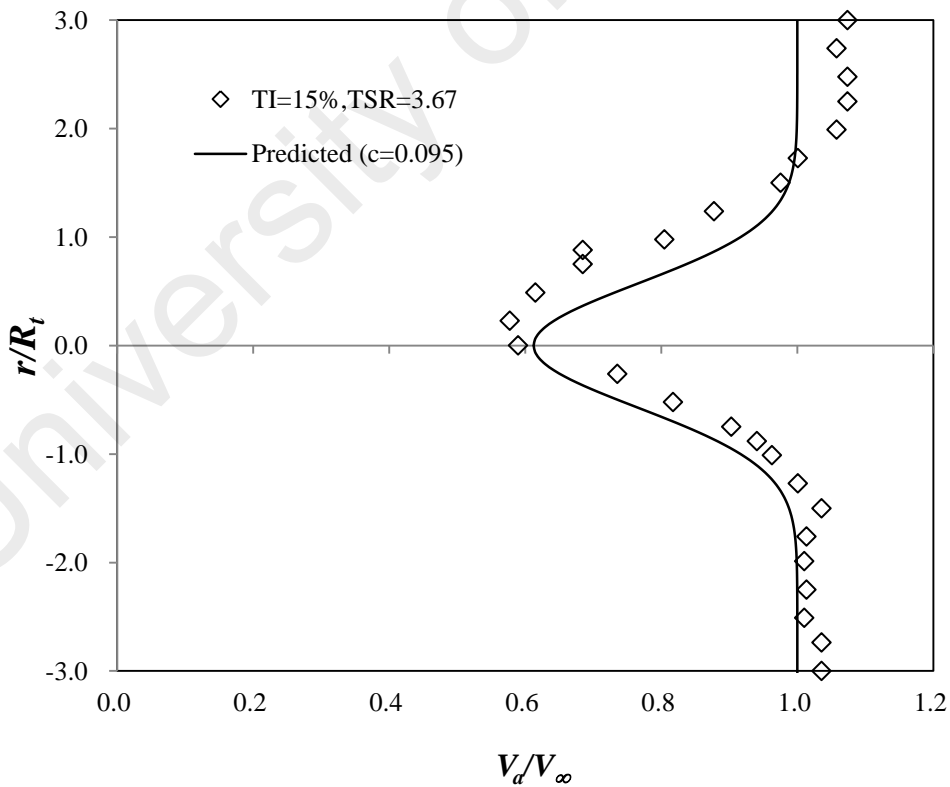
b. x/D_t =2.0

Figure 4.3: Comparison of the wake shape between experimental (TI=15%) and predicted values: (a) x/D_t =1.2; (b) x/D_t =2.0; (c) x/D_t =3.0; (d) x/D_t =4.0; (e) x/D_t =5.0; (f) x/D_t =6.0; (g) x/D_t =7.0 and (h) x/D_t =8.0
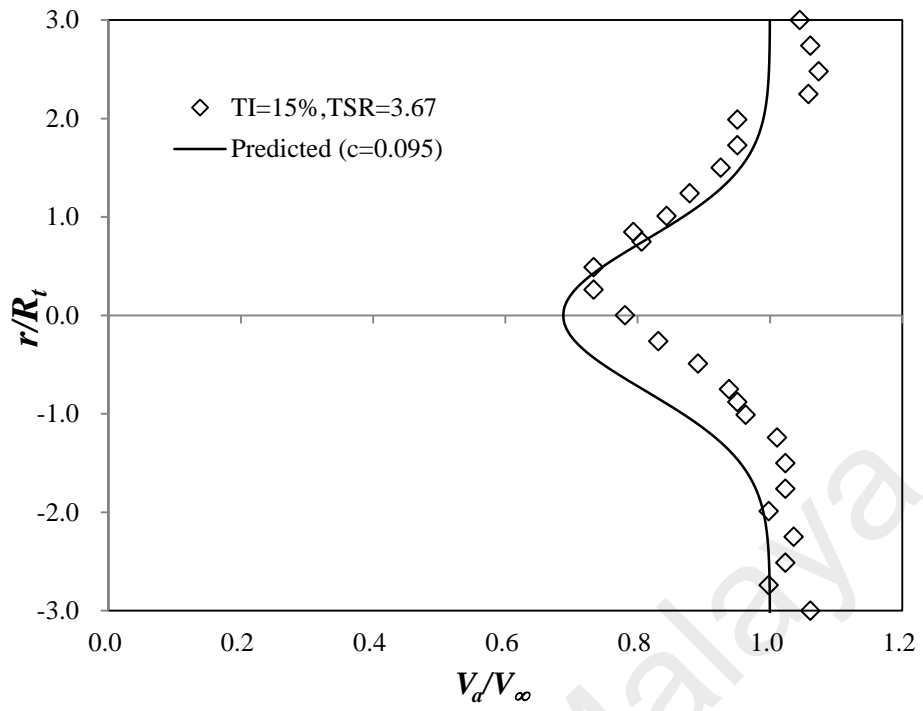
c. $x/D_t = 3.0$
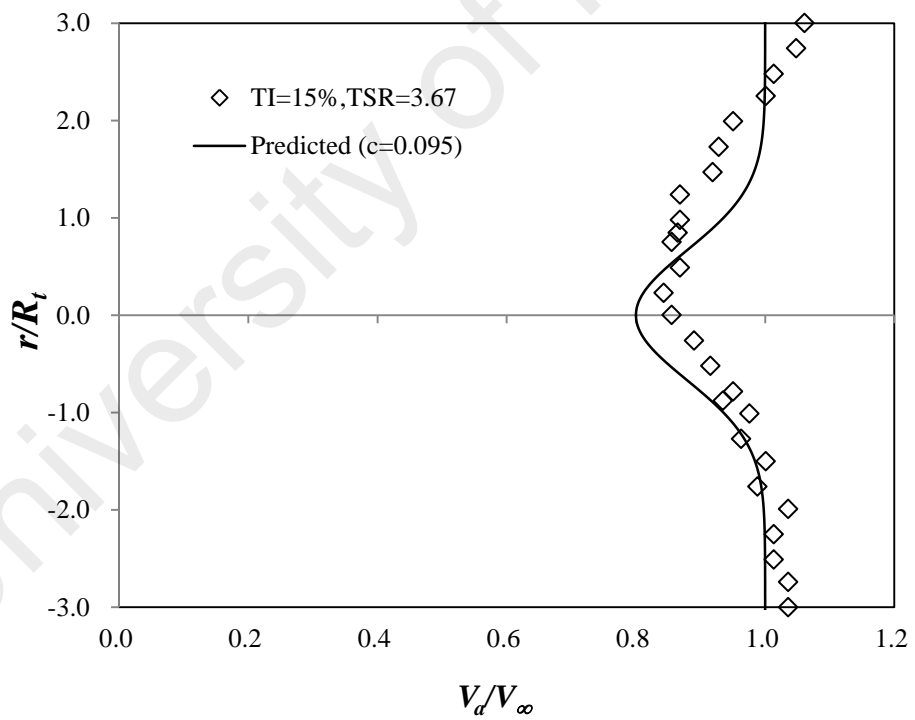
d. $x/D_t = 4.0$

Figure 4.3, continued.
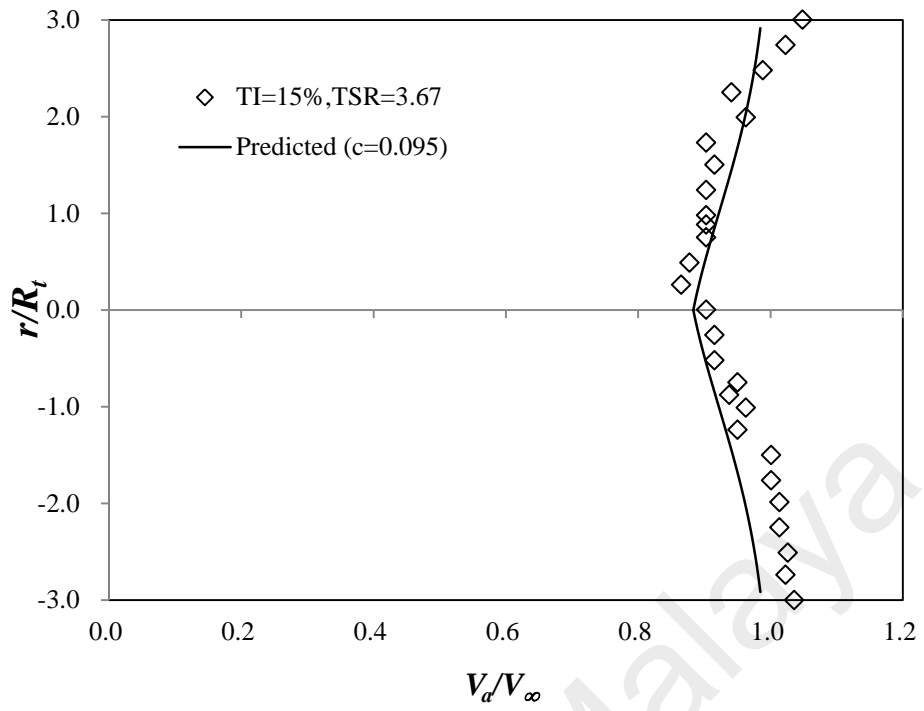
e. x/D_t =5.0
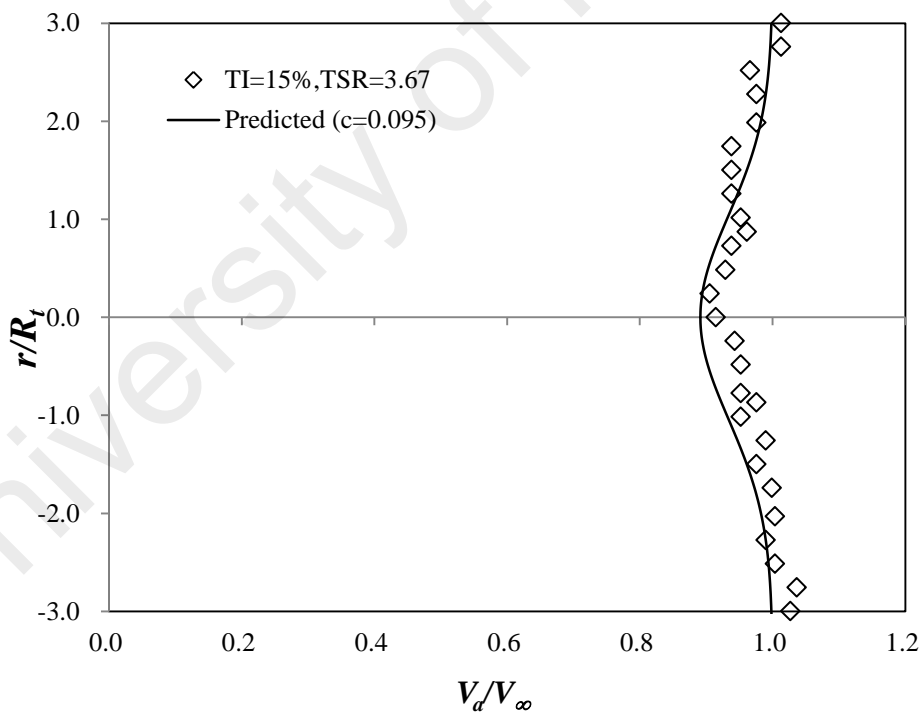
f. x/D_t =6.0

Figure 4.3, continued.
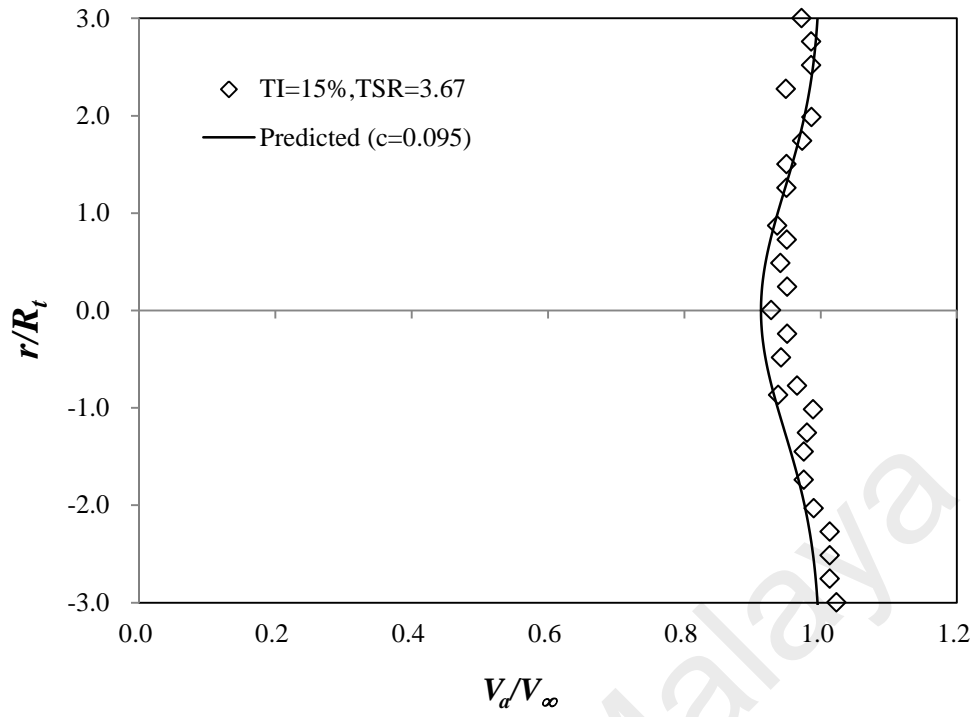
g. $x/D_t = 7.0$
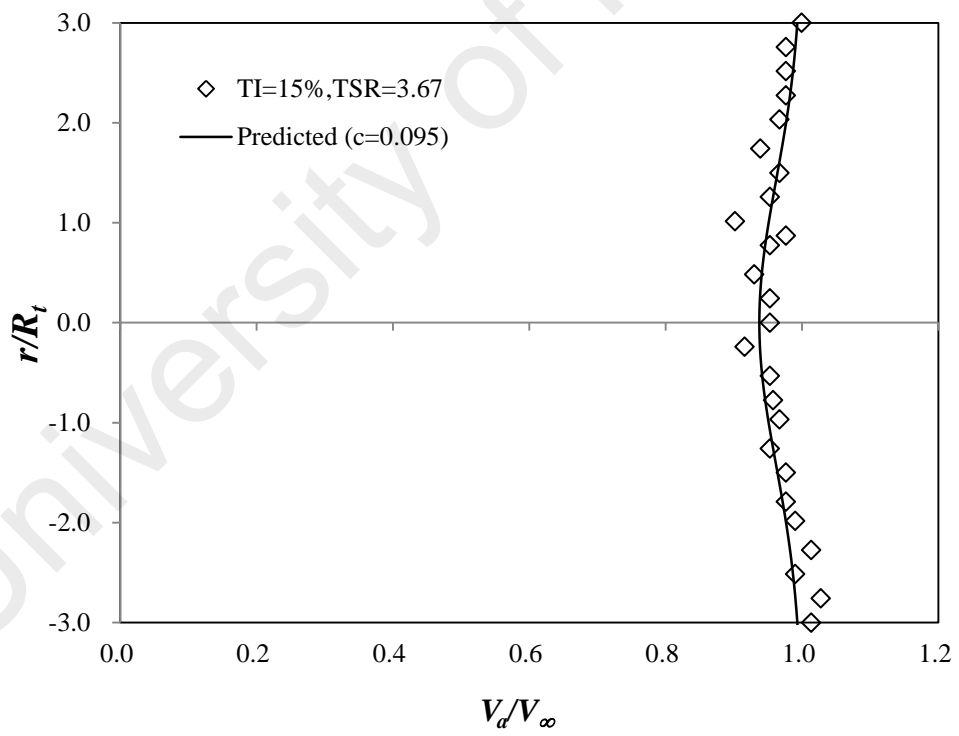
h. $x/D_t = 8.0$

Figure 4.3, continued.

4.2.4 Proposed Schematic Diagram of Turbine Wake

Hamill (1987) proposed a schematic diagram of a ship propeller jet as shown in Chapter 2 (See Figure 2.6). The preceding discussion indicated that the flow behaviour of turbine wake has similarities with ship propeller jets. The study depicts a schematic view of tidal turbine wake. The regions with a turbine wake can also be categorized into the same zones as a ship propeller jet (See Figure 4.4). The zone of flow establishment lies close to the turbine face and velocity within the zone has two-dip ridges. The presence of hub at the centre of turbine results in the wake has a high-velocity core along the axis of rotation within the zone of flow establishment. At first, the fluid is mixing with the surrounding water both inwardly and outwardly along the axis of rotation. The length of the zone of flow establishment depends on the ambient turbulence intensity. The zone of established flow is following the zone of flow establishment. In this region, the flow only mix outwardly and it has only one minimum velocity dip located at the rotational axis.
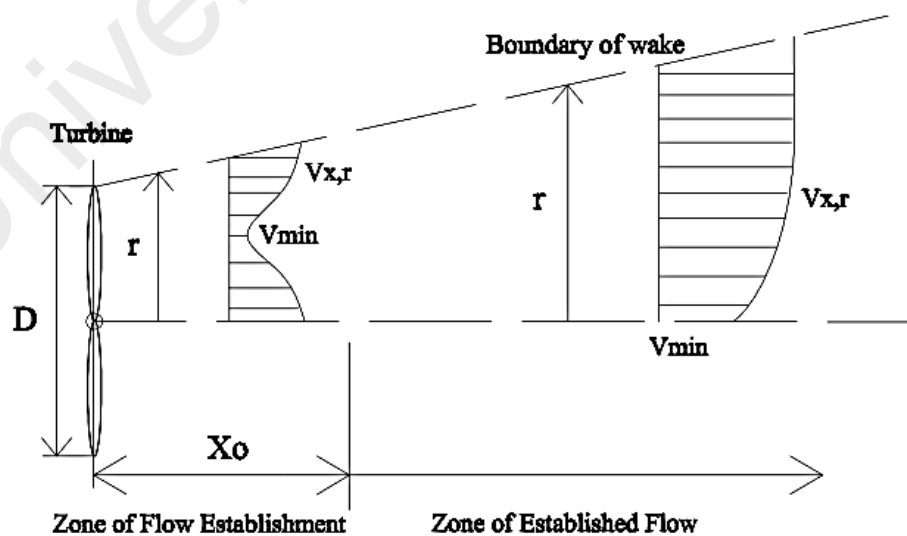
Figure 4.4: Schematic view of turbine wake (proposed)

The proposed wake model has an acceptable agreement with the experimental results at various ambient turbulence intensities. The new wake model also predicts the wake shape with appearance of two dips at near wake region. The experimental results from Maganga et al. (2010), Pinon et al. (2012) and Mycek et al. (2014) also showed the appearance of two dips in the wake. The experimental results of wake properties at high ambient turbulence level (15%) do not indicate the appearance of two dips (see Figure 4.3). The higher turbulence intensity results in the earlier merging of two dips.

The wake deficit behind turbine rotor may cause suspended sediment in the water to fall down. The concentration of suspended sediment between rotor and seabed may increase. Consequently, it may affect the bed load and the scour process around the support of TCT will be affected. The velocity deficit in the wake region also leads to the flow acceleration below the rotor. Hill et al. (2014) believed that the transition point between the scour hole and the deposited sand dune may suggest a relationship between the wake of the tidal turbine and the sand bed surface. The wake velocity at lateral sections along downstream shows its sediment transport capacity in the water column. The proposed analytical wake model may serve as an initial input for the scour prediction. The wake also affects the velocity near seabed and the flow conditions between rotor and seabed are discussed in Section 4.3.

4.2.5 Goodness-of-Fit

The above figures are providing justification for the quality of the fit provided by the given wake model. The study provides quantitative goodness-of-fit estimator R-square ($R2$). This statistic measures how successful the fit is in explaining the variation of the data. R-square is the square of the correlation between the response values and the predicted values. R-square is defined as:

$$\text{R-square} = 1 - [\text{Sum}_{(i=1 \text{ to } m)}\{w_i (y_i - f_i)^2\}] / [\text{Sum}_{(i=1 \text{ to } m)}\{w_i (y_i - y_{av})^2\}] = 1 - \text{SSE/SST} \quad (4.2)$$

Here f_i is the predicted value from the proposed model; y_{av} is the mean of the experimental data; y_i is the experimental data value; m is the number of experimental data points. w_i is the weighting applied to each data point, usually $w_i=1$ (Goodness of fit Statistics). SSE is the sum of squares due to error and SST is the total sum of squares. The authors also provide the goodness-of-fit estimator Mean Square Error (MSE).The MSE is defined as:

$$\text{MSE} = \text{SSE/m} \quad (4.3)$$

MSE value closer to 0 indicates the model is more useful for prediction. The results of the estimators are tabulated in Table 4.3. The R2 and MSE are in range of 0.1684-0.9305 (close to 1 better) and 0.0004-0.0331 (close to 0 better) respectively. The R2 are relative low at certain locations. However, the MSE are close to 0 for all the lateral sections. The results of the MSE provide justifications for the correlations proposed in the wake model. The prediction of the wake profile usually at $x/D_t>3.0$ is better than that of near wake region. The flow in the near wake region is with high shear

and turbulent. The wake pattern is rather complicated. More experimental results of near wake are required for future investigation. The proposed analytical wake model is indicated in Table 4.4.

Table 4.3: Goodness-of-fit analysis

x/D_t	I=3%		I=8%		I=15%	
	$R2$	MSE	$R2$	MSE	$R2$	MSE
1.0	N/A	N/A	0.3455	0.0331	N/A	N/A
1.2	0.3188	0.0327	N/A	N/A	0.7073	0.0111
2.0	0.3473	0.0320	0.4411	0.0290	0.7813	0.0056
3.0	0.3766	0.0289	0.5478	0.0186	0.8064	0.0006
4.0	0.8491	0.0064	N/A	N/A	0.5502	0.0021
5.0	0.9305	0.0017	0.9098	0.0023	0.6009	0.0011
6.0	0.9172	0.0024	N/A	N/A	0.2823	0.0008
7.0	0.8071	0.0042	0.7507	0.0036	0.1684	0.0006
8.0	0.7999	0.0035	N/A	N/A	0.5381	0.0004
9.0	N/A	N/A	0.6112	0.0037	N/A	N/A

*N/A: experimental results not available

Table 4.4: Analytical wake model

TI	Efflux velocity and its location	Minimum axial velocity recovery	Wake velocity distribution $V_{x,r} = V_\infty - (V_\infty - V_{min})e^A$
3%-5%		$x/D_t \leq 4$ $$\frac{V_{min}}{V_0} = 0.0106\left(\frac{x}{D_t}\right) + 1.0351$$ $x/D_t > 4$ $$\frac{V_{min}}{V_0} = 0.1123\left(\frac{x}{D_t}\right) + 0.5826$$	$1.2D_t < x \leq 3.0D_t$ $$A = [-0.5((r - R_{mo})/((\tfrac{R_{mo}}{2}) + 0.065(x - R))]^2$$ $x > 3.0D_t$ $$A = [-0.5(r/(0.065(x - R)))]^2$$
8%	$V_0 = V_\infty\sqrt{1 - C_t}$ $R_{mo} = 0.67(R_t\text{-}R_h)$	$$\frac{V_{min}}{V_0} = 0.0927\left(\frac{x}{D_t}\right) + 0.993$$	$1.0D < x \leq 3.0D_t$ $$A = [-0.5((r - R_{mo})/((\tfrac{R_{mo}}{2}) + 0.075(x - R_t)))]^2$$ $x > 3.0D_t$ $$A = [-0.5(r/(0.075(x - R_t)))]^2$$
15%		$x/D_t \leq 4$ $$\frac{V_{min}}{V_0} = 0.1505\left(\frac{x}{D_t}\right) + 0.8597$$ $x/D_t > 4$ $$\frac{V_{min}}{V_0} = 0.0372\left(\frac{x}{D_t}\right) + 1.4085$$	$x > 1.2D_t$ $$A = [-0.5(r/(0.095(x - R_t)))]^2$$

4.3 Flow Condition between Rotor and Seabed

The flow (axial, tangential and radial component) between rotor and seabed is simulated as the flow is affected by wake. The flow is also responsible for sediment transport in the vicinity of TCT. The axial velocity acts parallel to the rotor's rotational axis. The tangential velocity acts perpendicular to the turbine blade axis and is the component that represents the rotational nature of a wake. The radial velocity moves parallel to the turbine blade axis and represents the lateral expansion of the wake. The three velocity components are illustrated by the schematic diagram shown in Figure 4.5. Plots of the time-averaged axial, radial, and tangential components of velocity under the turbine blades are shown in this section.
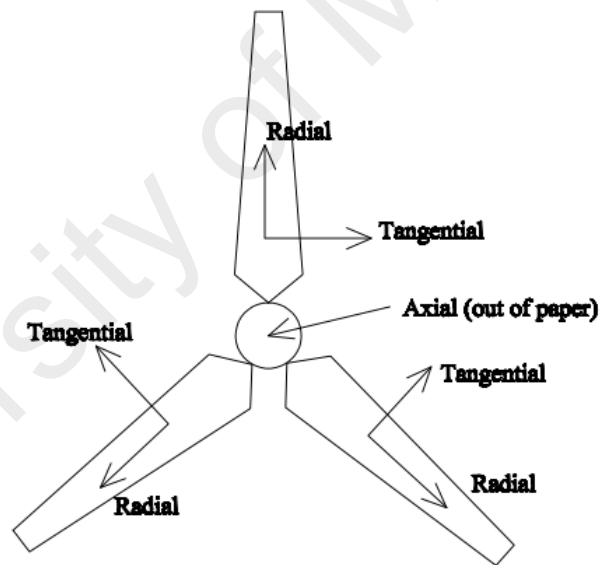
Figure 4.5: Schematic view of three velocity components

4.3.1 Influence of Rotor Tip Clearance

4.3.1.1 Axial Velocity

Ship propeller jet-induced scour has been studied for many years. Earlier researchers focused solely on the axial velocity field within the ship's propeller jets, due to the large contribution made by the axial velocity to seabed scouring. Lam et al. (2011) conducted Laser Doppler Anemometry measurement and claimed that the axial component of velocity is the main contributor to the velocity magnitude of the initial plane of a ship's propeller jet. Liu (2010) compared the downstream velocity profile of a propeller and a tidal turbine. It found that the direction of the downstream velocities of a propeller against that a turbine is opposing. This phenomenon indicates the different function of a tidal turbine and a propeller. The propeller is trying to transfer energy into the fluids which result in the acceleration of inflow. The tidal turbine aims to harness the kinetic energy from fluids and ends up slowing down the inflow.

Table 4.5 tabulates each maximum component velocity of the flow between the TCT and the seabed. It indicates that axial velocity is the biggest contributor to the velocity magnitude, in the same manner as ship's propeller jets. The maximum axial component of velocity in the investigated layers occurred in $0.5C$ ($C=0.4D_t$), $x/D_t=0.4$. The maximum value of axial velocity has approximately 1.07 times greater than the initial velocity. The maximum local acceleration of velocity around the current extraction device in the study of Sun (2008) study is approximately 1.2 times of its initial velocity. The maximum velocity locates at $x/D_t=1$ and $0.3D_t$ away from the tip of the turbine blade. The flow acceleration in Sun's work is more significant than the

current simulation. The experimental instrument applied in her study is actuator disk. It suggests that the turbine characteristic influences the extent of flow acceleration. Furthermore, Sun took the free surface effect of numerical modelling into consideration. The interaction between air and water might increase the velocity around the turbine.

Table 4.5: Maximum velocity component at each investigated layer

Height of tip clearance	Layer	Axial velocity	Radial velocity	Tangential velocity
		$(V_a/V_\infty)\%$	$(V_r/V_a)\%$	$(V_t/V_a)\%$
$1.00D_t$	$0.50C$	105.15	2.05	0.03
	$0.25C$	104.66	0.73	<0.01
	$0.05C$	100.00	0.27	<0.01
$0.80D_t$	$0.50C$	105.53	2.48	0.05
	$0.25C$	104.93	0.93	0.02
	$0.05C$	100.07	0.30	0.01
$0.60D_t$	$0.50C$	106.00	3.12	0.08
	$0.25C$	105.19	1.27	0.04
	$0.05C$	84.39	0.31	0.04
$0.40D_t$	$0.50C$	106.69	4.12	0.22
	$0.25C$	105.30	1.80	0.11
	$0.05C$	60.00	0.70	0.08

Figure 4.6 shows that the axial velocity of different layers between the TCT and the seabed under different heights of tip clearance. The axial component of velocity in the upper two investigated layers ($0.25C$ and $0.50C$ above seabed) has a moderate increase. The increment of velocity is approximately 5% of the initial incoming flow in average. The axial velocity near seabed ($0.05C$ above seabed) at each tip clearance case is lesser than the initial velocity due to the boundary layer effect. However, the fluids at each layer below and behind the turbine have slight higher axial velocity than that at the same level before turbine. This behaviour is different with the fluids passed through the rotor plane. The fluids passed through the rotor plane region experienced velocity

reduction and formed an expanding wake. The faster moving stream (below rotors) serves to re-energise the wake, breaking it up and increasing the velocity (Myers and Bahaj, 2010).

Moreover, the contraction of the TCT increases flow velocity. Based on the Bernoulli equation, the increase of velocity will be balanced by the decrease in pressure. As shown in Figure 4.7, the pressure of the fluids behind the turbine blades decreased at each investigated layer. The pressure has been non-dimensionalised by the atmospheric pressure (101.325 kPa). The difference of pressures on the two sides of turbine blades results in a suction phenomenon. The fluids at the high pressure side will be sucked to the low pressure side. This suction effect further accelerates the fluids below turbine blades on the back side. These reasons mentioned above contributed to the velocity acceleration of the fluids in each investigated layer. Figure 4.8 presents a schematic diagram to describe the flow under rotors of the TCT. A low pressure zone is formed below the boundary of the wake.
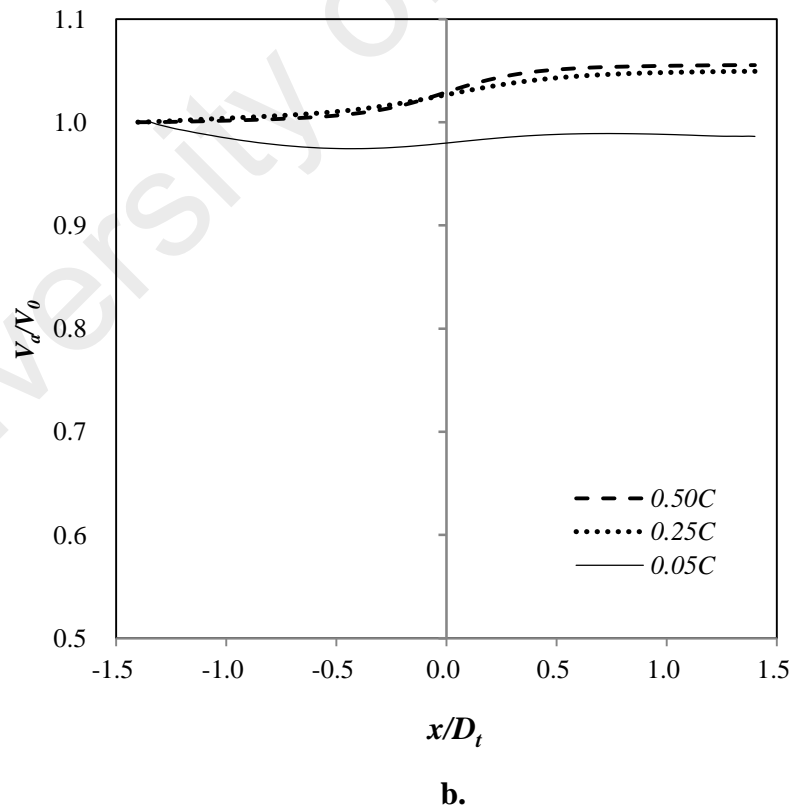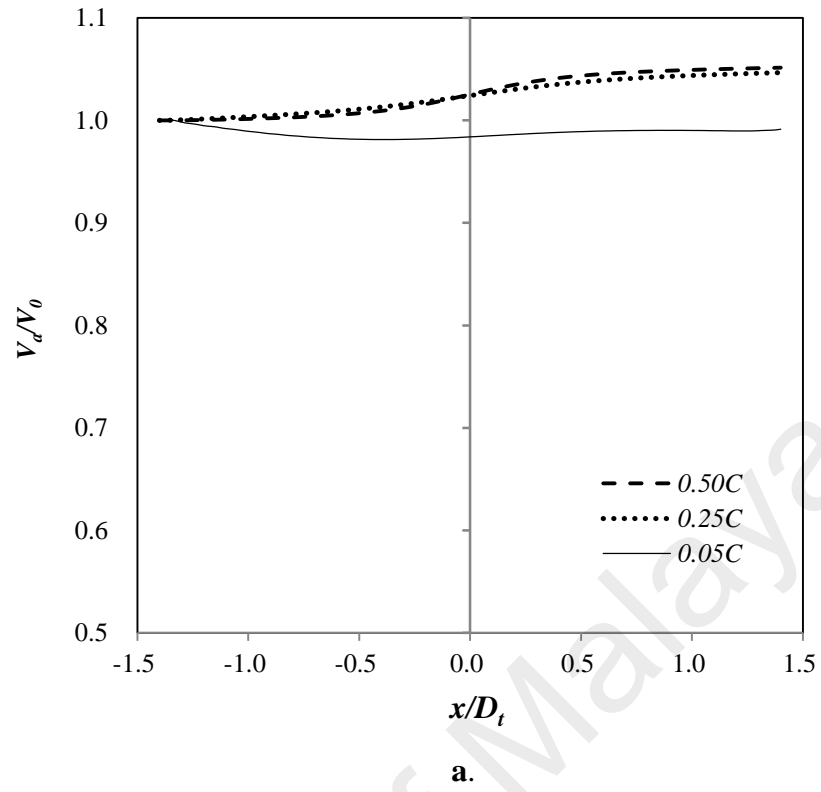
Figure 4.6: Dimensionless axial component velocity at different layers with various tip clearances from seabed: a. $1.0D_t$; b. $0.8D_t$; c. $0.6D_t$; d. $0.4D_t$.
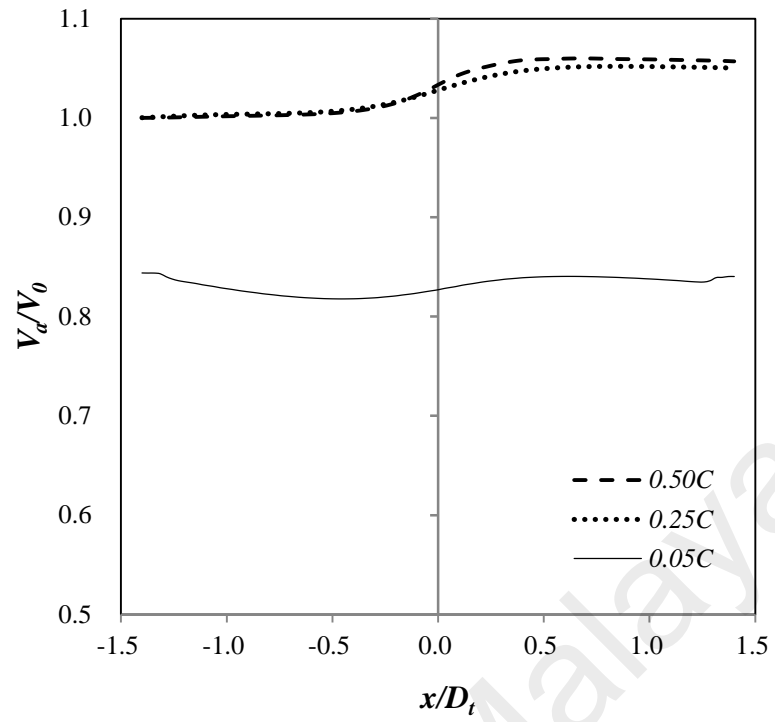
c.
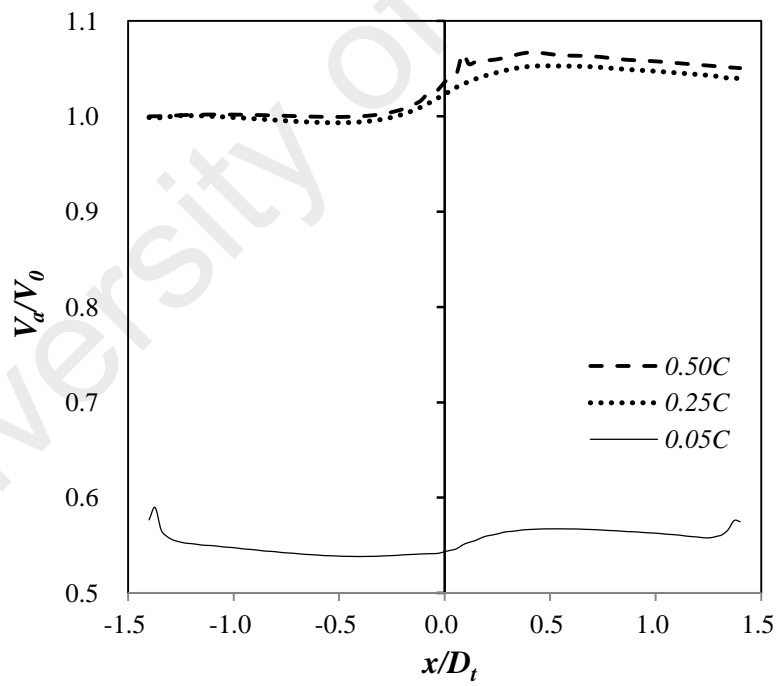
d.

Figure 4.6, continued.
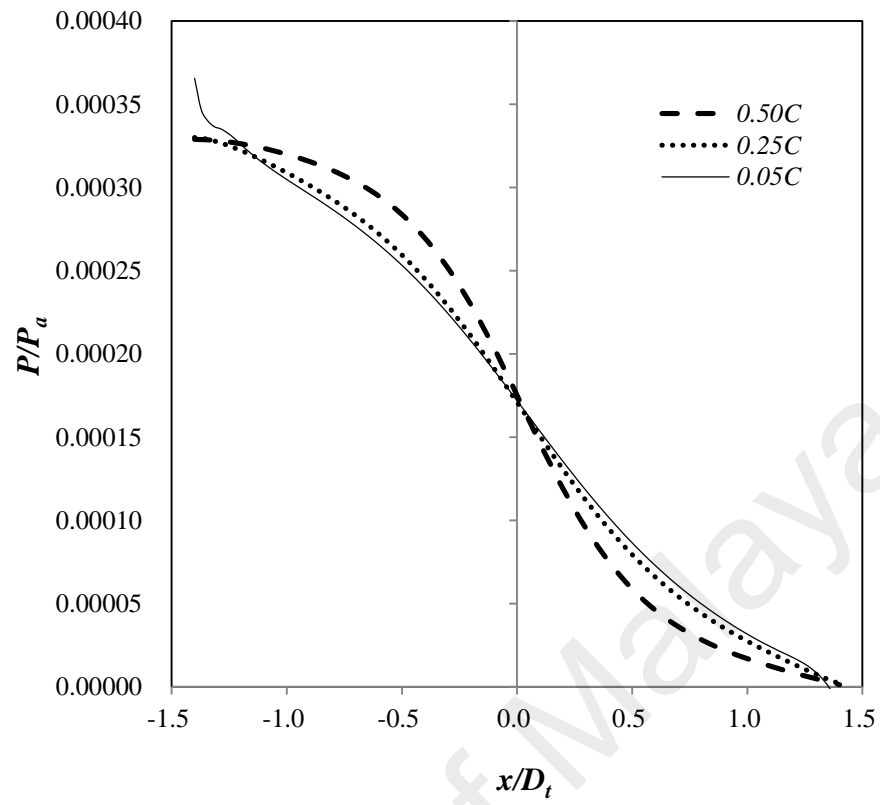
Figure 4.7: Dimensionless pressure of fluids at different layers near seabed (height of tip clearance=1.0D_t)
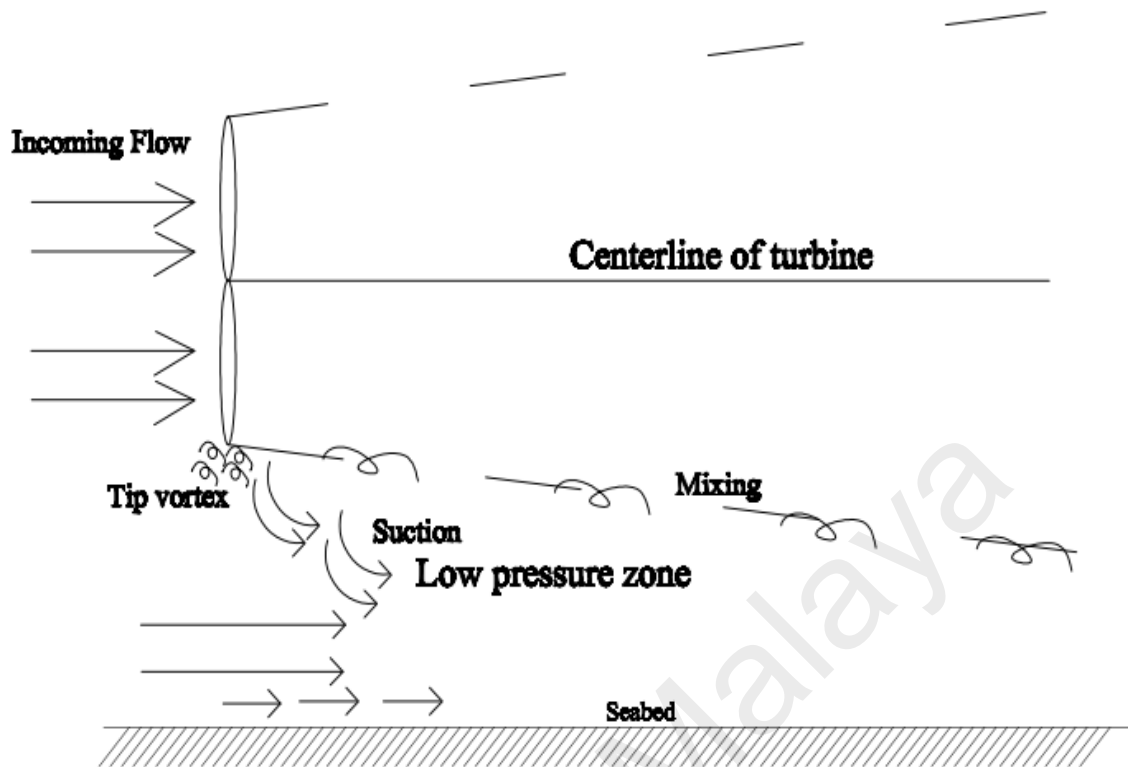
Figure 4.8 Schematic diagram of flow between the seabed and the TCT

The distribution of axial component velocity has a similar pattern despite different confinements. The influence of seabed proximity in the current study is not evident. It suggests the wake does not expand remarkably and it approaches the seabed. The fluids beneath the rotor disk are enough to re-energise the wake. Moreover, the solidity of turbine blade is low. The fluids pass through the turbine smoothly as the blockage effect is not significant. The flow suppression under the turbine is not pronounced. A turbine with high blade area ratio may have different velocity pattern when the confinement below turbine varies. The flow acceleration below the turbine blades is expected to develop along the downstream of the wake. The flow acceleration will probably affect the scour process and amplify the sediment transport at seabed.

4.3.1.2 Radial Velocity

McGarvey (1996) claimed the radial component of velocity was approximately 30% of the axial velocity along the face of the propeller. Later on, Lam et al. (2010) stated the radial component of velocity is third largest contributor to the magnitude of flow field in the propeller jet. The measurement of radial velocity is 14% of the axial velocity, which is lower than the 30% of axial velocity suggested by McGarvey (1996). Table 4.3 shows the radial component of velocity is the second largest contributor which is different with ship propeller jet. The maximum radial velocity component is approximately 4.12% of the maximum axial velocity component. It is the second largest contributor of velocity, which is in a different manner as ship propeller jets.

The radial velocity moves parallel to the turbine blade axis and represents the lateral expansion of fluids. The fluids diffused downward once they approached the blades due to the blockage effect of turbine blades. The distributions of radial velocity at each layer are symmetric which are in valley shapes. The peak ridged radial velocity occurs either at or near the Z-axis (See Figure 4.9). Table 4.6 tabulates the maximum radial velocity at each investigated layer. The maximum radial velocity located at the $0.5C$ ($C=0.4D_t$), $x/D_t=0$ (Z-axis), which is 4.4% of the initial velocity. The trend of each component velocity close to the tip of turbine blade might be more complicated due to tip vortex. The radial velocity of the fluids in the investigated layer decreased right after the turbine blades. The radial component velocity is relatively less and may not have pronounced effects on local scour. The radial component of velocity might contribute to the backfilling of scour hole.

Table 4.6: Maximum radial component of velocity

Height of tip clearance	Layer	Position (x/D_t)	Radial velocity $(V_r/V_o)\%$
1.00D_t	0.50C	0.00	2.16
	0.25C	0.04	0.76
	0.05C	-1.37	0.27
0.80D_t	0.50C	0.00	2.62
	0.25C	0.02	0.98
	0.05C	-1.34	0.30
0.60D_t	0.50C	0.00	3.31
	0.25C	0.00	1.34
	0.05C	-1.37	0.26
0.40D_t	0.50C	0.00	4.40
	0.25C	0.03	1.90
	0.05C	1.40	0.42
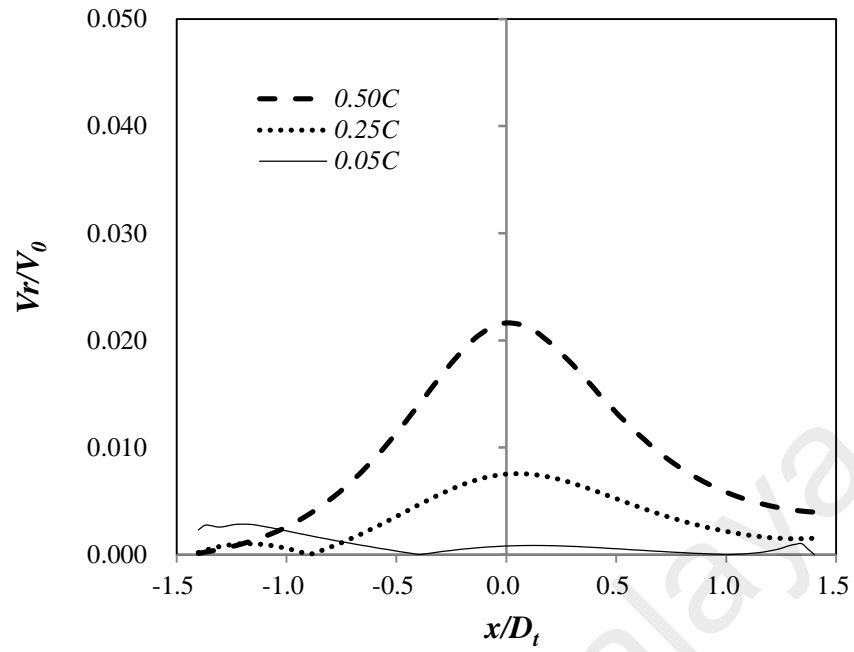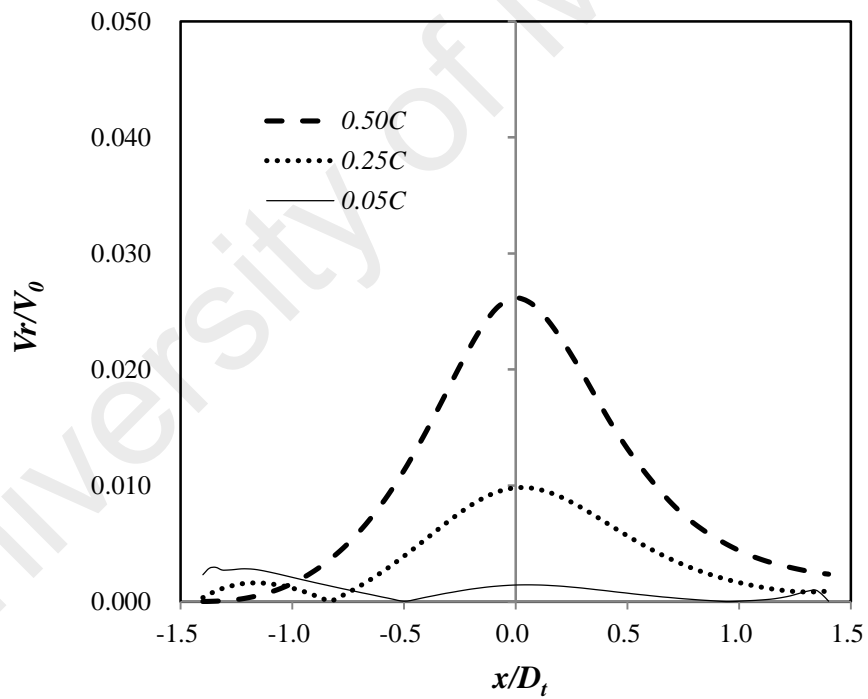
Figure 4.9: Dimensionless radial component velocity at different layers with various heights of tip clearances from seabed: a. $1.0D_t$; b. $0.8D_t$; c. $0.6D_t$; d. $0.4D_t$.

c.

c.

100

c.

d.
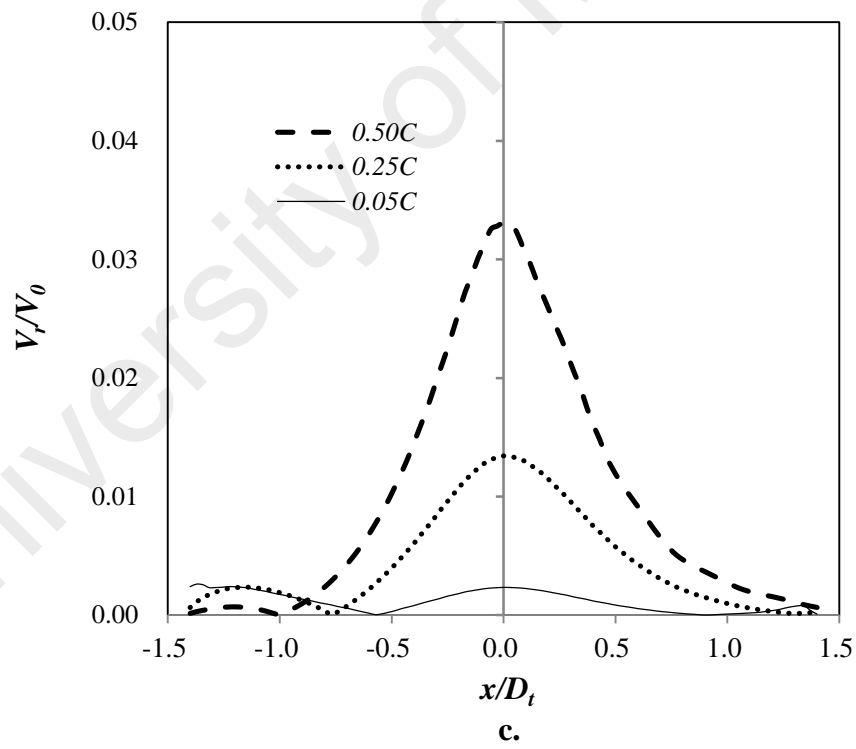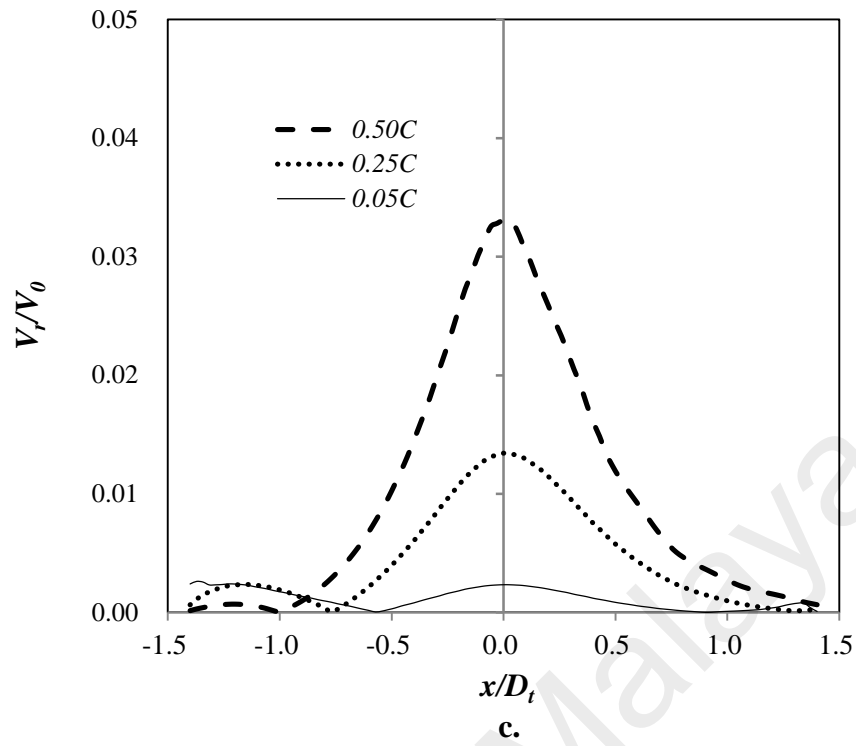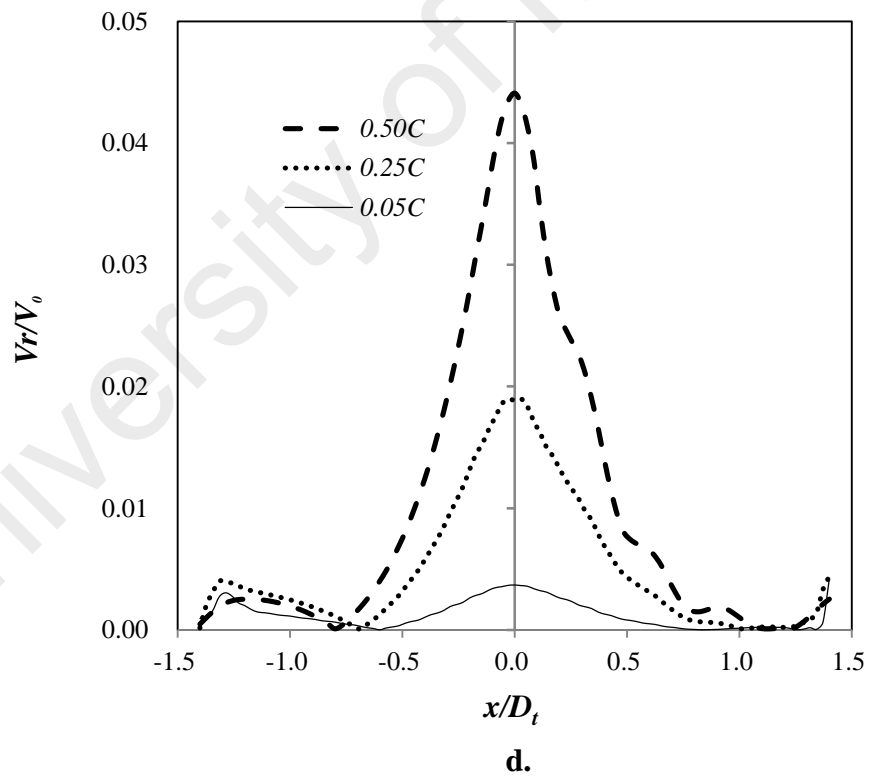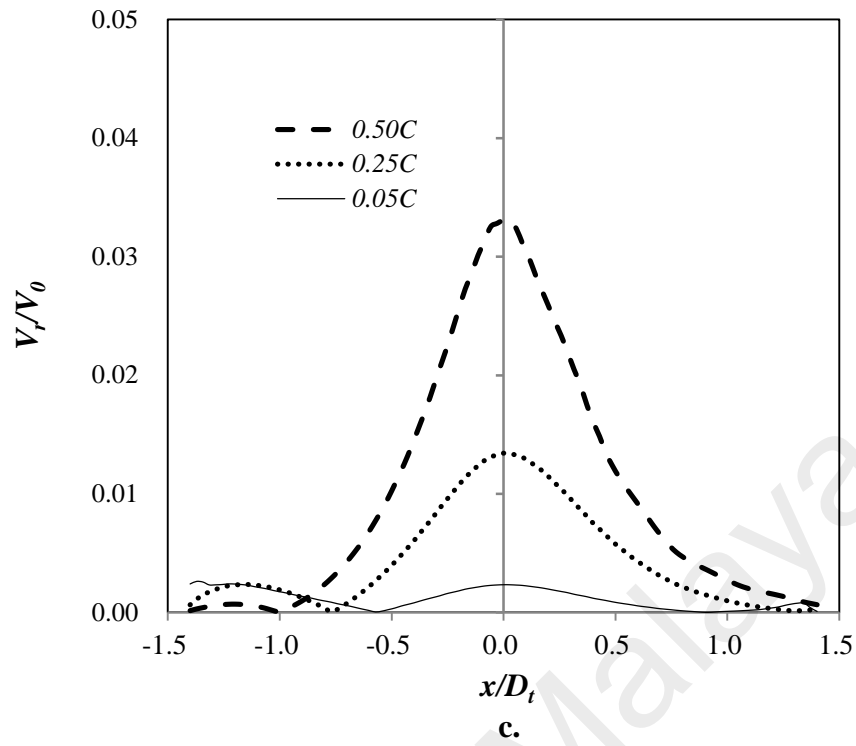
Figure 4.9, continued.

4.3.1.3 Tangential Velocity

Many researches approved that the tangential component of velocity is the second largest contributor to the resultant field in the ship's propeller jet. Prosser (1986) estimated the magnitude of maximum tangential velocity is approximately 30% of the maximum axial velocity. The results have been contradicted by Lam et al. (2010), they reported that the maximum tangential component of velocity within a ship propeller jet is 82% of the maximum axial velocity. The tangential velocity acts perpendicular to the turbine blade rotating axis. The tangential component results from the rotating nature of turbine blades and it contributes to the rotation of fluids. The fluids below and behind the turbine should not have significant tangential component as the fluids are away from the blades.

Figure 4.10 shows the distribution of tangential velocity. The distribution of tangential velocity is more complicated compared to the radial velocity. The distribution of tangential velocity varies with height of tip clearance and it is remarkably small. However, Figure 4.10d is more predictable and shows seasonal rise and falls of tangential velocity at the layer $0.5C$ when tip clearance is $0.4D_t$. This might be the cyclic decay of tangential component. Table 4.7 shows the maximum tangential velocity at each investigated layer. The highest tangential velocity occurred at x/D_t=0.09 (C=0.4D_t), which is 0.24% of initial incoming flow. It shows the rotational of fluids is higher in the region near turbine blade.

Table 4.7 Maximum tangential component of velocity

Height of tip clearance	Layer	Position	Tangential velocity
		(x/D_t)	(V_t/V_0)%
$1.00D_t$	$0.50C$	0.20	0.03
	$0.25C$	0.26	<0.01
	$0.05C$	0.26	<0.01
$0.80D_t$	$0.50C$	0.17	0.05
	$0.25C$	0.23	0.02
	$0.05C$	0.23	0.01
$0.60D_t$	$0.50C$	0.11	0.09
	$0.25C$	0.20	0.04
	$0.05C$	0.20	0.03
$0.40D_t$	$0.50C$	0.09	0.24
	$0.25C$	0.11	0.12
	$0.05C$	0.17	0.05
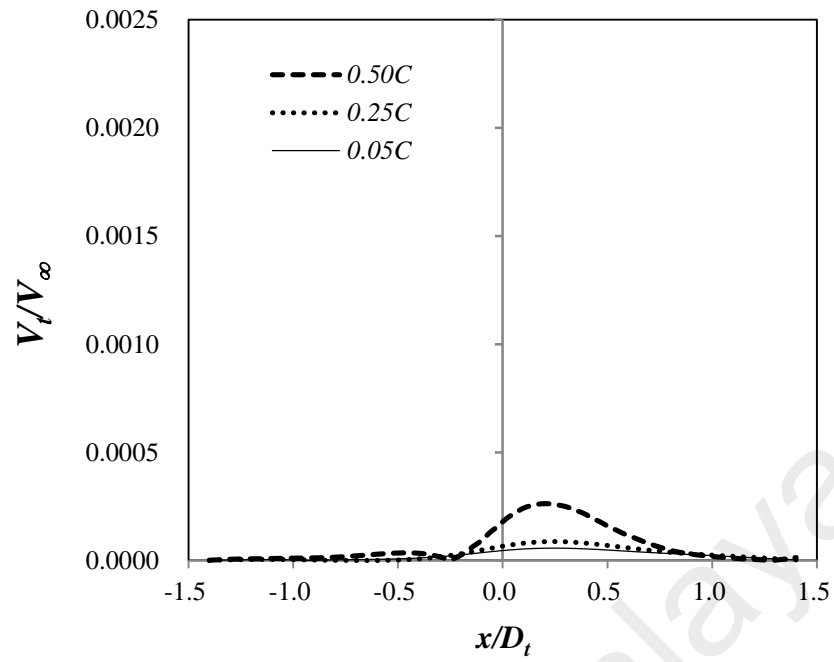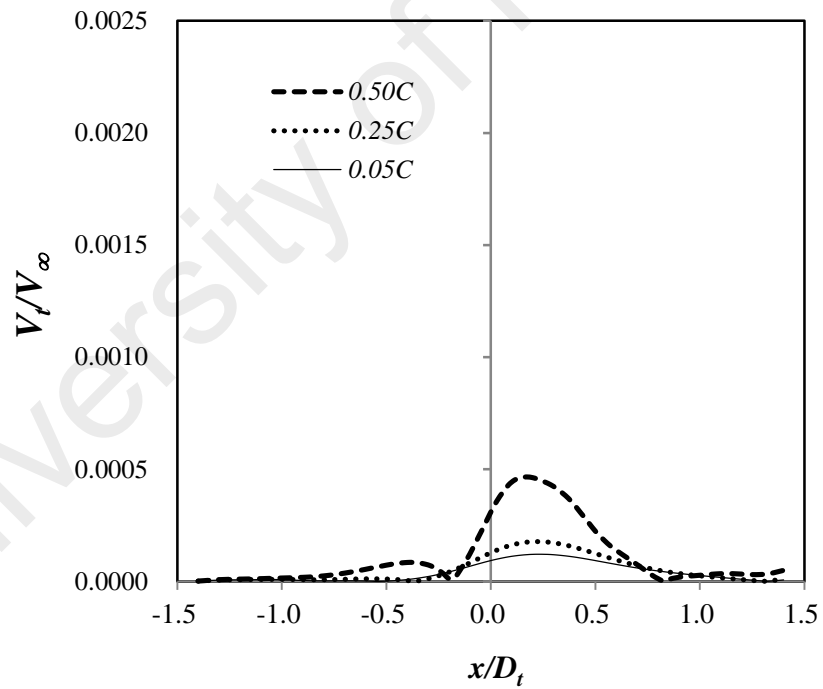
Figure 4.10: Dimensionless tangential velocities at various tip clearances: a. 1.0D_t; b. 0.8D_t; c. 0.6D_t; d. 0.4D_t.

c.

d.
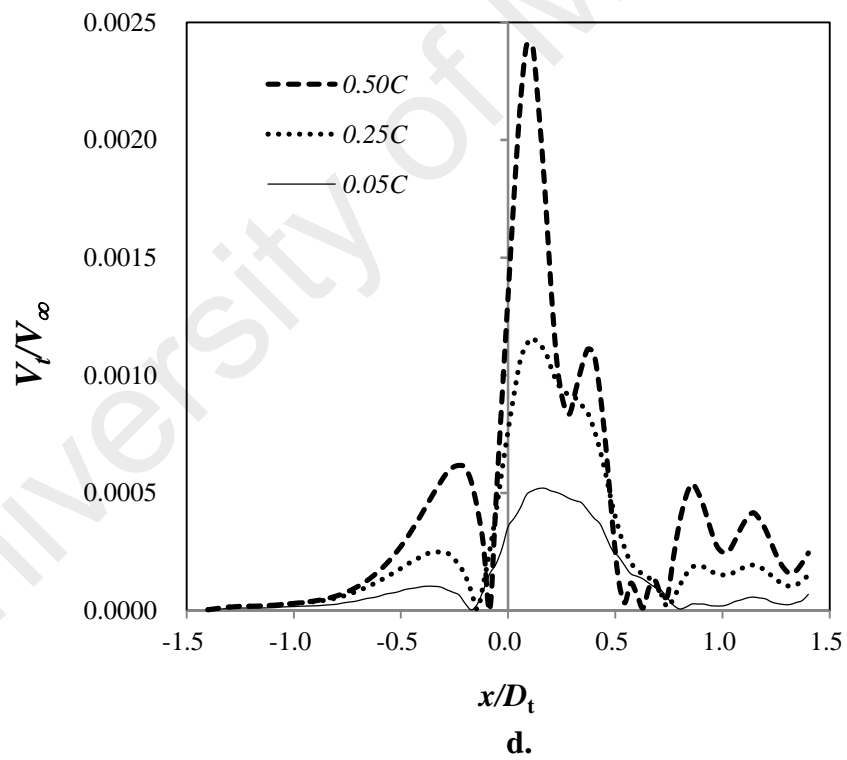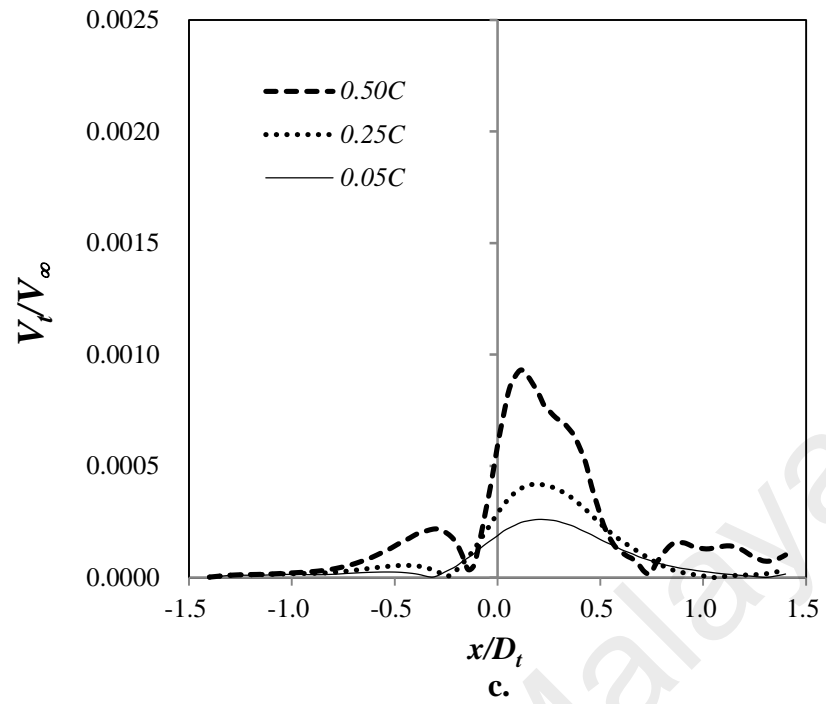
Figure 4.10, continued.

4.3.2.1 Axial Velocity

Liu (2010) presented a study and showed that the number of blades has a significant importance for the efficiency of turbine performance. This section presents the effect of the number of blades on the flow between the TCT and the seabed. Table 4.8 tabulates the maximum velocity component at each investigated layer. The axial velocity is the dominant component of fluids under the turbine blades in all computational cases. The radial component of velocity is the second largest contributor to the magnitude of velocity instead of the tangential component.

Table 4.8: Maximum velocity component at each investigated layer

Number of Blades	Layer	Axial velocity $(V_a/V_\infty)\%$	Radial velocity $(V_r/V_a)\%$	Tangential velocity $(V_t/V_a)\%$
2-blade	0.05C	100.07	0.29	<0.010
	0.50C	103.63	1.35	0.019
3-blade	0.05C	100.08	0.28	<0.010
	0.50C	105.14	2.16	0.026
4-blade	0.05C	100.90	0.30	<0.010
	0.50C	106.88	3.07	0.011
5-blade	0.05C	103.25	0.27	<0.010
	0.50C	109.12	4.18	0.014

Figure 4.11 shows the axial velocity of the flow near the seabed. The fluids at each layer below and behind the turbine have a higher axial velocity than that at the same level before the turbine. The fluids behind the turbine in the two layers did experience acceleration, particularly in the layer of 0.5Dt. The two-blade turbine has the least flow change, which is approximately 3.6% acceleration. The maximum acceleration is approximately 9% from the five-bladed turbine (see Figure 4.11b). The fluids near the

seabed ($0.05D_t$) have less acceleration than the other layers. The lower change of axial velocity at that layer is due to the viscous effect of the seabed. The five-bladed turbine also causes the largest acceleration in the region near the seabed. The blade area ratio is a key parameter of the flow under the rotors. A turbine with a higher solidity results in greater velocity reduction right behind the rotors. The water around the rotors will move faster to recover the velocity deficit in the cone-shaped wake region.
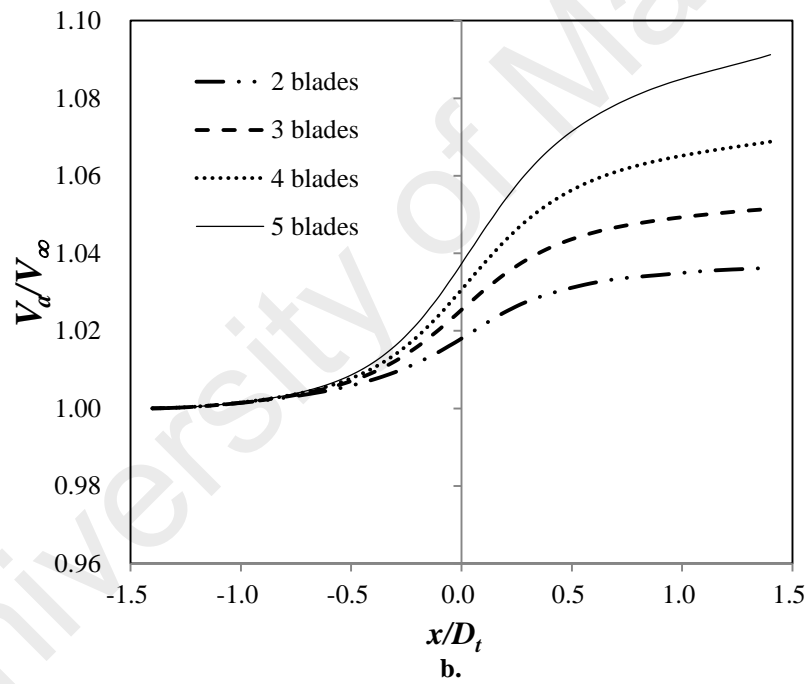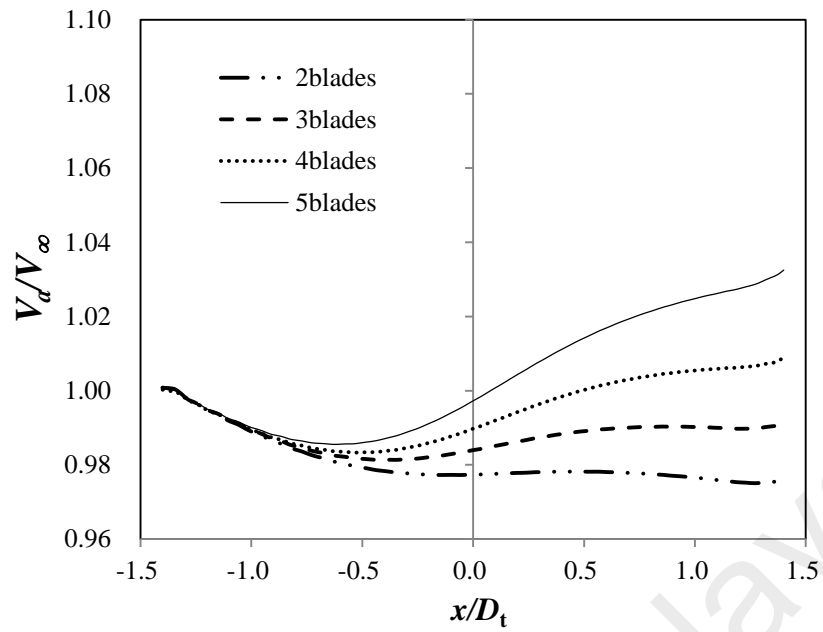
Figure 4.11: Dimensionless axial component velocity at different layers: a. 0.05*C*; b. 0.50*C*.

Figure 4.12 shows the contour plot of axial velocity around the turbines. The behaviour of flow acceleration for the fluids around the turbine blades differs from the fluids passing through the rotor plane. The flow outside the wake region will re-energise the wake. It was observed that the fluids outside the wake region in Figure 4.12 tend to have a higher velocity than the free stream. The acceleration around the turbine blades in the current study is in line with Sun (2008) and Hill et al. (2014). This further suggests that the turbine characteristics influence the extent of flow acceleration. Therefore, the geometry of TCT may also affect the scour process.
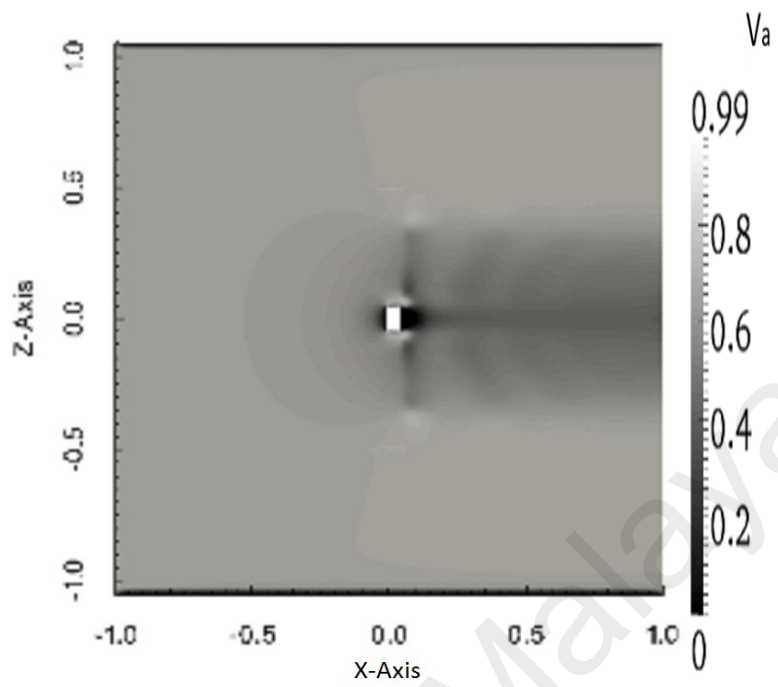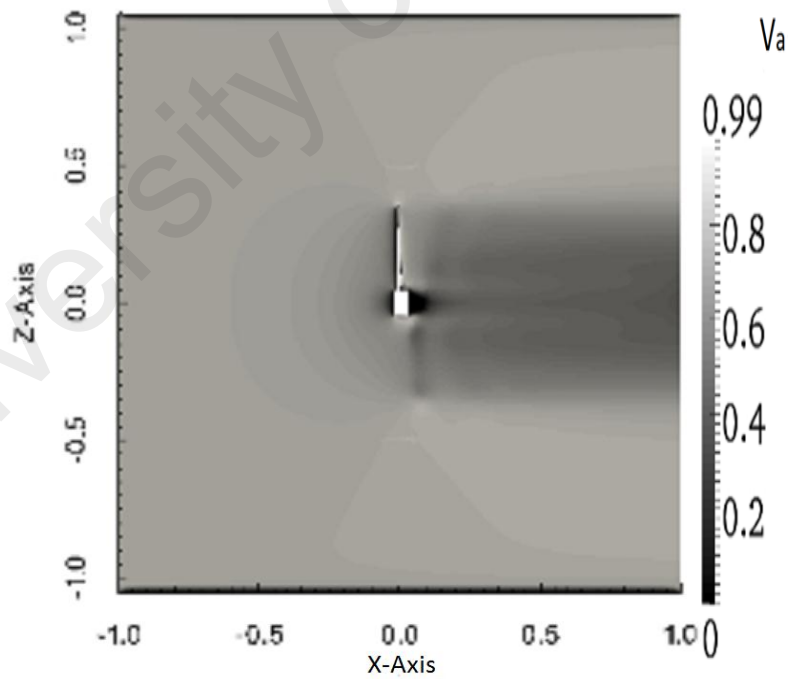
a. 2-blade

b. 3-blade

Figure 4.12: Axial velocity contour of turbine with different blade number:
a.2-blade; b. 3-blade; c. 4-blade; d. 5-blade.
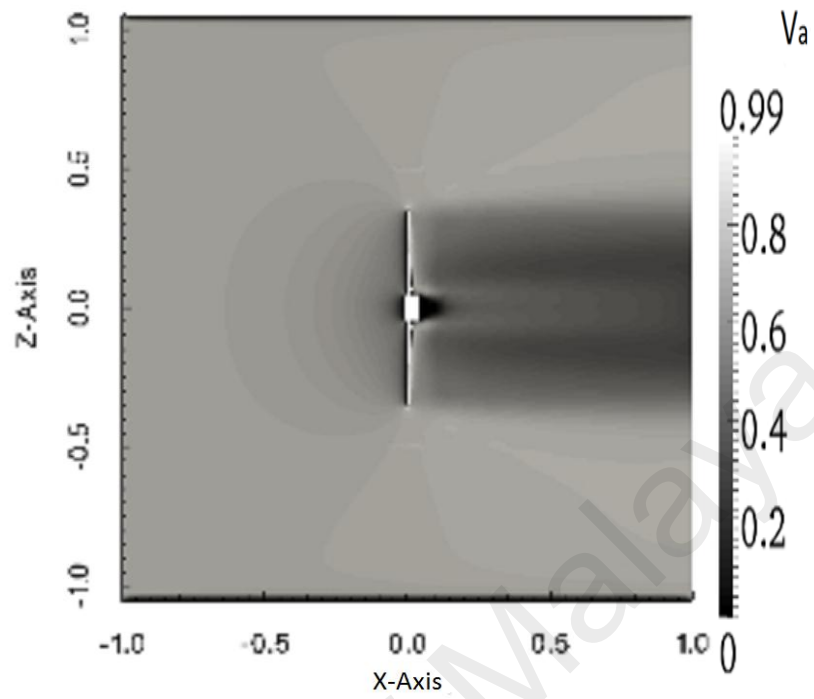
c. 4-blade
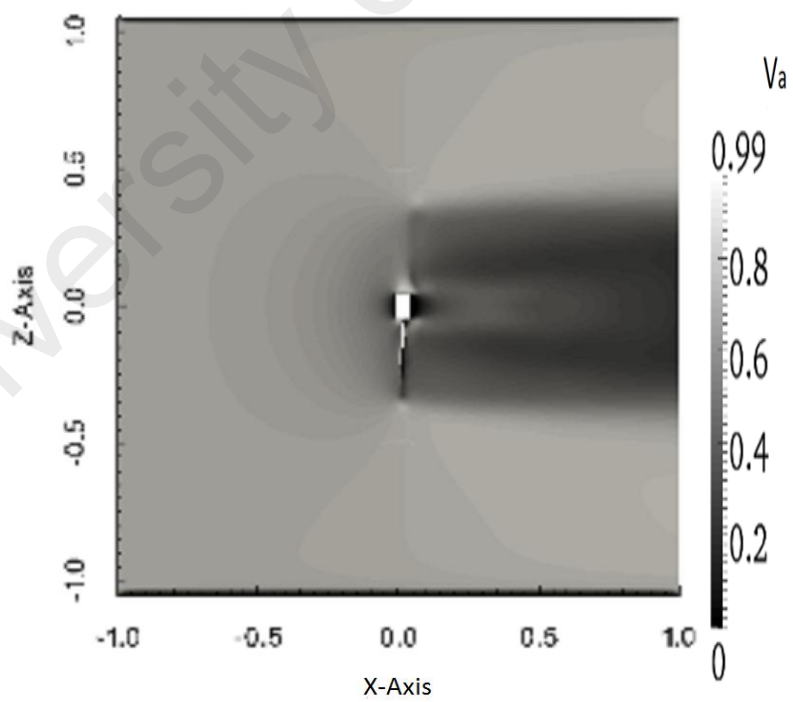
d. 5-blade

Figure 4.12, continued.

4.3.2.2 Radial velocity

The increase of blade numbers does not change the velocity components of ships' propeller jets. The radial component of velocity of the flow below ($0.05C$ and $0.50C$ from seabed) the turbine blades is the second largest contributor to the magnitude of velocity instead of the tangential component. Figure 4.13 illustrates the radial component of the flow field between the TST and the seabed. The distribution of radial velocity at the $0.50C$ layer is relatively predictable. The distributions of radial velocity at the $0.50C$ layer are axisymmetric. The highest radial velocity component is approximately $0.042V_\infty$ and occurs near the Z-axis when the turbine has 5 blades. The fluids near the seabed ($0.05C$) have minor radial component. However, the flow near the seabed shows the same trend as the water flows in the $0.50C$ layer. The greater number of blades results in a higher radial velocity of fluids. The radial velocity starts to decrease at the back of the turbine in all computational cases. Table 4.7 also shows that the number of blades has a significant effect on the maximum radial velocity below the turbine blades. The radial velocity under the five-bladed turbine is approximately two times the radial velocity below the two-bladed turbine.
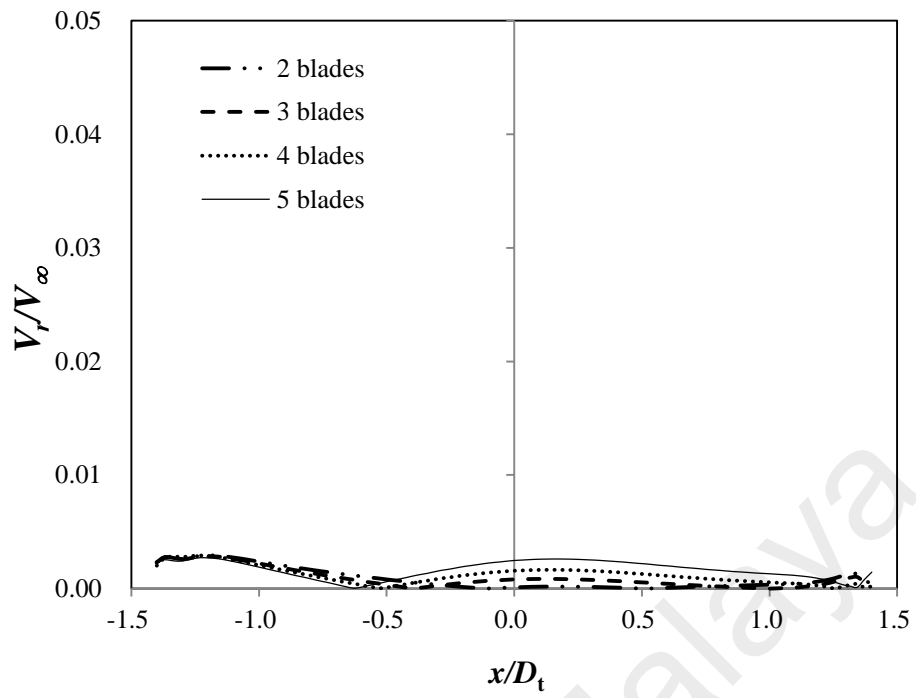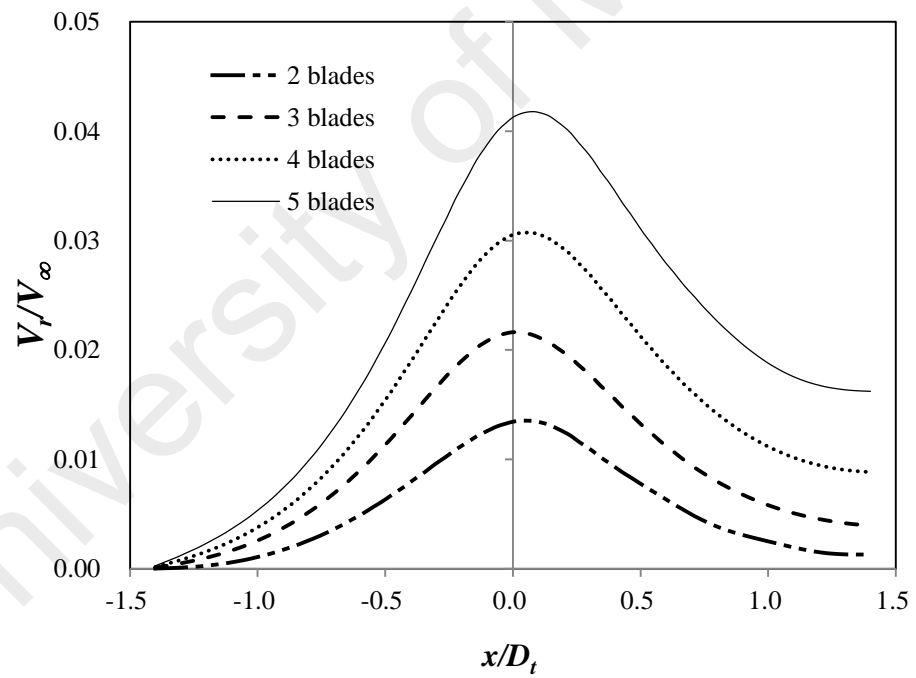
Figure 4.13: Dimensionless radial component velocity at different layers: a. 0.05*C*; b. 0.50*C*.

The fluids are diffused downward once they approached the blades as radial velocity represents the lateral expansion of fluids. More fluids will be diffused away if the turbine has a higher blade area ratio. Figure 4.14 presents a contour plot of radial velocity around the turbines. It demonstrates that more radial components exist in the region closer to the turbine blades. It further demonstrates that a higher blade area ratio could cause higher radial velocity in fluids at the downstream (see Fig. 4.14d). Higher radial velocity was also observed near turbine tip compares to other regions. It is in line with the study of Chamorro et al. (2013). They also observed higher radial velocity near the turbine tip. Figure 4.14 shows that the fluids below the rotational axis have negative radial velocity. It indicates that as the fluids below the rotational axis approach the turbine blades while the fluids diffuse downward. The radial velocity may cause the sediment diffuse downward as well.
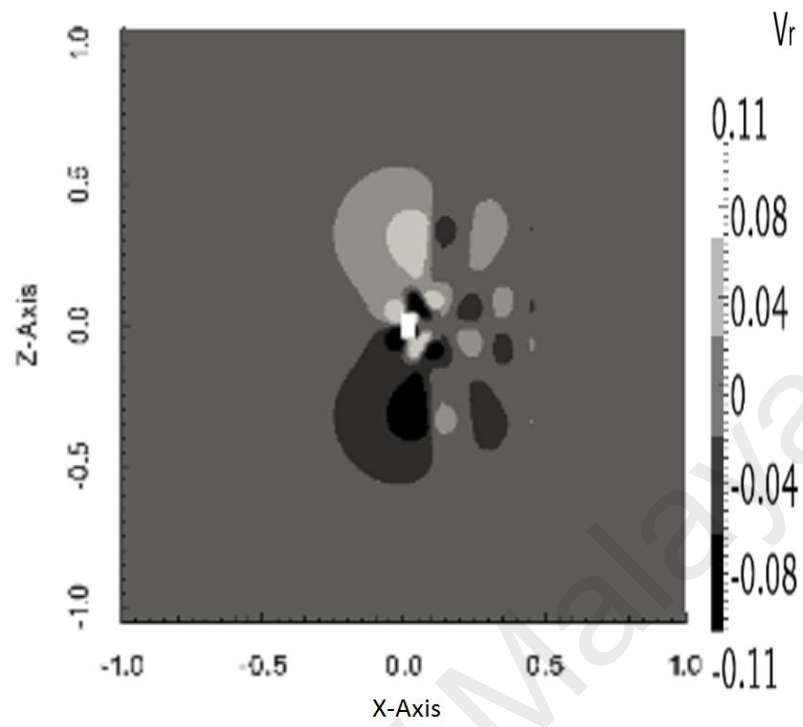
a. 2-blade
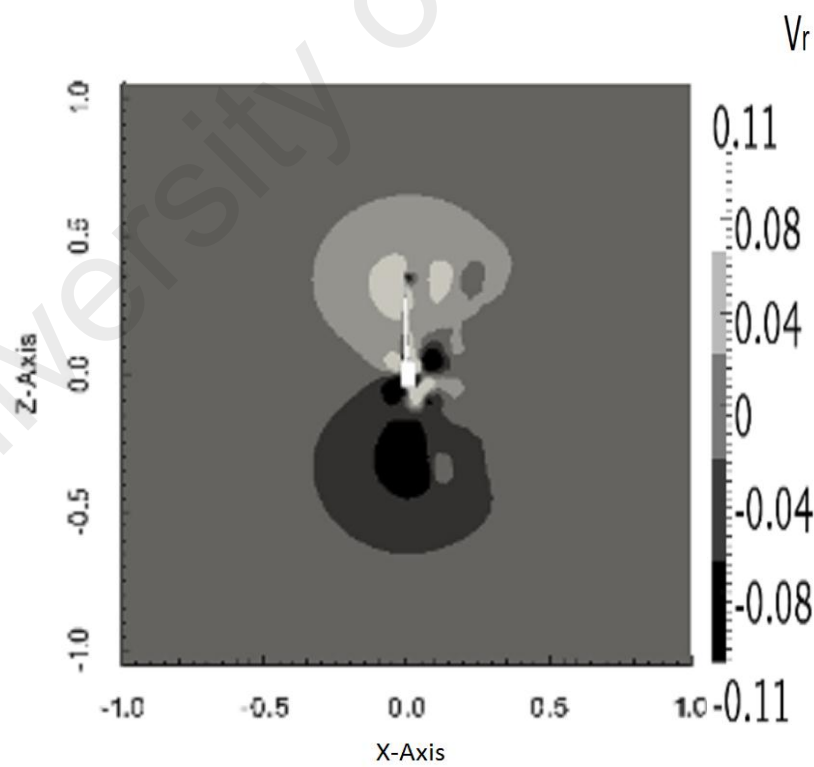
b. 3-blade

Figure 4.14: Radial velocity contour of turbine with different blade numbers: a. 2-blade; b. 3-blade; c. 4-blade d. 5-blade.
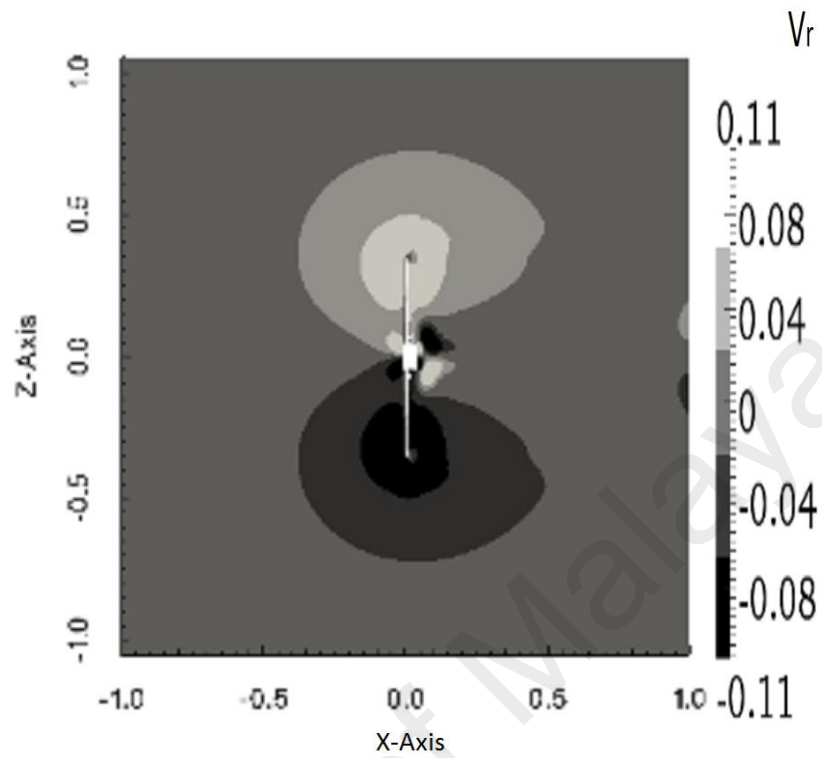
c. 4-blade
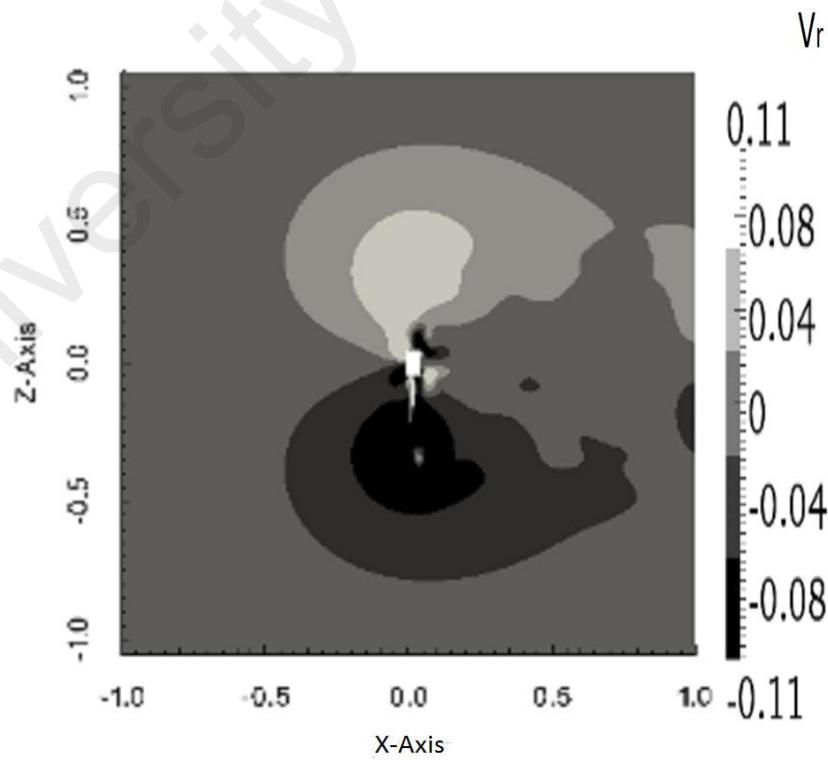
d. 5-blade

Figure 4.14, continued.

4.3.2.3 Tangential velocity

The tangential velocity acts perpendicular to the rotating axis of the turbine blade. The tangential component results from the rotating nature of the turbine blades and it contributes to the rotation of fluids. The tangential component is the second largest contributor to the velocity magnitude of the jets produced by a three-bladed and a six-bladed propeller (Lam et al., 2012b). However, the flow field under the turbine blades has a small tangential component. Figure 4.15 shows the tangential velocity around the turbines (2, 3, 4 and 5 blades).
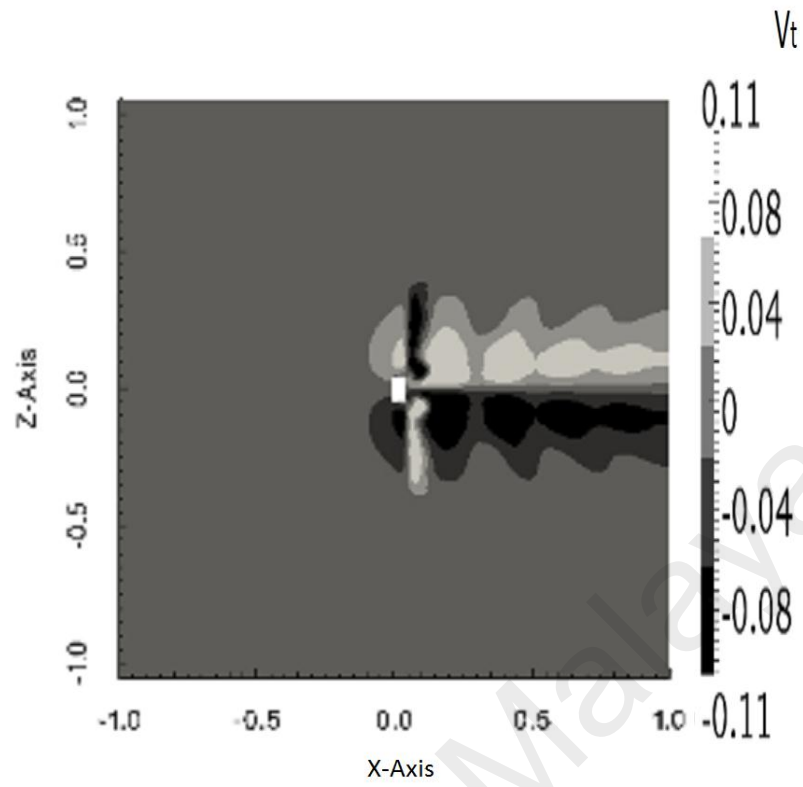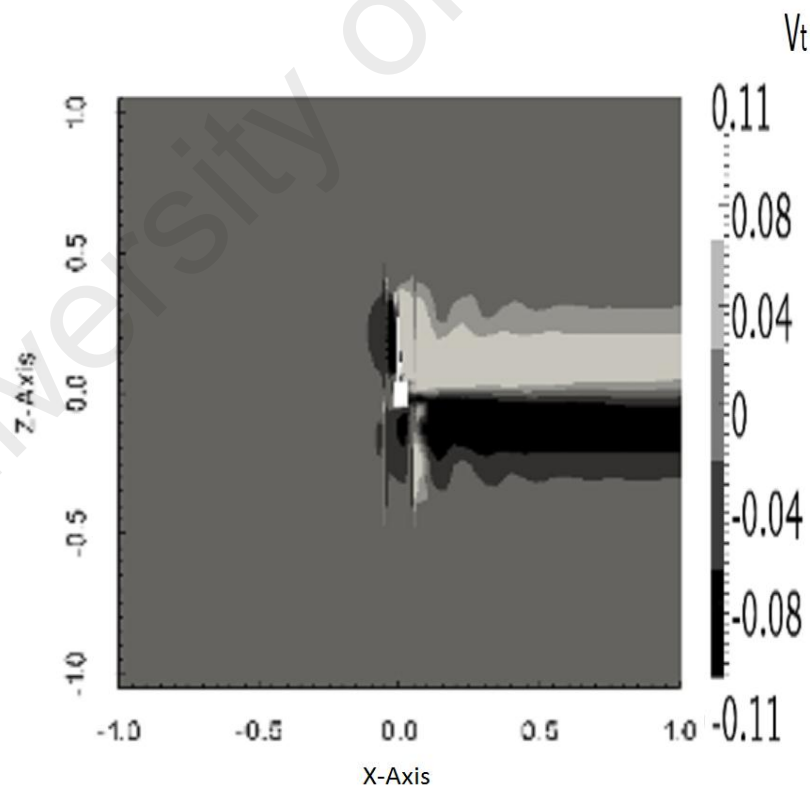
a. 2-blade

b. 3-blade

Figure 4.15: Tangential velocity contour of turbine with different blade numbers: a. 2-blade; b. 3-blade; c. 4-blade; d. 5-blade.

c. 4-blade

d. 5-blade
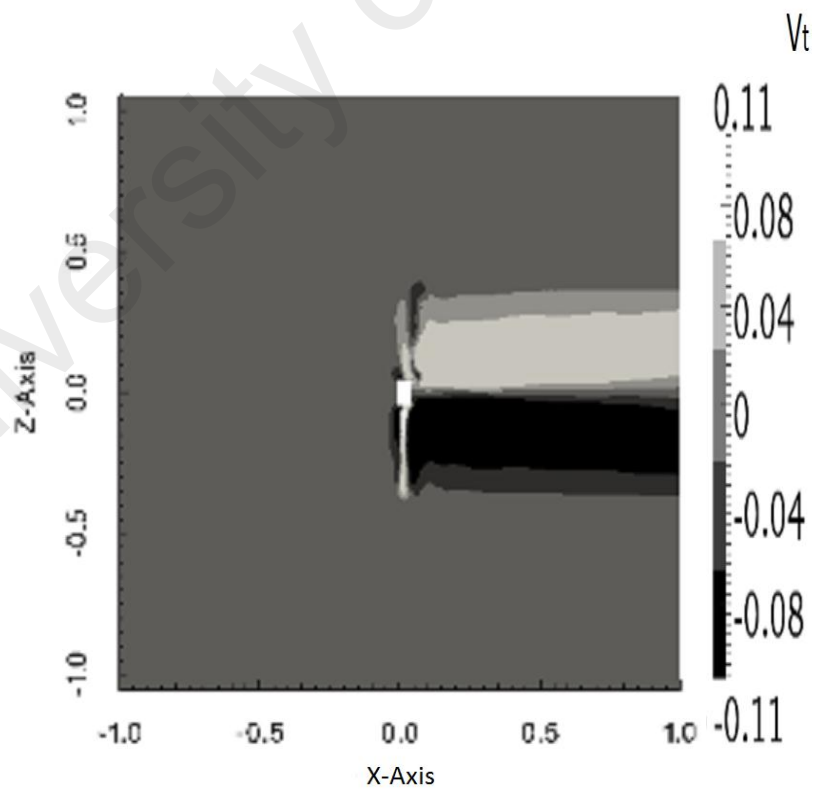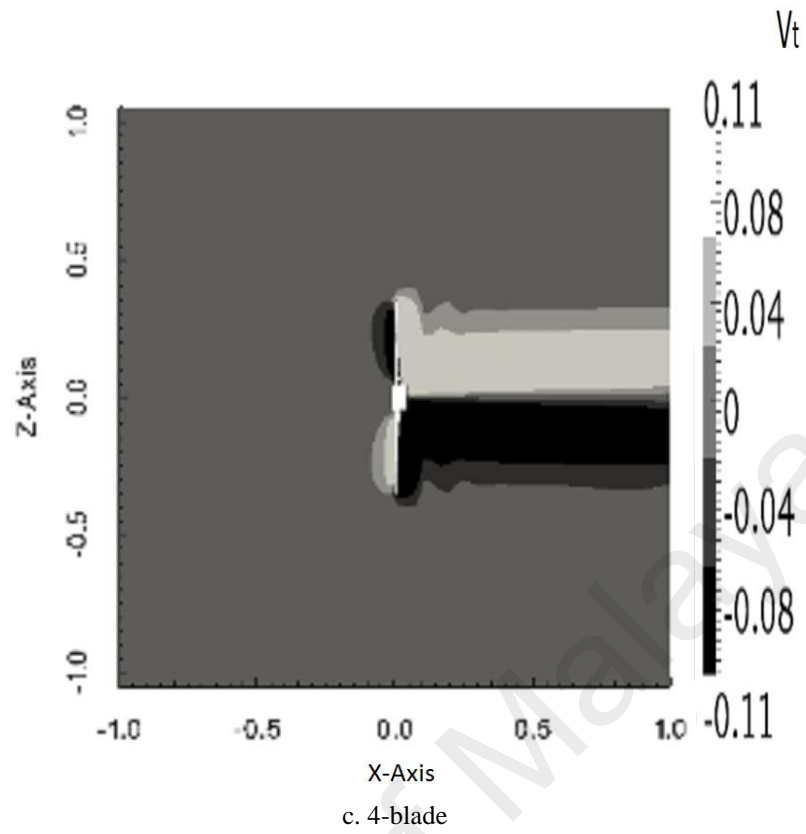
Figure 4.15, continued.

A ship's propeller imposes rotational force to produce the swirling velocity field. A high tangential velocity component is expected in the flow field of ship propeller jets. However, a TCT extracts energy through the rotation. The induced tangential velocity in the flow field generated by the turbine can reasonably be less compared to the jet produced by a ship propeller. The tangential component of velocity is even less significant under the turbine blades. The tangential velocity below rotor may not affect the scour process around the support of TCT. The tangential component is pronounced in the wake. It is identical with the study of Chamorro et al. (2013), which they detected a high tangential velocity near the wake core. It may contribute to the interaction between the suspended particles and wake.

4.3.3 Development of Boundary Layer

The mechanism of horseshoe vortex is of significant importance in the process of scour. The rotation of the incoming flow results in the horseshoe vortex. The boundary layer experiences a three-dimensional separation under the influence of the adverse pressure gradient induced by the presence of the support structure. The separated boundary layer accordingly rolls up to from a spiral vortex around the support structure (Sumer and Fredsøe, 2002).

The incoming boundary layer and pressure gradient induced by the support structure are the two necessary preconditions to generate a horseshoe vortex. Baker (1979a; 1979b) claimed that the non-dimensional quantities describing the horseshoe vortex in the case of steady current mainly depends on the following parameters:

$$\frac{\delta}{D}, \ R_{e_D} (\text{or alternatively} \ R_{e_\delta}), \text{and pile geometry}$$

in which $\delta/D=$ the ratio of bed boundary layer thickness to the pile diameter, $R_{e_D}=$ the

pile Reynolds number (Equation (4.4)):

$$R_{e_D} = \frac{UD_p}{v} \tag{4.4}$$

and R_{e_δ} = the bed-boundary-layer Reynolds number (Equation (4.5)):

$$R_{e_\delta} = \frac{U\delta}{v} \tag{4.5}$$

where U is the velocity at the edge of the bed boundary layer, v is the kinetic viscosity.

Figure 4.16 shows the current boundary layer profile with rotor in operation in

conjunction with measured data from Chilworth flume, University of Southampton

(Myers et al., 2008). The measured boundary layer profiles are without presence of

energy extraction devices. The seabed condition incorporated in the current numerical

simulation is without roughness. The numerical results indicate that the flow near

seabed is increasing and the velocity gradient is reduced compared with the

experimental data without rotor in operation. The flow acceleration increases the shear

stress on seabed and causes more sediment to transport. The five-bladed turbine results

in highest acceleration. The difference of the flow acceleration under different turbines

is not significant. Minor difference of velocity near seabed in long term could cause

evident differences on the capacity of sediment transport. More logarithmic velocity

distribution exists in real marine environment. The presence of rotor significantly

interferes with the boundary layer. The changes of flow near seabed possibly affect the

bed load and suspended load of sediment. The increase of number of blades results in

greater acceleration of flow under the TCT. The turbine with higher blade area ratio

may need higher shaft height to avoid severe triggering of sediment transport.
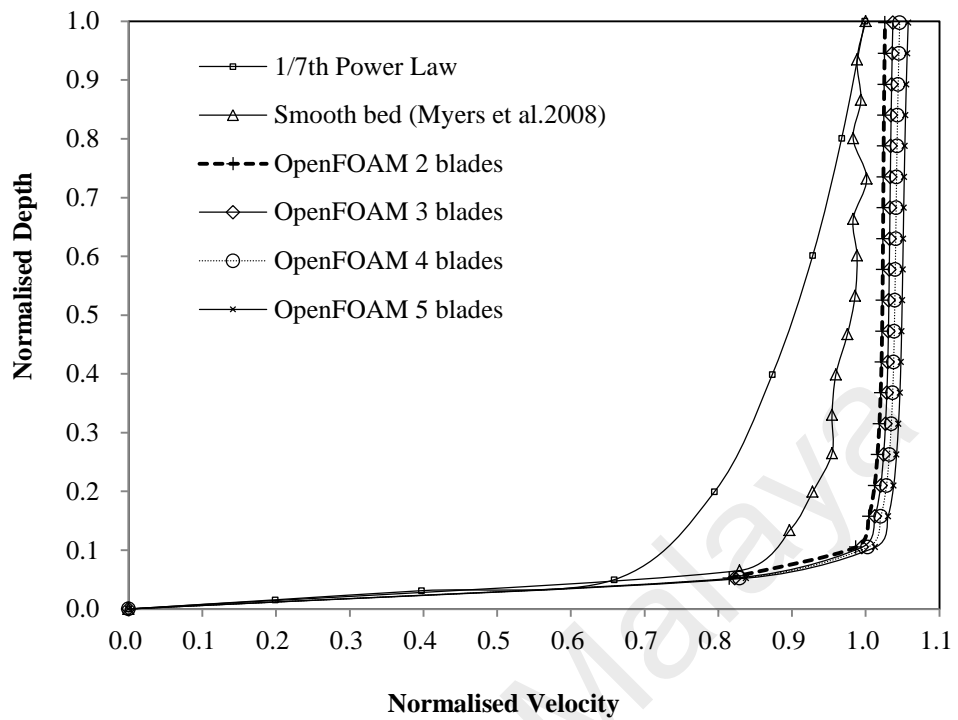
Figure 4.16: The development of boundary layer behind turbine rotors

4.3.4 Validation of Numerical Results and Mesh Independence Study

Experimental results and numerical simulation by Pinon et al. (2010) for investigating wake of TCT were used in the study to validate the numerical model. The velocity profile at the location $1.2D_t$ behind the turbine was presented and compared with results obtained by Pinon et al. (See Figure 4.17). There is some variability in the region near the rotational axis. The cause of this disagreement might be the length of the hub. The computational results agree well with the experimental results of Pinon et al. (2010). Figure 4.17 also shows that the axial velocity under turbine blades experienced a slight increase.
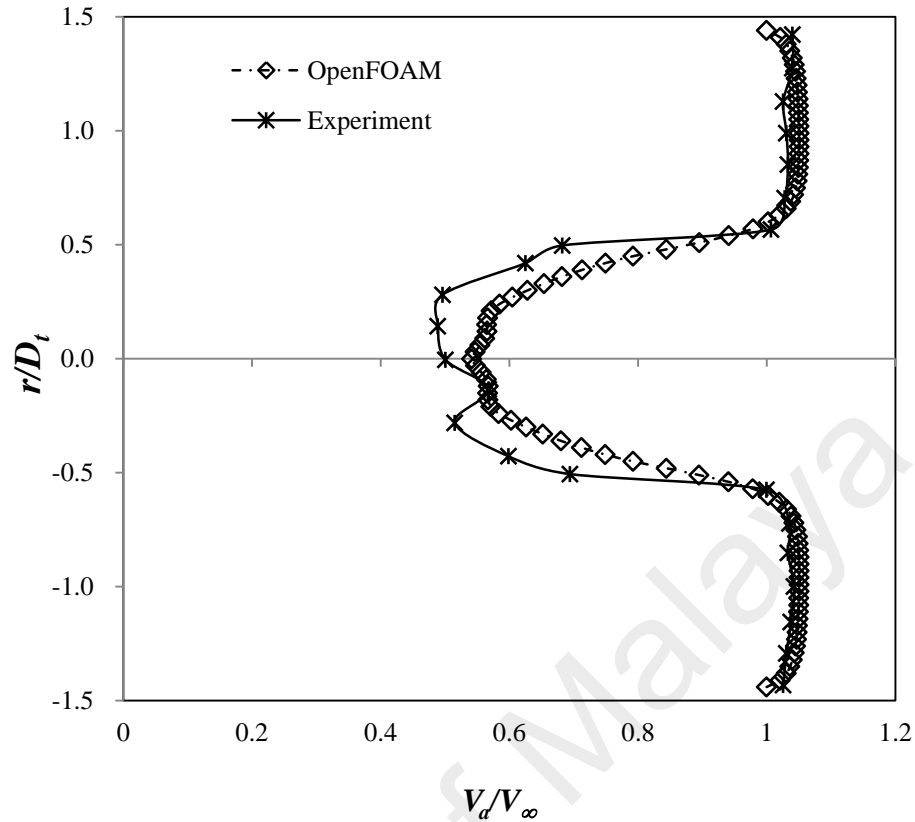
Figure 4.17: Axial velocity profiles behind turbine blades ($x=1.2D_t$)

The number of cells in CFD can influence the results due to the approximations and time-averaging method used in RANS equations (Daly et al., 2013). A greater number of cells may result in a more accurate solution for the problem with a specified numerical setting. The increase in mesh density also requires more computational power. The mesh independence study attempts to investigate the velocity field accurately with less processing time.

The computational case with a three-bladed turbine was selected and the mesh independence study incorporated the turbine in the numerical simulation with finer meshes. The cell numbers were increased to 545757 and 655908 cells. The mesh independence was tested by selecting axial velocity at the layer $0.5C$ from the bed (C=350mm). The results obtained by using a finer mesh give no discernible changes in

the predicted flow field (see Figure 4.18). The results of velocity magnitude are in good

agreement for both fine and coarse meshes. A mesh density of 451039 cells is used for

the investigation, which has the advantage of less processing time.
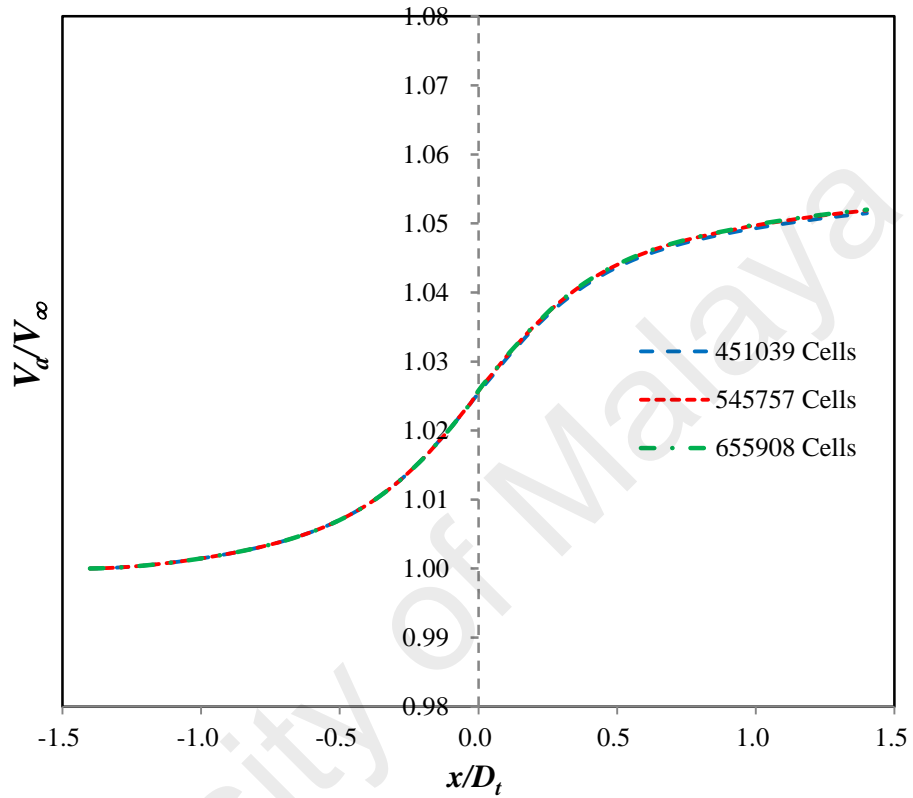
Figure 4.18: Mesh independence study

4.4 Scour Nature of TCT

4.4.1 Spatial Scour Profile

The final bed topography from the clear water scour tests is shown in Figure 4.19. It aims to investigate the effect of rotor tip clearance on the sediment transport around the support of the TCT. During the test, no sediment transport occurred at the upstream, confirming clear water scour conditions and local scour and deposition induced by the TCT. The scour induced by the TCT of the three cases has the similar pattern. Sediment around the support is eroded and a hole is formed. Sediment eroded from the scour region was deposited behind in a hill shaped dune. The maximum scour depth reached 18% of rotor diameter (5 cm tip clearance), D_t, or 7% of the flow depth, H. Results also indicate that regions susceptible to scour typically persist up to $0.5D_t$ downstream and up to $0.5D_t$ to either side of the turbine support centre. The peak of the deposition reached the elevation of 10% of the rotor diameter.
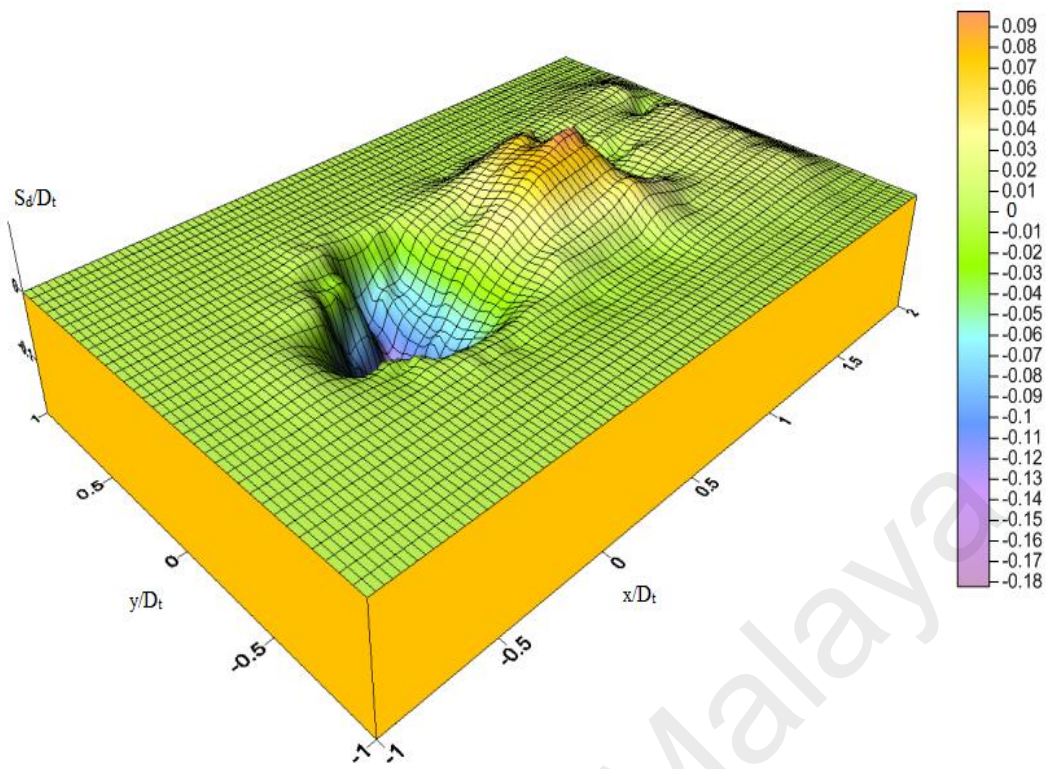
a. 5 cm tip clearance
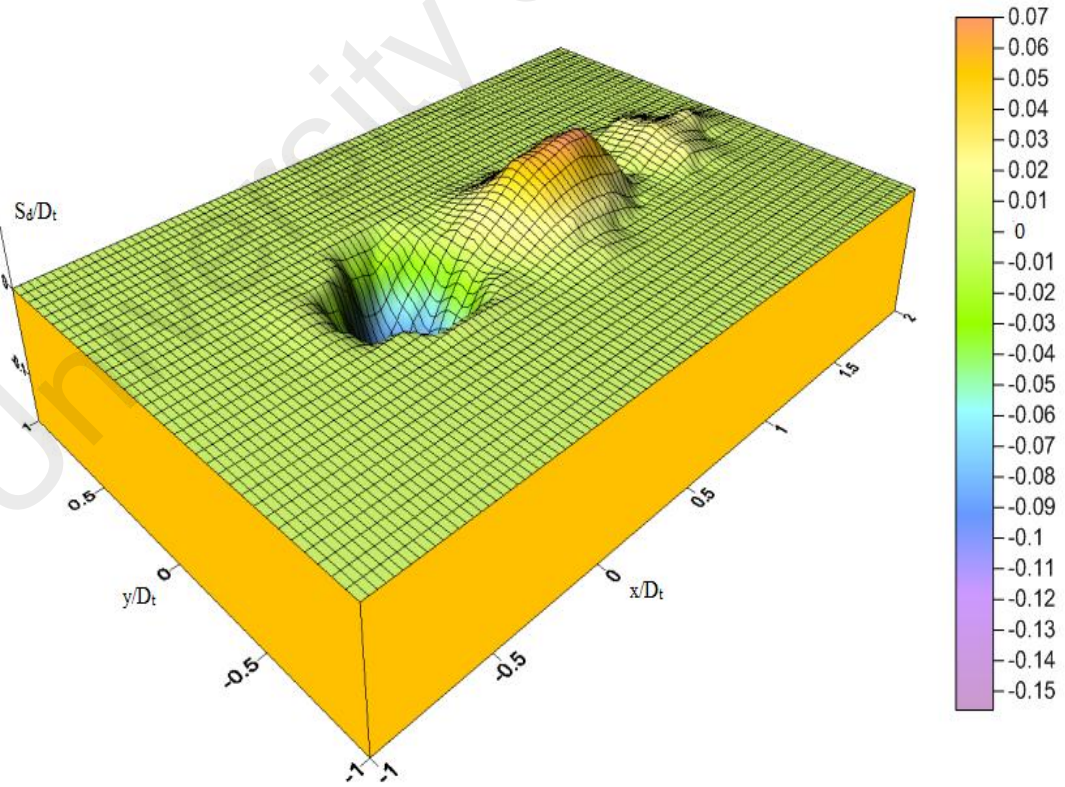
b. 10 cm tip clearance

Figure 4.19: 3D surface map of 24-hr scour by SURFER
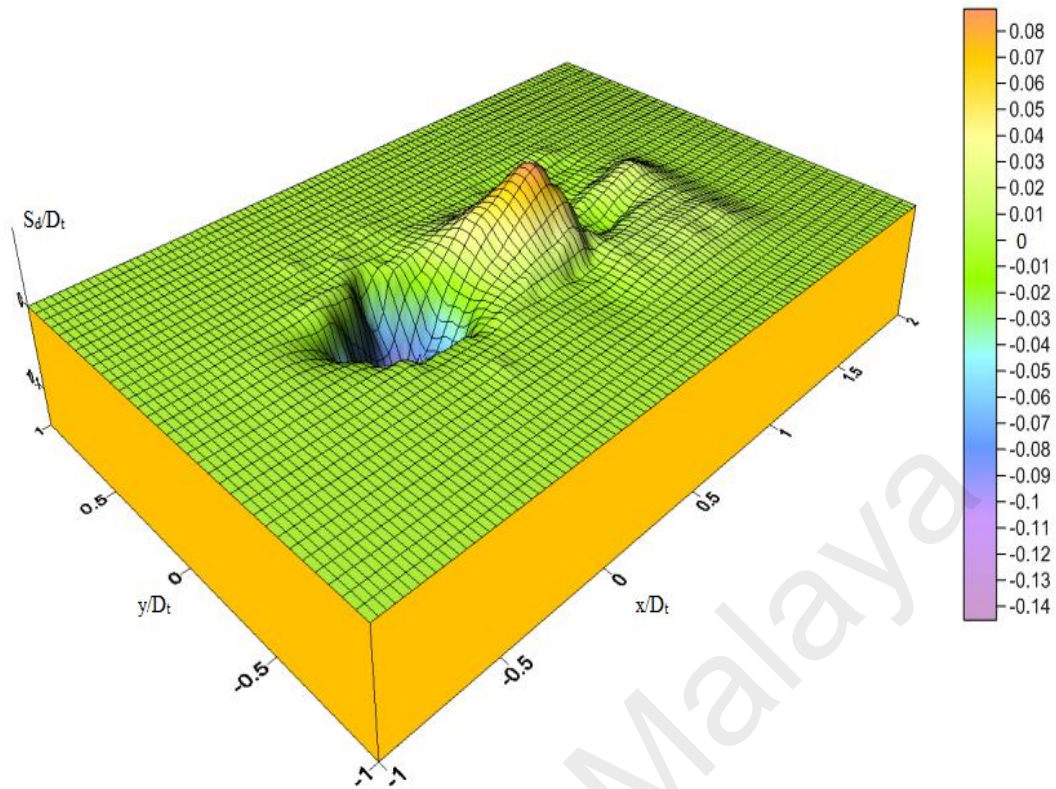
c. 15 cm tip clearance

Figure 4.19, continued.

As discovered in Section 4.3, the obstruction induced by the spinning rotor resulting acceleration of the flow between the bottom rotor tip and bed surface. This acceleration increases the local shear stress and it amplifies the scour mechanism. It is therefore the short tip clearance (5 cm) can cause severe sediment transport around the support of the TCT. The extent of scour hole increases with the decrease of tip clearance. The highest tip clearance 15 cm results in the least eroded sand from the bed. The scour holes and deposited sand are asymmetric particularly in the case of 5 cm tip clearance. It is due to asymmetric shear stress impacted at the bed. It conforms to the study conducted by Zhang et al. (2015).

4.4.2 Temporal Evolution

4.4.2.1 Temporal Variation of Scour Profiles

Figures 4.20, 4.21 and 4.22 present the temporal dimensionless scour holes profile at 3.5, 7.0 and 24 hr. The turbine rotor places 5cm, 10cm and 15 cm from bed, respectively. The investigated cases are in the same manner in terms of scour development. Looking closely at the measured developments of scour profile at various lateral positions, it can be observed that a scour hole is formed around the support tower. The majority of scour occurred at the initial 3.5 hr. The size of scour holes increase with time. The scour depth slightly increases after 3.5 hr scour. A deposition mound is also observed downstream at initial stage. The depositional wedge also moves further downstream as the test in progress. A secondary sand dune is formed right behind the primary dune after 24 hr test.

At the case of 5 cm tip clearance, maximum scour occurred at approximately $x/D_t=$ -0.1, $y/D_t=$ -0.1, reached the depth of $S/D_t=0.185$. The highest depositional wedge reached elevations of approximately 10% of the D_t at location $x/D_t=1.0$, $y/D_t=0.1$. The highest secondary sand dune is only 3.5% of D_t at location $x/D_t=1.8$, $y/D_t= 0.2$. It is has been observed that there is no secondary sand dune at the first 7 hr scour test. It is probably due to the primary deposition wedge reached a certain height and it becomes susceptible to the flow below turbine rotor. The accelerated flow below rotor turbine eroded the deposited sand dune.

In the case of 10 cm tip clearance, maximum scour depth is approximately 16% of D_t and took place at $x/D_t= -0.05$, $y/D_t=0$ and $x/D_t=-0.05$, $y/D_t= -0.1$. The highest primary sand dune has an elevation of $0.075D_t$ and it happened after 7 hr scour test other than 24 hr. It may due to the primary scour dune deposition is less than its erosion in the subsequent test. The highest primary deposition located at the region of $x/D_t=0.6-0.7$, $y/D_t=0.0-0.1$. Secondary dune is also formed but with lower elevation. The highest secondary sand dune is only 3% of D_t at $x/Dt=1.5$, $y/D_t=0.0$.

For the investigated case of 15 cm tip clearance, maximum scour depth occurred at $x/D_t= -0.05$, $y/D_t=0$ and $x/D_t=-0.05$, $y/D_t= -0.1$ which is same as the case of 10 cm tip clearance. The maximum scour depth is approximate $0.145D_t$. The highest primary deposition is 8.5% of D_t located at $x/D_t= 0.7$, $y/D_t=0$ and $x/D_t=0.7$, $y/D_t= -0.1$. The secondary sand dune is getting lower and lower as the rotor of turbine rotor moves up. The highest secondary sand dune is only 2% of turbine diameter at locations $x/D_t= 1.2$, $y/D_t=0$ and $x/D_t=1.2$, $y/D_t= -0.1$.

As seen from all the investigated cases, it has been observed that the maximum scour depth increase as the decrease of tip clearance. The maximum scour depth occurred in front of the support pile. It is generally at the region $x/D_t=-0.05 - -0.1$ and $y/D_t=0.0 - -0.1$. The height of primary and secondary deposited sand dunes also increases as the decreases in tip clearance. The location of peak sand dune is a bit complicated due to the influence of the flow between turbine rotor and bed. Furthermore, the transition point between net erosion and net deposition moves downstream as the test ongoing. Hill et al. (2014) suggested that the transition point may reveal a

relationship between turbine wake and the bed surface. The transition points of Hill et al. (2014) are between x/D_t=1.0 to x/D_t=2.0. This region has been noted by Chamorro et al. (2013) and they claimed that the turbine wake coherence starts to break down in this region where the most rapid velocity deficit recovery begins. However, the furthest transition point of the current study located at x/D_t=0.5 in all the cases after 24 hr scour test. The difference of the locations of the transition point may be due to the difference of turbine geometry and flow velocity.

a.
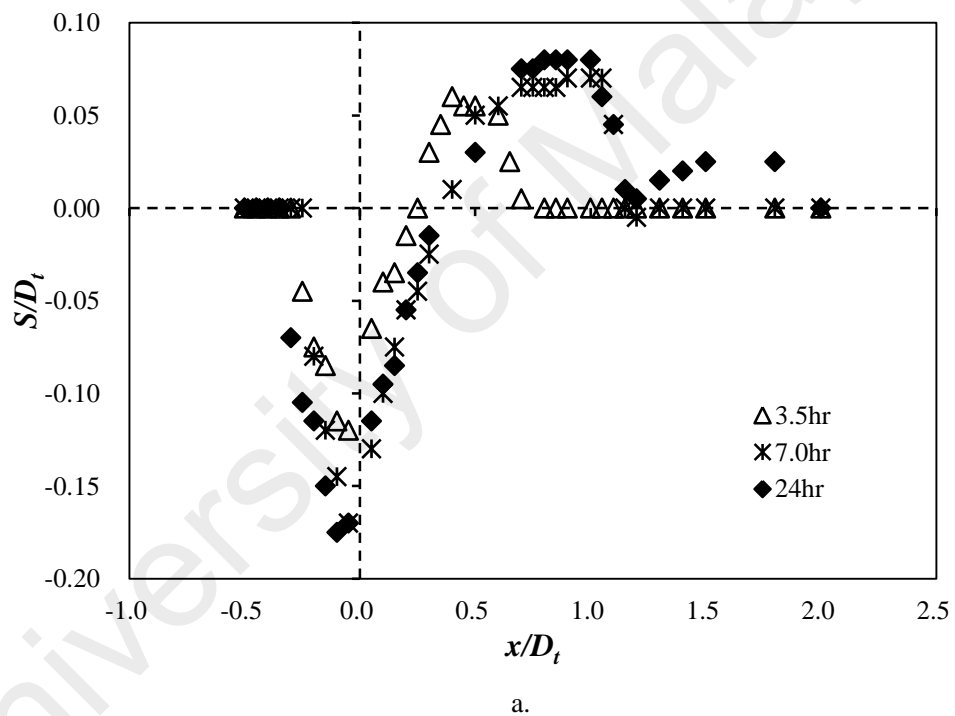
Figure 4.20: Temporal dimensionless scour holes profile at different times (Tip clearance=5 cm); a. $y/D_t = 0$; b. y/D_t= -0.1; c. $y/D_t = 0.1$. e. y/D_t= -0.2; f. $y/D_t = 0.2$.
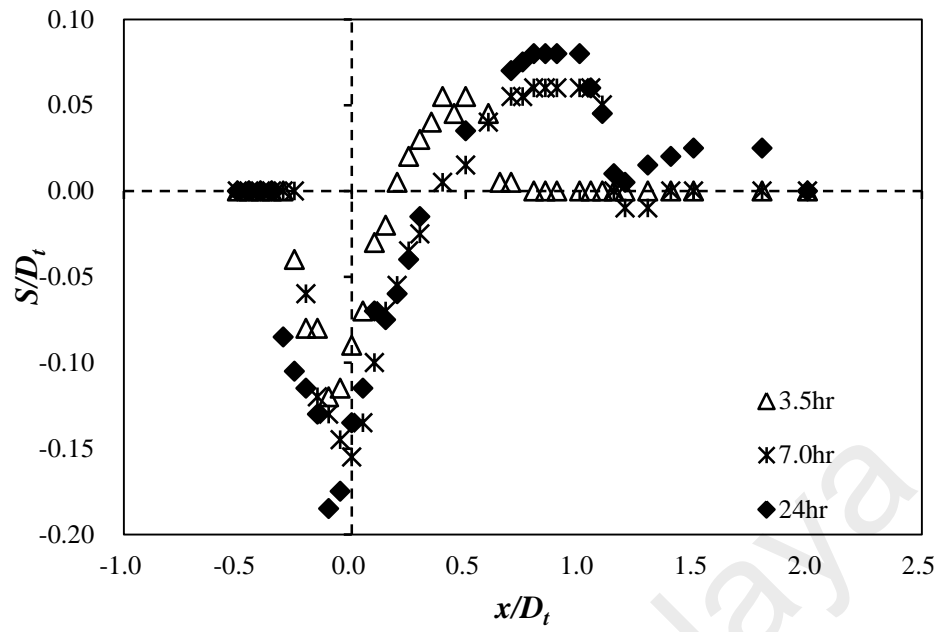
b.
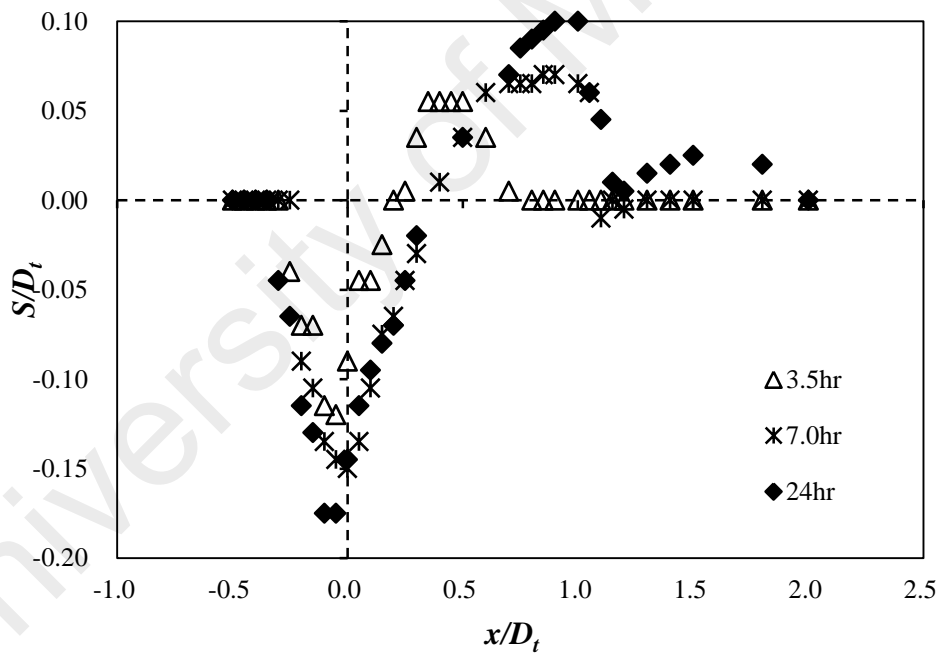
c.

Figure 4.20, continued.
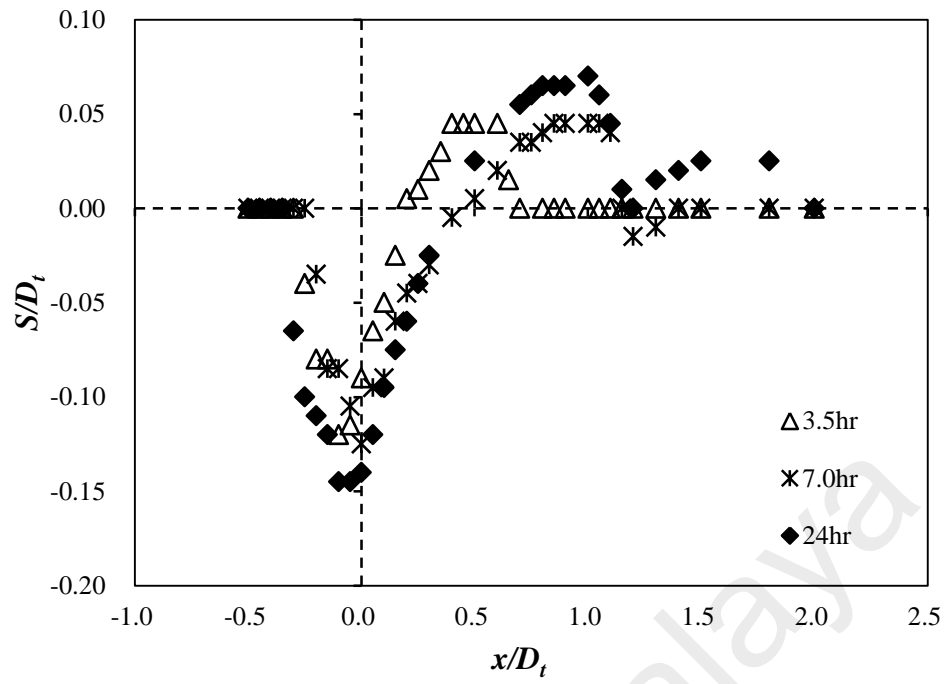
d.
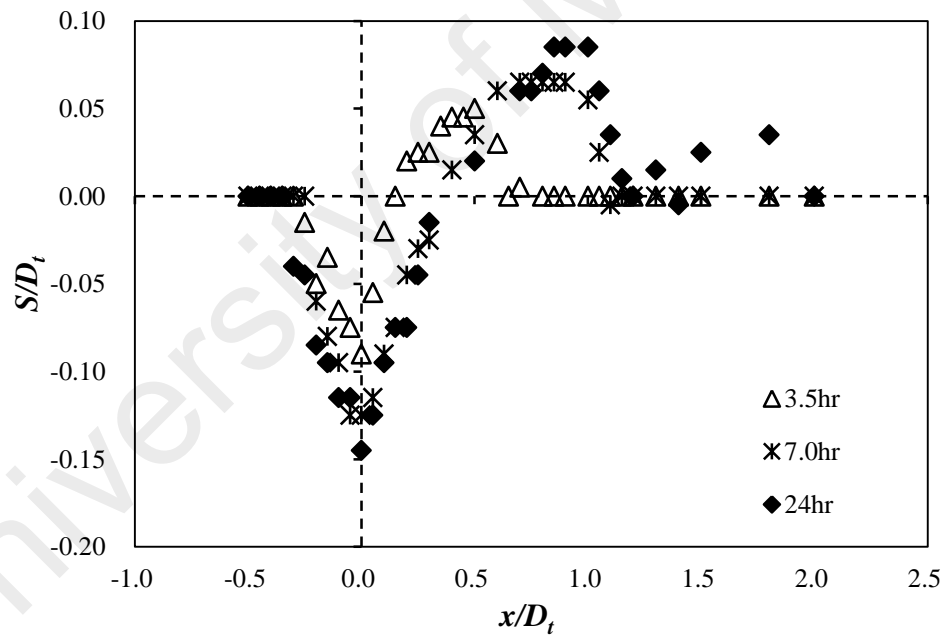
e.

Figure 4.20, continued.
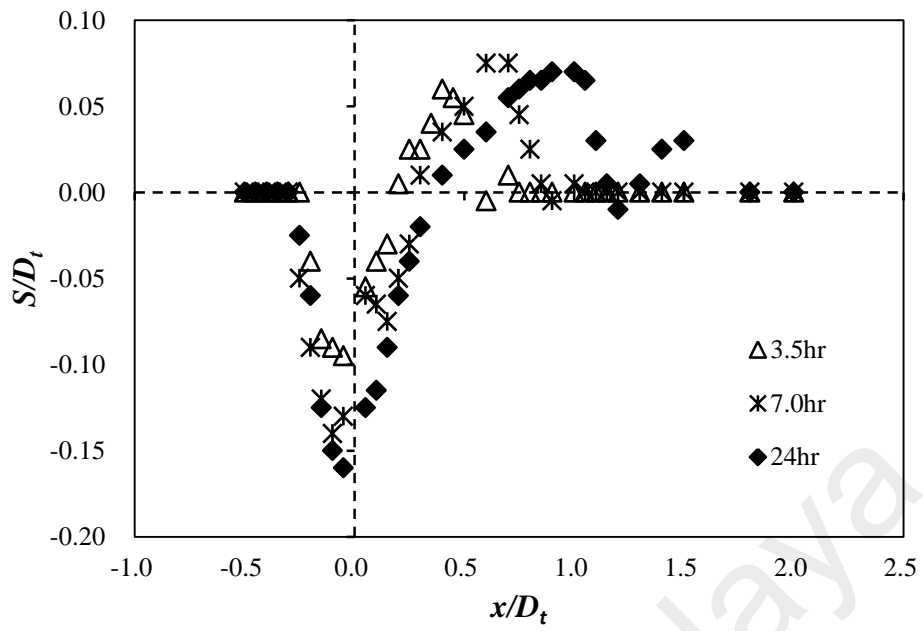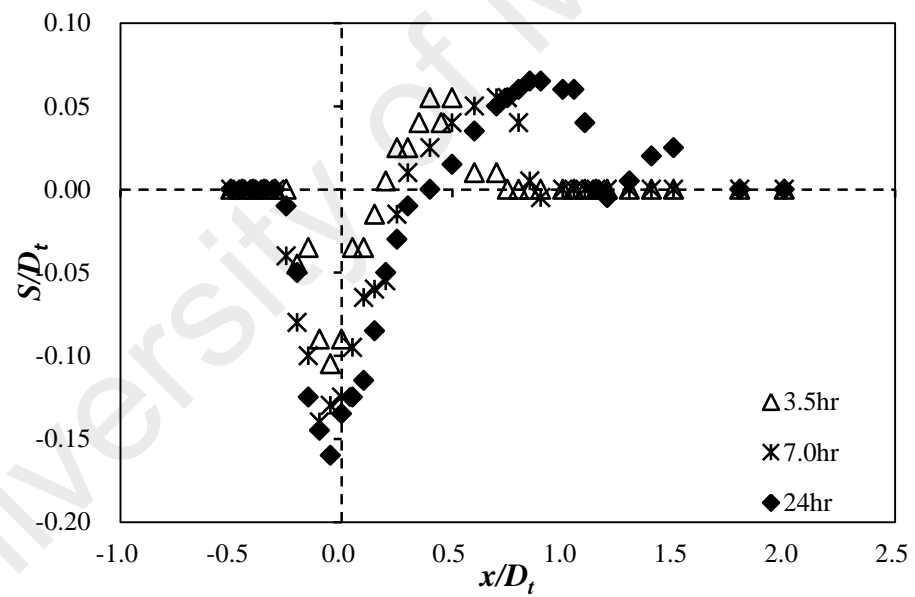
Figure 4.21: Temporal dimensionless scour holes profile at different times (Tip clearance=10 cm); a. $y/D_t = 0$; b. $y/D_t = -0.1$; c. $y/D_t = 0.1$. e. $y/D_t = -0.2$; f. $y/D_t = 0.2$.
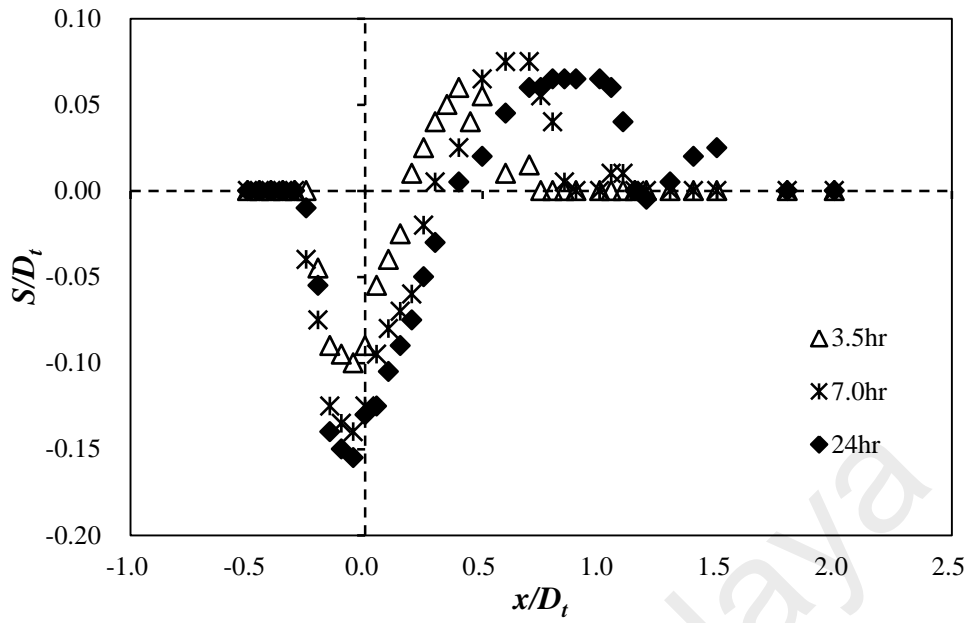
c.
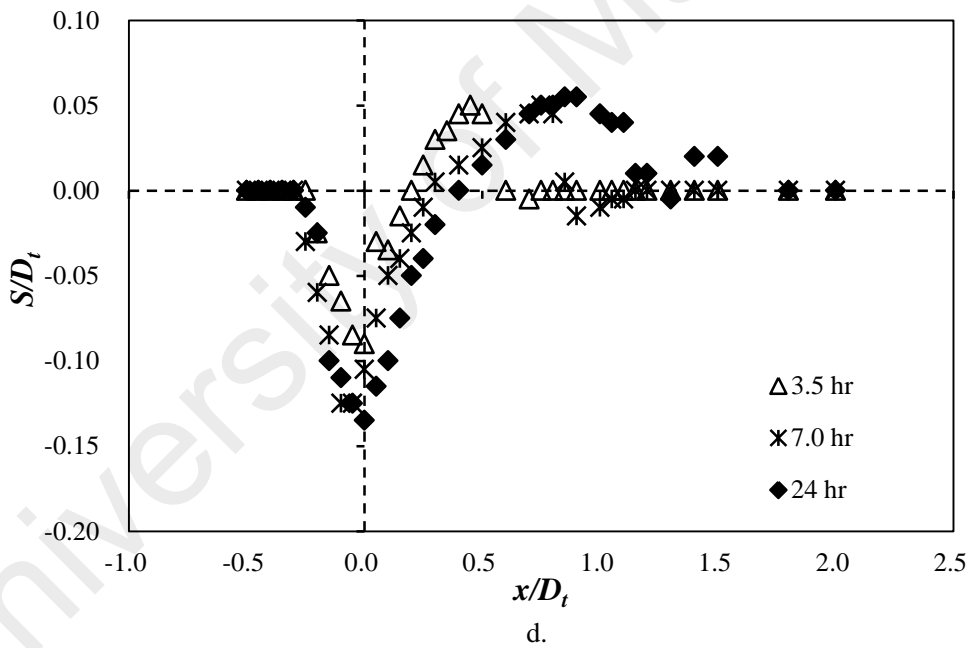
d.

Figure 4.21, continued.

134
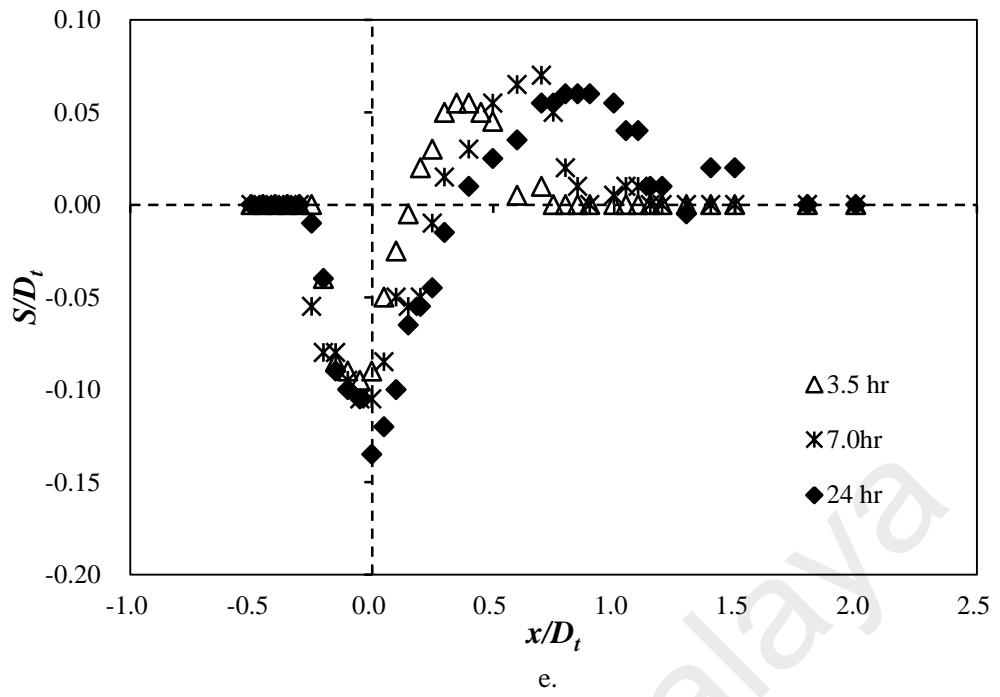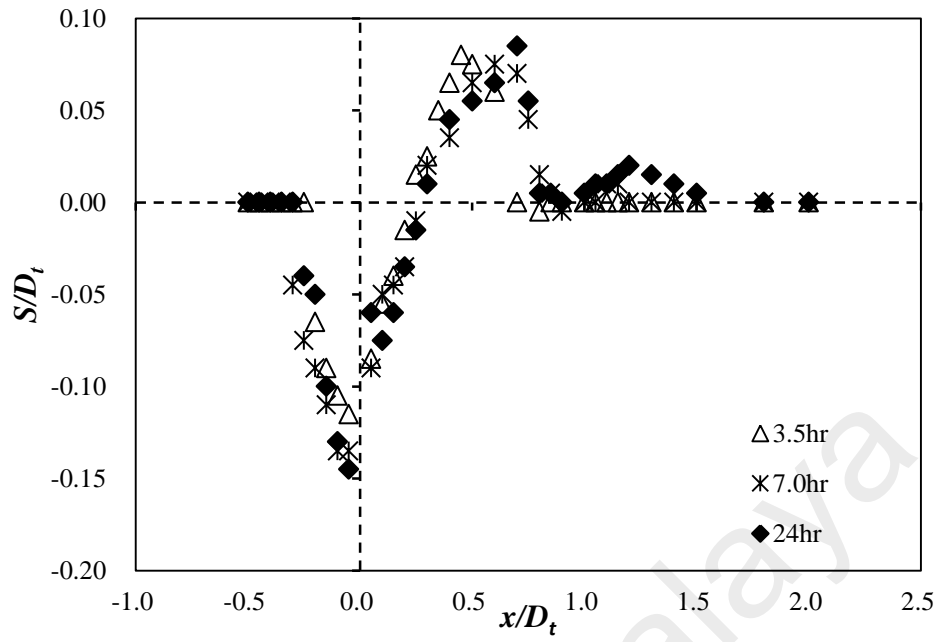
Figure 4.21, continued.
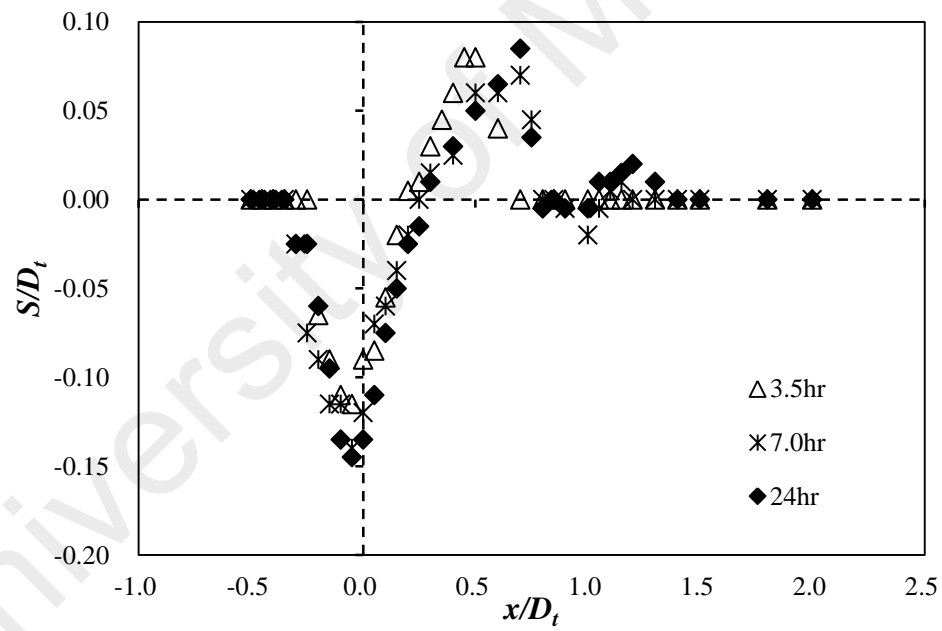
Figure 4.22: Temporal dimensionless scour holes profile at different times (Tip clearance=15cm); a. $y/D_t = 0$; b. $y/D_t = -0.1$; c. $y/D_t = 0.1$. e. $y/D_t = -0.2$; f. $y/D_t = 0.2$.
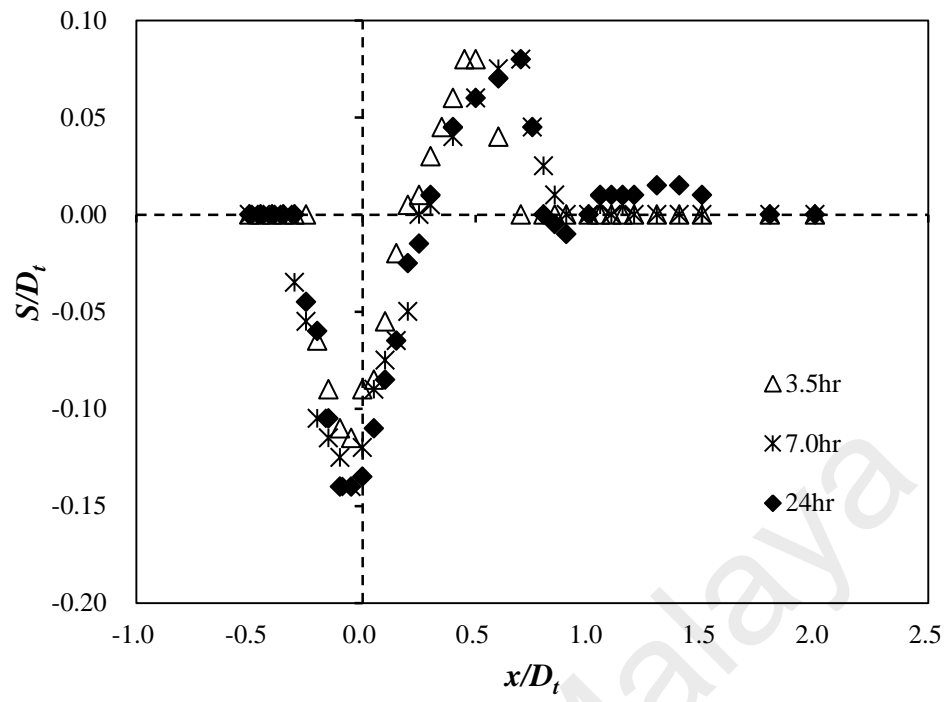
c.
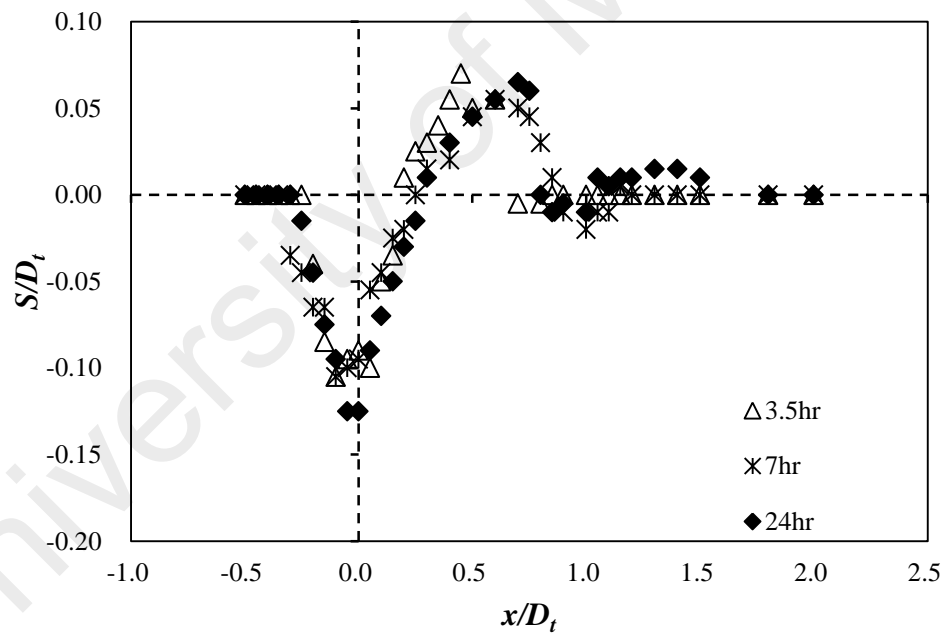
d.

Figure 4.22, continued.
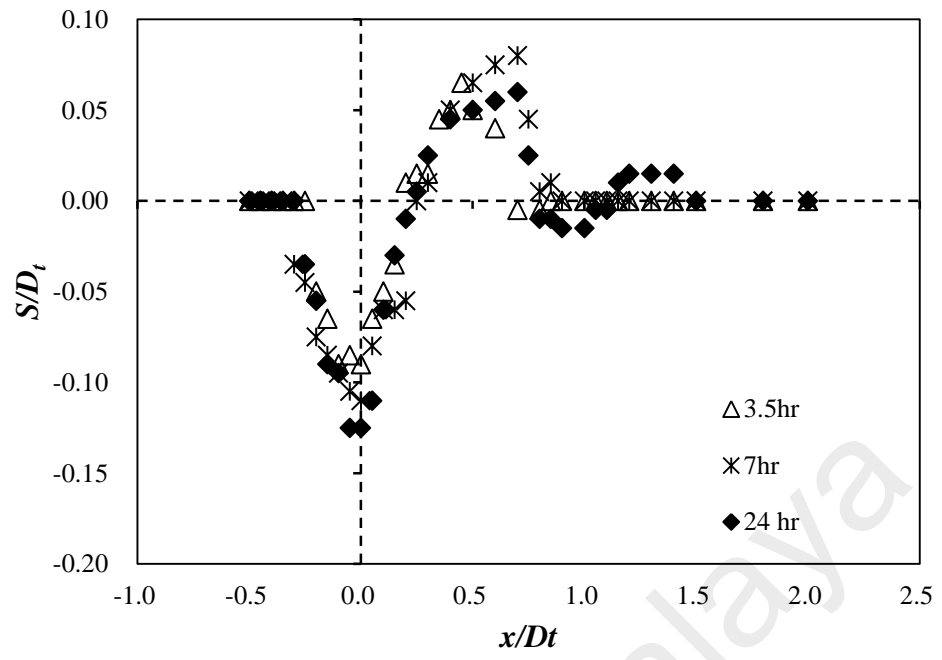
e.

Figure 4.22, continued.

4.4.2.2 Temporal Variation of Maximum Scour Depth

Figure 4.23 illustrates the temporal scour depth under different tip clearances. The S_t/D_t is a logarithmic function of time (t). It observed that the majority of the scour of all the investigated cases occurred in the first 3.5 hours. After 7 hr of scour test, all three cases reach near-equilibrium conditions. The depth of scour increased more quickly in the case with 5 cm tip clearance. The slowest scour occurred in the case of 15 cm tip clearance. The maximum scour also occurred in the case of 5cm tip clearance, which is approximately 18.5% of the rotor diameter D_t (8% of flow depth). The least scour happened in the case of 15 cm tip clearance, which is approximately 14% of the rotor diameter D_t (6% of flow depth).
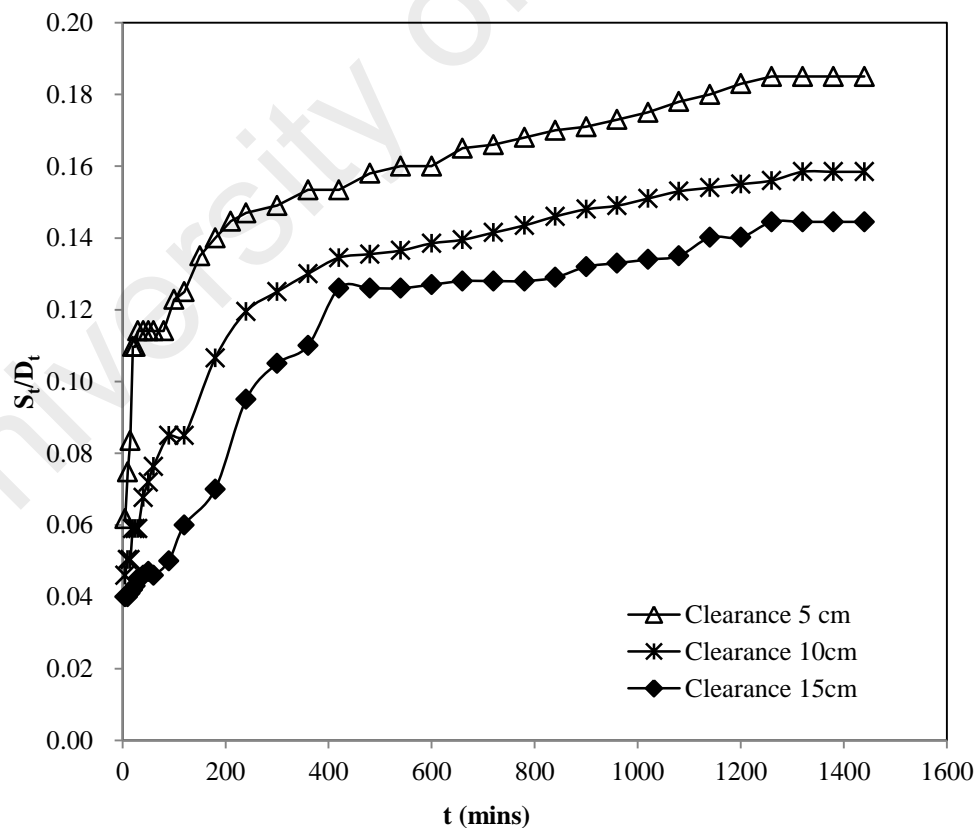
Figure 4.23: Time-dependent maximum scour depth

A comparison between the experimental results of the current study and Hill et al. (2014) of temporal scour depth is presented in Figure. 4.24. The time has been normalized by the respective velocity at hub height. It shows that the large-scale experiment did not approach equilibrium stage. The small-scale experiments approach the near-equilibrium. Hill et al. (2014) also indicated that the sour hole evolves faster when the rotor is on the upstream side of the support tower. The temporal evolution of scour depth of small-scale experiments indicated similar pattern with the author's results (C=5 cm), particularly the case of rotor upstream. The authors' experiments are conducted with rotor upstream. The results of Hill et al. (2014) in Fig.10 are taken from x/D_t=0.66 and y/D_t=0 for all cases. The results of current study are taken from x/D_t=-0.1 and y/D_t=-01. These locations are on the downstream side of the rotors. With the rotor on the downstream of the support tower, the flow acceleration between rotor and seabed may take place later. The scour amplification occurs potentially further downstream from the support tower. The location of rotor plays an important role for the scour mechanism of tidal turbine. The development of wake of the turbine affects the scour mechanism. The prediction of wake profile is able to provide insightful inputs for the scour prediction around the support of TCT.

The temporal evolution of scour hole for large-scale experiment is relatively faster compare to small-scale experiments. However, it should be noted that the velocity at hub height is 0.66 m/s. This indicated the incoming flow velocity plays a significant role on the temporal evolution of scour hole. The size of the rotor may also cause the faster evolution of scour hole as the large-scale experiment with a 0.5 m diameter rotor.
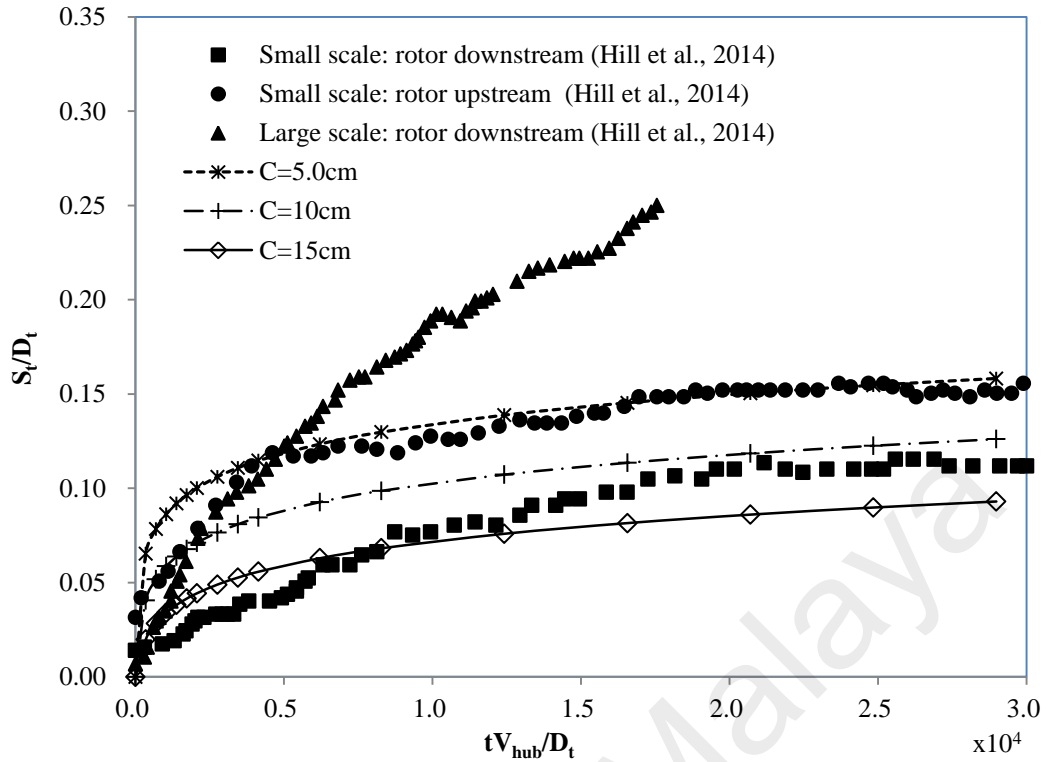
Figure 4.24: Comparison of temporal scour depth

4.4.2.3 Proposed Scour Prediction Model

Research to provide methods for predicting scour depth around the pile-supported structure of tidal turbine is limited. The maximum scour depth at any time t, S_t, is assumed to be a function of 10 independent variables as follows:

$$S_t = f_1(V_0, D_t, d_{50}, C, \rho, \rho_s, g, H, v, t) \tag{4.6}$$

In the works of ship propeller jet induced scour (Rajaratnam, 1981; Hamill, 1999; Hong et al., 2013), the fluid viscosity could be neglected as the Reynolds number of the jet is greater than 10,000. The Reynolds number of the wake induced by the physical model of the turbine is around 29,100. The viscosity term is ignored in the following analysis. The water depth of the study is reasonable high, the Froude number is

approximately 0.11 and its effects on scour are not examined in the study. The efflux velocity is calculated from $V_0 = V_\infty\sqrt{1 - C_t}$ (Equation 3.10), as introduced in Section 3.1. By referencing the work of Hong et al. (2014), the Buckingham π theorem has been applied and choosing ρ, g, V_0 as fundamental variables. Equation (4.6) has been obtained as the follows:

$$\frac{gS_t}{V_0^2} = f_2\left(\frac{gD_t}{V_0^2}, \frac{gd_{50}}{V_0^2}, \frac{gC_0}{V_0^2}, \frac{\rho}{(\rho_s - \rho)}, \frac{gt}{V_o}\right) \tag{4.7}$$

Based on experience of ship propeller jet induced scour (Hamill, 1999; Hong et al., 2013) and re-arrange the above equation, the maximum depth of scour hole could be written as:

$$\frac{S_t}{D_t} = f_2\left(F_o, \frac{C}{D_t}, \frac{C}{d_{50}}, \frac{t}{D_t/V_o}\right) \tag{4.8}$$

In Equation (4.7), $F_o = V_o / \sqrt{\left(\frac{\rho_s - \rho}{\rho}\right)gd_{50}}$ and D_t/V_o, which is denoted by t_R, is the proposed time scale. A nonlinear regression analysis has been performed and an empirical equation for the estimation of time-dependent scour depth of the pile-supported TCT is proposed as:

$$\frac{S_t}{D_t} = k_1\left[log_{10}\left(\frac{V_o t}{D_t}\right) - k_2\right]^{k_3} \tag{4.9}$$

where

$$k_1 = 0.01\left(\frac{C}{D_t}\right)^{-0.405}\left(\frac{C}{d_{50}}\right)^{0.009}F_0^{0.443}$$

$$k_2 = 1.9\left(\frac{C}{D_t}\right)^{1.67}\left(\frac{C}{d_{50}}\right)^{0.009}F_0^{-0.009}$$

$$k_3 = 2.18\left(\frac{C}{D_t}\right)^{0.19}\left(\frac{C}{d_{50}}\right)^{-0.04}F_0^{-0.05}$$

Figure 4.25 presents the overall comparison between the computed and observed temporal maximum scour depth. The R-squared value ranges from 0.7747 to 0.9737. The best fitting of the experimental data with predicted value is in the case C=10 cm. The lowest R-squared value in the case of C=15 cm is 0.7747 which is still consider very good based on Henriksen et al. (2003). Equation 4.9 has good agreement with present experimental data under the conditions of $0.25 \leq C/D_t \leq 0.75$, $50 \leq C/d_{50} \leq 150$ and $F_0 = 1.8965$. More experimental results are necessary to enlarge the applicable range of the proposed model.
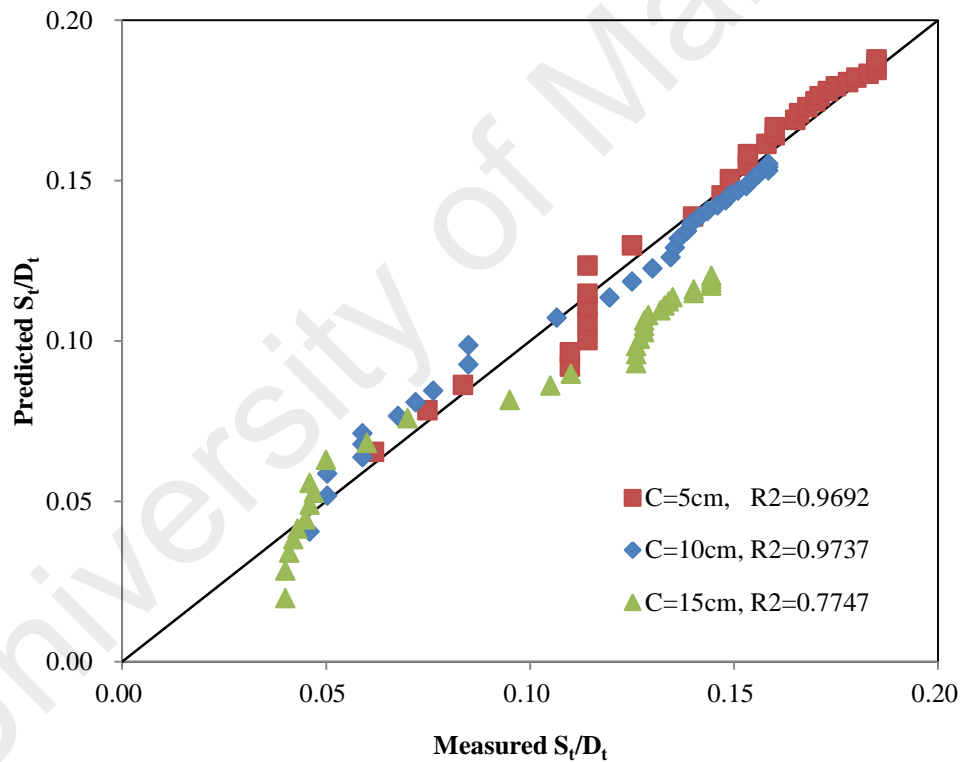
Figure 4.25: Comparison between measured and predicted time-dependent scour depth

4.4.3 Comparison with Conventional Bridge/Pile Scour

The presence of rotor adds complexity to the scour induced by the pile-supported TCT. The scour mechanism of the TCT is different from the conventional bridge/pile scour. The main differences come from the generated wake and the flow below the wake. The flow below wake tends to move faster than the free stream and may act to amplify the scour process which results in the increase of the scour rate. The study showed that the tip clearance (vertical location) of rotor affects the scour depth around the support of the TCT which is line with Zhang et al. (2015). Figure 4.24 also indicated that the lateral location of the rotor affects the scour profile of tidal turbine. The proposed efflux velocity is employed for the prediction of time-dependent scour depth. The prediction of wake profiles provides initial input for the scour profile prediction.

The turbine geometry may also affect the scour process. This is because of the geometry affects the flow between rotor and seabed. As presented in section 4.3.2, the number of blades affects the axial and radial component of velocity. The study of Hill et al. (2014) also stated that the scour process of TCT depends on geometrical properties of turbine rotor. They also highlighted that the device performance may affect the scour mechanism.

The flow characteristic of a river stream is significantly different from tidal variations. River flow is unidirectional and it may have strong stochastic variation on daily to seasonal base (Khan et al., 2009). The tides undergo fluctuations of dominant periodic nature. The tide is either diurnal or semidiurnal. Many sites are relatively bi-directional. The flow reversal can be 20° or more away from 180° (Myers and Bahaj,

2005; Blunden and Bahaj, 2006; Haydar et al., 2012). The scour test performed in the study is under the case of unidirectional flow. The study of Escarameia and May (1999) and McGovern (2014) reported that the equilibrium scour depth is smaller than the case under unidirectional flows due to backfilling of scour hole during reversing flow. In the site of relatively bi-directional flow, the predicted scour rate and depth by using proposed scour model is probably larger than the real case. The conservative feature of the proposed model safeguards the stability of the support of TCTs. The proposed model is based on the reference guide of ship propeller jets induced scour. The scour process of TCTs is complicated due to the presence of the rotor. The attempts by referencing ship propeller jet induced scour predictor is promising and the proposed model (Equation 4.9) can be used as a starting point for future model development.

CHAPTER 5: CONCLUSIONS AND RECOMMENDATIONS

5.1 Conclusions

The main purposes of the thesis were to study the flow nature of turbine wake and to explore the impacts of turbine wake on the seabed. The conclusions of the research objectives listed in Section 1.3 are addressed in the following:

5.1.1 Analytical Wake Model

The validity of the analytical wake model is demonstrated. It is able to predict the two-dipped wake structure. Two-dipped wake model is able to predict the two axisymmetric minimum velocities within the zone of flow establishment compared to the equations of Lam and Chen (2014). The two minimum velocities merged to be one minimum velocity in the zone of established flow. The proposed model is also able to predict the wake model under various ambient turbulence conditions (TI=3%, 5%, 8% and 15%). The analytical wake model is documented in Table 4.2.

The procedure to predict the wake structure is summarised. Prediction of the wake structure is started by predicting the efflux velocity. Efflux velocity is able to be predicted using the enhanced equation V_o (Equation 3.10) to predict the minimum velocities at various positions from the turbine depending on the turbulence intensity. Goodness-of-fit analysis has been conducted by comparing with published experimental data. The estimator of R-square (R2) and Mean Square Error (MSE) indicated that the predicted wake stricture has acceptable agreement with the published experimental results.

5.1.2 Flow between Rotor and Bed

OpenFOAM is able to predict the velocity profile under the rotor of the TCT. The axial component is the largest contributor to the magnitude of the velocity. The radial component of the velocity is the second largest contributor to the magnitude of the velocity. The tangential component is insignificant so that it suggests the tangential component of velocity has no impact on the scour and deposition process. The confinement has no effect on the velocity pattern of each velocity component when the tip clearance is large enough.

The blockage ratio of TCT is directly proportional to the extent of flow acceleration. The presence of rotor changes the boundary layer profile subsequently results in the altering of horseshoe vortex formation. A schematic diagram to describe the flow profile between seabed and TCT has been proposed (Figure 4.8). The blockage ratio of a TCT is directly proportional to the extent of flow acceleration. A higher blade area ratio of turbine cause more velocity deficit right behind the turbine plane. A higher blade area ratio causes higher velocity acceleration around the turbine rotors. A larger blade area ratio also results in higher radial velocity in the near-field of the turbine. The change of tangential velocity was found to be insignificant due to change of blade area ratio.

The characterization of the flow conditions offers the preliminary insight into the interaction between the turbine and the ambient environment. The geometry of the turbine is of importance to the flow. The study demonstrates the possibility of OpenFOAM as a promising method to investigate TCT related issue. The height of tip clearances and turbine geometry are the two critical parameters in scour design of TCT.

5.1.3 Tip Clearance on the Scour Depth of Pile-Supported TCT

The presence of rotor amplifies the scour process around the support of the TCT. The decrease of tip clearance increases the scour depth. The maximum scour depth reached 18.5% of the rotor diameter. Results indicate that regions susceptible to scour typically persist up to $1.0D_t$ downstream and up to $0.5D_t$ to either side of the turbine support centre.

The tip clearance plays the most important role in affecting the scour depth and scour rate. The case of 5 cm tip clearance results in the fastest scour and most sediment transport, while the case of 15 cm tip clearance has the slowest and least sediment transport.

5.1.4 Temporal Scour Profiles of Pile-Supported TCT

Majority of the scour occurred in the first 3.5 hr in all the cases. The scour depths of all the cases reach near-equilibrium state after 7 hr test. A "V" shape scour hole is formed around the support tower. A deposition mound is also observed downstream at initial stage. The primary deposition mound moves further downstream with time. A secondary dune is formed right behind the primary dune after 24 hr of scour test.

5.1.5 Correlation of the Tip Clearance with Time-Dependent Maximum Scour Depth

Using the experimental data, the S_t/D_t is a logarithmic function of time. An empirical formula (Equation 4.9) to estimate the time-dependent maximum scour depth is proposed as the following:

$$\frac{S_t}{D_t} = k_1 [log_{10} \left(\frac{V_o t}{D_t}\right) - k_2]^{k_3}$$

where

$$k_1 = 0.01 \, (\frac{C}{D_t})^{-0.405} (\frac{C}{d_{50}})^{0.009} F_0^{\,0.443}$$

$$k_2 = 1.9 \, (\frac{C}{D_t})^{1.67} (\frac{C}{d_{50}})^{0.009} F_0^{\,-0.009}$$

$$k_3 = 2.18 \, (\frac{C}{D_t})^{0.19} (\frac{C}{d_{50}})^{-0.04} F_0^{\,-0.05}$$

Equation 3.10 (Efflux velocity) is an initial input for the proposed scour prediction. The predicted results indicate acceptable agreement with the present experimental data.

5.2 Recommendations for Future Works

Though large amount of works has been done to understand the wake and scour of TCT, the scope of this work is limited. Recommendations for future research are listed as follows:

I. The wave may affeect the turbine performance and wake structure. The effect of wave on the wake would need to be studied

II. Field measurements of turbine wake profile can be done.

III. The applicability of the porposed turbine wake model can be testified when the incoming flow is non-uniform.

IV. Higher resolution of numerical model can be conducted to capture the detail flow near turbine rotor.

V. Further research can be carried out to cover a wider range of densimetric Froude number for the scour prediction around the support of TCT. For instance, different incoming velocity and various sediment sizes.

VI. More attention should be drawn to the scour nature of TCT under live-bed condition.

VII. The effect of the wave on the scour depth of TCT can be investigated.

VIII. The scour rate of TCT under bi-directional flow condition can be examined.

IX. The investigation on scour profile of TCT under tide and wave combined condition needs be carried out.

X. The interations of turbines may affect the scour mechanisms. The investigation of scour of TCT in arrays needs to be investigated.

REFERENCES

Aberle, J., & Söhngen, B. (2008). Analysis of propeller jet induced scours. In *International Conference on Fluvial Hydraulics River Flow* (pp. 3-5).

Albertson, M. L., Dai, Y. B., Jensen, R. A., & Rouse, H. (1950). Diffusion of submerged jets. *Transactions of the American Society of Civil Engineers*, *115*(1), 639-664.

Annandale, G. (2005). *Scour technology: mechanics and engineering practice*. McGraw Hill Professional.

Ansari, S. A., & Qadar, A. (1994). Ultimate depth of scour around bridge piers. In *Hydraulic Engineering (1994)* (pp. 51-55). ASCE.

Atlantis Resource. 16th, Jan, 2015, from http://atlantisresourcesltd.com/turbines/ar-series/ar1000.html

Bahaj, A. S. (2011). Generating electricity from the oceans. *Renewable and Sustainable Energy Reviews*, *15(7)*, 3399-3416.

Bahaj, A.S., Batten, W.M.J., & McCann, G. (2007). Experimental verification of numerical predictions for the hydrodynamic performance of horizontal axis marine current turbines. *Renewable Energy*, *32 (15)*, 2479-2490.

Bahaj, A. S., Myers, L. E., Thomson, M. D., & Jorge, N. (2007, September). Characterising the wake of horizontal axis marine current turbines. *In Proceedings of the 7th European wave and tidal energy conference* (p. 9).

Baker, C. J. (1979a). The laminar horseshoe vortex. *Journal of fluid mechanics, 95(02)*, 347-367.

Baker, C. J. (1979b). *Vortex flow around the bases of obstacles* (Doctoral dissertation, University of Cambridge). Retrieved from https://www.repository.cam.ac.uk/handle/1810/244806

Barkdoll, B. D., Ettema, R., & Melville, B. W. (2007). *Countermeasures to protect bridge abutments from scour* (Vol. 587). Transportation Research Board.

Bastankhah, M., & Porté-Agel, F. (2014). A new analytical model for wind-turbine wakes. *Renewable Energy*, *70*, 116-123.

Batten, W. M., Harrison, M. E., & Bahaj, A. S. (2013). Accuracy of the actuator disc-RANS approach for predicting the performance and wake of tidal turbines. *Philosophical Transactions of the Royal Society of London A: Mathematical, Physical and Engineering Sciences, 371(1985)*, 20120293.

Berger, W., FelKel, K., Hager, M., Oebius, H., & Schale, E. (1981, June). Courant provoque par les bateaux protection des berges et solution pour eviter l'erosion du lit du haut rhin. In *PIANC, 25th Congress, Section I-1. Edinburgh*.

Blaauw, H. G., & Van de Kaa, E. J. (1978). *Erosion of bottom and sloping banks caused by the screw race of manoevring ships* (pp. 1-12). Delft Hydraulics.

Blunden, L. S., & Bahaj, A. S. (2006). Initial evaluation of tidal stream energy resources at Portland Bill, UK. Renewable Energy, 31(2), 121-132.

Breusers, H.N.C., Raudkivi, A.J. (1991). *Scouring*. Balkema, Rotterdam.

Bryden, I.G., Naik, S., Fraenkel, P., Bullen, C.R. (1998). Matching tidal current plants to local flow conditions. *Energy*, *23 (9)*, 699-709.

Brewster, P.M. (1997). *Modelling the wash from a ship's propeller*. (Unpublished doctoral dissertation). University of Queen's Belfast, Northern Ireland.

Breusers, H. N. C., Nicollet, G., & Shen, H. W. (1977). Local scour around cylindrical piers. *Journal of Hydraulic Research*, *15(3)*, 211-252.

Breusers, H. N. C., & Raudkivi, A. J. (1991). Scouring, hydraulic structures design manual. *IAHR, AA Balkema, Rotterdam*, *143*.

Builtjes, P. J. H. (1978). The interaction of windmill wakes. *In 2nd international symposium on wind energy systems* (Vol. 1, p. 5).

Camporeale, S.M., & Magi, V. (2000). Stream tube model for analysis of vertical axis variable pitch turbine for marine currents energy conversion. *Energy Conversion and Management*, *41(16)*, 1811-1827.

Chamorro, L. P., Hill, C., Morton, S., Ellis, C., Arndt, R. E. A., & Sotiropoulos, F. (2013). On the interaction between a turbulent open channel flow and an axial-flow turbine. *Journal of Fluid Mechanics*, *716*, 658-670.

Chamorro, L. P., Troolin, D. R., Lee, S. J., Arndt, R. E. A., & Sotiropoulos, F. (2013). Three-dimensional flow visualization in the wake of a miniature axial-flow hydrokinetic turbine. *Experiments in fluids, 54(2)*, 1-12.

Chong, H., & Lam, W. (2013). Ocean renewable energy in Malaysia: The potential of the straits of Malacca. *Renewable and Sustainable Energy Reviews*, *23*, 169-178.

Copping, A., Battey, H., Brown-Saracino, J., Massaua, M., & Smith, C. (2014). An international assessment of the environmental effects of marine energy development. *Ocean & Coastal Management, 99*, 3-13.

Daly, T., Myers, L. E., & Bahaj, A. S. (2013). Modelling of the flow field surrounding tidal turbine arrays for varying positions in a channel. *Philosophical Transactions of the Royal Society of London A: Mathematical, Physical and Engineering Sciences*, *371(1985)*, 20120246.

Den Boon, J. H., Sutherland, J., Whitehouse, R., Soulsby, R., Stam, C. J. M., Verhoeven, K. Verhoeven, M. Høgedal., & Hald, T. (2004, November). Scour behaviour and scour protection for monopile foundations of offshore wind turbines. In *Proceedings of the European Wind Energy Conference* (Vol. 14).

De Vos, L., De Rouck, R., Troch, P., & Frigaard, P. (2011). Empirical design of scour protections around monopile foundations Part 1: Static approach. *Coastal Engineering*, *58*, 540-533.

Dixen, M., Lohmann, I. P., & Christensen, E. D. (2012). Method to predict long time span of scour around offshore wind turbine foundations. *Coastal Engineering Proceedings*, *1(33)*, 88.

Escarameia, M., & May, R. W. P. (1999). Scour around structures in tidal flows. Retrieved from: http://eprints.hrwallingford.co.uk/706/2/SR521-Scour-structures-tidal-flows-HRW allingford.pdf

Fraenkel, P. L. (2002). Power from marine currents. *Proceedings of the Institution of Mechanical Engineers, Part A: Journal of Power and Energy*, *216*(1), 1-14.

Fraenkel, P. L. (2007). Marine current turbines: pioneering the development of marine kinetic energy converters. *Proceedings of the Institution of Mechanical Engineers, Part A: Journal of Power and Energy*, *221*(2), 159-169.

Gaythwaite, J. W. (2004). *Design of marine facilities for the berthing, mooring, and repair of vessels* (No. 2nd Edition).

Gebreslassie, M. G., Tabor, G. R., & Belmont, M. R. (2013). Numerical simulation of a new type of cross flow tidal turbine using OpenFOAM–Part I: Calibration of energy extraction. *Renewable Energy*, *50*, 994-1004.

Goodness-of-fit Statistics. Retrieved 9th Oct, 2014. Retrieved from http://web.maths.unsw.edu.au/~adelle/Garvan/Assays/GoodnessOfFit.html

Hamill, G.A. (1987). *Characteristics of the screw wash of a maneuvering ship and resulting bed scour.* (Unpublished doctoral dissertation). Queen's University of Belfast, Northern Ireland.

Hamill, G. A., Johnston, H. T., & Stewart, D. P. (1999). Propeller wash scour near quay walls. *Journal of waterway, port, coastal, and ocean engineering, 125(4)*, 170-175.

Hamill, G. A., McGarvey, J. A., & Hughes, D. A. B. (2004). Determination of the efflux velocity from a ship's propeller. *Proceedings of the ICE-Maritime Engineering*, *157*(2), 83-91.

Hamill, G. A., McGarvey, J. A., & Hughes, D. A. B. (2004, June). Determination of the efflux velocity from a ship's propeller. In *Proceedings of the Institution of Civil Engineers-Maritime Engineering* (Vol. 157, No. 2, pp. 83-91). Thomas Telford Ltd.

Hashim, H., & Ho, W.S. (2011). Renewable energy policies and initiatives for a sustainable energy future in Malaysia. *Renewable and Sustainable Energy Reviews*, *15*, 4870-4887.

Hashimi, H.N. (1993). *Erosion of a granular bed at a quay wall by a ship's screw wash*. (Unpublished doctoral dissertation). Queen's University of Belfast, Northern Ireland.

Harris, J., Whitehouse, R. J. S., & Benson, T. (2010). The time evolution of scour around offshore structures. *ICE-Maritime Engineering*, *163(1)*, 3-17.

Harrison, M. E., Batten, W. M. J., Myers, L. E., & Bahaj, A. S. (2010). Comparison between CFD simulations and experiments for predicting the far wake of horizontal axis tidal turbines. *IET Renewable Power Generation*, *4*(6), 613-627.

Hassan, U. (1993). *A wind tunnel investigation of the wake structure within small wind turbine farms*. Harwell Laboratory, Energy Technology Support Unit.

Hassan, H.F., El-Shafie, A., & Karim. O.A. (2012). Tidal current turbines glance at the past and look into future prospects in Malaysia. *Renewable and Sustainable Energy Reviews*, *16*, 5707-5717.

He, L., Kinnas, S. A., & Xu, W. (2011, January). Numerical methods for the prediction of unsteady performance of marine propellers and current turbines. In *The Twenty-first International Offshore and Polar Engineering Conference*. International Society of Offshore and Polar Engineers.

Henriksen, H. J., Troldborg, L., Nyegaard, P., Sonnenborg, T. O., Refsgaard, J. C., & Madsen, B. (2003). Methodology for construction, calibration and validation of a national hydrological model for Denmark. *Journal of Hydrology, 280(1)*, 52-71.

Higuera, P., Lara, J. L., & Losada, I. J. (2013). Simulating coastal engineering processes with OpenFOAM®. *Coastal Engineering*, *71*, 119-134.

Hill, C., Musa, M., Chamorro, L. P., Ellis, C., & Guala, M. (2014). Local scour around a model hydrokinetic turbine in an erodible channel. *Journal of Hydraulic Engineering*, *140(8)*, 04014037.

Hoffmans, G.J.C.M., & Verheij, H.J. (1997). *Scour Manual.* Balkema, Rotterdam.

Hong, J. H., Chiew, Y. M., & Cheng, N. S. (2013). Scour caused by a propeller jet. *Journal of Hydraulic Engineering*, *139(9)*, 1003-1012.

International Energy Agency (IEA). (2013). *World Energy Outlook*. London.

Jensen, N. O. (1983). A note on wind turbine interaction. Risoe National Laboratory, *Roskilde, Denmark, Technical Report No. M-2411.*

Jo, C. H., Lee, J. H., Rho, Y. H., & Lee, K. H. (2014). Performance analysis of a HAT tidal current turbine and wake flow characteristics. Renewable Energy, 65, 175-182.

Julien, P. Y., Ruff, J. F., & Ji, U. (2006). *Alternative designs of pier-scour protection for the Gupo and Subway Bridge on the Lower Nakdong River.*

Kang, S., Borazjani, I., Colby, J. A., & Sotiropoulos, F. (2012). Numerical simulation of 3D flow past a real-life marine hydrokinetic turbine. *Advances in water resources*, *39*, 33-43.

Khan, M. J., Bhuyan, G., Iqbal, M. T., & Quaicoe, J. E. (2009). Hydrokinetic energy conversion systems and assessment of horizontal and vertical axis turbines for river and tidal applications: A technology status review. *Applied Energy*, *86(10)*, 1823-1835.

Lam, W.H., & Chen, L. (2014). Equations used to predict velocity distribution within a wake from a horizontal axis tidal current turbine. *Ocean Engineering*, *79*, 35-42.

Lam, W. H., Hamill, G.A., Robinson, D., & Raghunathan, S. (2010). Observations of the initial 3D flow from a ship's propeller. *Ocean Engineering*, *37(14)*, 1380-1388.

Lam, W. H., Hamill, G.A., Robinson, D., Raghunathan, S., & Song, Y. (2012a). Analysis of the 3D zone of flow establishment from a ship's propeller. *KSCE Journal of Civil Engineering*, *16(4)*, 465-477.

Lam, W.H., Hamill, G.A., Song, Y.C., Robinson, D.J., & Raghunathan, S. (2011). A review of the equations used to predict the velocity distribution within a ship's propeller jet. *Ocean Engineering*, *38*, 1–10.

Lam, W. H., Robinson, D. J., Hamill, G. A., Zhao, J. F., & Jia, M. (2012b). Time-averaged velocity and turbulence intensity at the initial downstream flow from a six-bladed ship propeller. *Ocean Engineering*, *51*, 85-93.

Lam, W. H., Robinson, D. J., Hamill, G. A., & Johnston, H. T. (2012c). An effective method for comparing the turbulence intensity from LDA measurements and CFD predictions within a ship propeller jet. Ocean Engineering, 52, 105-124.

Launder, B. E., & Spalding, D. B. (1972). Lectures in mathematical models of turbulence.

Liu, P. (2010). A computational hydrodynamics method for horizontal axis turbine–Panel method modeling migration from propulsion to turbine energy. *Energy, 35(7)*, 2843-2851.

Lillycrop, W.J. & Hughes, S.A. (1993). *Scour Hole Problems Experienced by the Corps of Engineers: Data presentation and Summary*, Vicksburg: CERC-93-2, US Army Engineer Waterways Experiment Station. Coastal Engineering Research Centre.

Lim, Y. S., & Koh, S. L. (2010). Analytical assessments on the potential of harnessing tidal currents for electricity generation in Malaysia. *Renewable Energy*, *35(5)*, 1024-1032.

Liu, X.F. (2008). *Numerical models for scour and liquefaction around object under currents and waves*. (Doctoral Thesis, University of Illinois at Urbana-Champaign).Retrieved from http://water.engr.psu.edu/liu/publications.html

MacEnri, J., Reed, M., & Thiringer, T. (2013). Influence of tidal parameters on SeaGen flicker performance. Philosophical Transactions of the Royal Society of London A: Mathematical, Physical and Engineering Sciences, 371(1985), 20120247.

Maganga, F., Germain, G., King, J., Pinon, G., & Rivoalen, E. (2010). Experimental characterisation of flow effects on marine current turbine behaviour and on its wake properties. *IET Renewable Power Generation*, *4*(6), 498-509.

McDougal, W. G., & Sulisz, W. (1989). Seabed stability near floating structures. *Journal of waterway, port, coastal, and ocean engineering*, *115*(6), 727-739.

McGarvey, J.A. (1996). *The influence of the rudder on the hydrodynamics and the resulting bed scour, of a ship's screw wash*. (Doctoral Dissertation, University of Queen's Belfast).

McGovern, D. J., Ilic, S., Folkard, A. M., McLelland, S. J., & Murphy, B. J. (2014). Time development of scour around a cylinder in simulated tidal currents. Journal of Hydraulic Engineering, 140(6), 04014014.

Melville, B. W. (1997). Pier and abutment scour: integrated approach. *Journal of Hydraulic Engineering*, *123(2)*, 125-136.

Melville, B.W., & Coleman, S.E. (2000). *Bridge Scour*. Water Resource Publication. CO, USA.

Mycek, P., Gaurier, B., Germain, G., Pinon, G., & Rivoalen, E. (2013). Numerical and experimental study of the interaction between two marine current turbines. *International Journal of Marine Energy*, *1*, 70-83.

Mycek, P., Gaurier, B., Germain, G., Pinon, G., & Rivolen, E. (2014). Experimental study of the turbulence intensity effects on marine current turbines behaviour. Part I: One single turbine. *Renewable Energy*, 66, 729-746.

Myers, L., & Bahaj, A. S. (2005). Simulated electrical power potential harnessed by marine current turbine arrays in the Alderney Race. Renewable Energy, 30(11), 1713-1731.

Myers, L., & Bahaj, A. S. (2007). Wake studies of a 1/30th scale horizontal axis marine current turbine. *Ocean Engineering*, 34(5), 758-762.

Myers, L.E., & Bahaj, A.S. (2010). Experimental analysis of the flow field around horizontal axis tidal turbines by use of mesh disk rotor simulators. *Renewable Energy*, *37*, 218-227.

Myers, L.E., & Bahaj, A.S. (2012). An experimental investigation simulating flow effects in first generation marine current energy converter arrays. *Renewable Energy*, *37*, 26-36.

Myers, L., Bahaj, A. S., Germain, G., & Giles, J. (2008, January). Flow boundary interaction effects for marine current energy conversion devices. In *World Renewable Energy Congress X, Glasgow, Juillet 2008*.

Neill, C. R. (1973). *Guide to bridge hydraulics*. Roads & Transportation Association of Canada.

Neill, S. P., Jordan, J. R., & Couch, S. J. (2012). Impact of tidal energy converter (TEC) arrays on the dynamics of headland sand banks. *Renewable Energy*, 37(1), 387-397.

Neill, S. P., Litt, E. J., Couch, S. J., & Davies, A. G. (2009). The impact of tidal stream turbines on large-scale sediment dynamics. *Renewable Energy*, 34(12), 2803-2812.

OES-IA Annual Report 2010 (2011). Implementing Agreement on Ocean Energy Systems. Lisbon, Portugal.

OES-IA Annual Report 2011 (2012). Implementing Agreement on Ocean Energy System. Lisbon, Portugal.

OES-IA Annual Report 2012 (2013). Implementing Agreement on Ocean Energy System. Lisbon, Portugal.

Olsen, N. R., & Melaaen, M. C. (1993). Three-dimensional calculation of scour around cylinders. *Journal of Hydraulic Engineering*, 119(9), 1048-1054.

OpenFOAM. 16th Jan, 2015. Retrieved from http://www.openfoam.com/

Pinon, G., Mycek, P., Germain, G., & Rivoalen, E. (2012). Numerical simulation of the wake of marine current turbines with a particle method. *Renewable Energy*, *46*, 111-126.

Prosser, M. J. (1986). *Propeller induced scour.* BHRA, Fluid Engineering Centre.

Raaijmakers, T., & Rudolph, D. (2008, November). Time-dependent scour development under combined currents and waves conditions-laboratory experiments with online monitoring technique. In *Proc. 4th Int. Conf. Scour Erosion, ICSE, Tokyo* (pp. 152-161).

Rajaratnam, N. (1981). Erosion by plane turbulent jets. *Journal of hydraulic Research*, *19(4)*, 339-358.

Rambabu, M., Rao, S. N., & Sundar, V. (2003). Current-induced scour around a vertical pile in cohesive soil. *Ocean Engineering*, *30*(7), 893-920.

Richardson, E.V., & Davis, S.R. (2001). Evaluating scour at bridges (4th ed.). Washington, D.C.: *Hydraulic Engineering Circular No.18 (HEC-18), Federal Highway Administration.*

Rocks, L., & Runyon, R.P. (1972). *The Energy Crisis.* New York: Crown Publishers.

Roulund, A., Sumer, B. M., Fredsøe, J., & Michelsen, J. (2005). Numerical and experimental investigation of flow and scour around a circular pile. *Journal of Fluid Mechanics,* 534, 351-401.

Rourke, F. O., Boyle, F., & Reynolds, A. (2010). Marine current energy devices: current status and possible future applications in Ireland. *Renewable and Sustainable Energy Reviews*, *14*(3), 1026-1036.

Rudolph, D., Bos, K. J., Luijendijk, A. P., Rietema, K., & Out, J. M. M. (2004, November). Scour around offshore structures–analysis of field measurements. In *Proceedings 2nd International Conference on Scour and Erosion* (pp. 14-17).

Rudolph, D., Raaijmakers, T. C., & De Sonneville, B. (2009, September). Challenges and recent advances in offshore scour modelling. In *12th International Conference The Jack-Up Platform–Design, Construction and Operations, London* (pp. 15-16).

Sakmani, A. S., Lam, W. H., Hashim, R., & Chong, H. Y. (2013). Site selection for tidal turbine installation in the Strait of Malacca. *Renewable and Sustainable Energy Reviews*, *21*, 590-602.

Sforza, P. M., Stasi, W., Smorto, M., & Sheerin, P. (1979, January). Wind turbine generator wakes. *In AIAA, Aerospace Sciences Meeting* (Vol. 1).

Shields, M.A., Woolf, D.K., Grist, E.P.M., Kerr, S.A., Jackson, A.C., Harris R.E., … Jonathan, S. (2011). Marine renewable energy: the ecological implications of altering the hydrodynamics of the marine environment. *Ocean and Coastal Management*, *54*, 2-9.

Simons, R., Weller, J., & Whitehouse, R. J. S. (2009). Scour development around truncated cylindrical structures. In Proceedings of the 5th Coastal Structures Conference, CSt07 (Vol. 2, pp. 1881-1890). World Scientific Publishing.

Stallard, T., Collings, R., Feng, T., & Whelan, J. I. (2011, September). Interactions between tidal turbine wakes: experimental study of a group of 3-bladed rotors. In *Proceedings of 9th European Wave and Tidal Energy Conference* (EWTEC2011) (pp. on-CD).

Stallard, T., Collings, R., Feng, T., & Whelan, J. (2013). Interactions between tidal turbine wakes: experimental study of a group of three-bladed rotors. *Philosophical Transactions of the Royal Society of London A: Mathematical, Physical and Engineering Sciences*, *371(1985)*, 20120159.

Stewart, D.P.J. (1992). *Characteristics of a ships screw wash and the influence of Quay wall proximity*. (Doctoral dissertation, Queen's University of Belfast).

Sumer, B.M. (2007) Mathematical modelling of scour: A review. *Journal of Hydraulic Research*, 45(6), 723-735.

Sumer, B. M., & Fredsøe, J. (2001). Scour around pile in combined waves and current. *Journal of Hydraulic Engineering*, *127*(5), 403-411.

Sumer, B. M., & Fredsøe, J. (2002). *The mechanics of scour in the marine environment*. World Scientific.

Sumer, B. M., Fredsøe, J., & Christiansen, N. (1992). Scour around vertical pile in waves. *Journal of waterway, port, coastal, and ocean engineering*.

Sumer, B. M., Petersen, T. U., Locatelli, L., Fredsøe, J., Musumeci, R. E., & Foti, E. (2012). Backfilling of a scour hole around a pile in waves and current. *Journal of Waterway, Port, Coastal, and Ocean Engineering, 139(1)*, 9-23.

Sun, X. (2008). *Numerical and experimental investigation of tidal current energy extraction*. (Doctoral dissertation, The University of Edinburg). Retrieved from https://www.era.lib.ed.ac.uk/handle/1842/2756

Tedds, S. C., Owen, I., & Poole, R. J. (2014). Near-wake characteristics of a model horizontal axis tidal stream turbine. *Renewable Energy*, 63, 222-235.

Transportation Association of Canada. (2004). *Guide to bridge hydraulics*. Thomas Telford.

Verhey, H. (1900, January). The stability of bottom and banks subjected to the velocities in the propeller jet behind ships. In *8th International Harbour Congress.*

Versteeg, H. K., & Malalasekera, W. (2007). *An introduction to computational fluid dynamics: the finite volume method*. Pearson Education.

Vermeulen, P. E. J., & Builtjes, P. J. H. (1982). *Turbulence Measurements in Simulated Wind-Turbine Clusters.* Hoofdgroep Maatschappelijke Technologie TNO.

Vybulkova, L. (2013). *A study of the wake of an isolated tidal turbine with application to its effects on local sediment transport* (Doctoral dissertation, University of Glasgow). Retrieved from http://theses.gla.ac.uk/4997/

Wang, D., Atlar, M., & Sampson, R. (2007). An experimental investigation on cavitation, noise, and slipstream characteristics of ocean stream turbines. *Proceedings of the Institution of Mechanical Engineers, Part A: Journal of Power and Energy*, *221*(2), 219-231.

Watchorn, M., Trapp, T., Sayigh, A.A.M. (2000). Tidal stream renewable offshore power generation. *World Renewable Energy Congress VI*. Oxford: Pergamon. 2664-667.

Whitehouse, R. J. S. (2006). Scour at coastal structures. *In: Third International Conference on Scour and Erosion, 1-3 November, Amsterdam,* The Netherlands.

Whitehouse, R. (1998). *Scour at marine structures: A manual for practical applications*. Thomas Telford.

Williams, G.E. (2000). Geological constraints on the Precambrian history of Earth's rotation and the Moon's orbit. *Reviews of Geophysics*, *38*, 37-59.

Wu, W., & Wang, S. S. (1999). Movable bed roughness in alluvial rivers. *Journal of Hydraulic Engineering*, 125(12), 1309-1312.

Xia, J.Q., Falconer, R.A., & Lin, B. (2010). Impact of different tidal renewable energy projects on the hydrodynamic processes in the Severn Estuary, UK. *Ocean Modelling*, *32*, 86-104.

Zanke, U. C., Hsu, T. W., Roland, A., Link, O., & Diab, R. (2011). Equilibrium scour depths around piles in noncohesive sediments under currents and waves. *Coastal Engineering*, *58(10)*, 986-991.

Zhang, J., Gao, P., Zheng, J., Wu, X., Peng, Y., & Zhang, T. (2015). Current-induced seabed scour around a pile-supported horizontal-axis tidal stream turbine. *Journal of Marine Science and Technology*, *23(6)*, 929-936.

Zhao, M., Cheng, L., & Zang, Z. (2010). Experimental and numerical investigation of local scour around a submerged vertical circular cylinder in steady currents. *Coastal Engineering, 57(8)*, 709-721.

LIST OF PUBLICATIONS AND PAPERS PRESENTED

Publications:

Chen, L., & Lam, W.H., (2014). Slipstream between marine current turbine and seabed, *Energy*, 68, 801-810. (ISI-Cited)

Lam, W.H., & **Chen, L**., (2014). Equations used to predict the velocity distribution within a wake from horizontal axis tidal current turbine, *Ocean Engineering*, 79, 35-42. (ISI-Cited)

Chen, L., & Lam, W.H., (2014). Methods for predicting seabed scour around marine current turbine. *Renewable and Sustainable Energy Reviews*, 29, 683-692. (ISI-Cited)

Lam, WH., **Chen, L**. & Hashim, R. (2015). Analytical wake model of tidal current turbine, *Energy*, 79, 512-521. (ISI-Cited)

Chen, L., & Lam, W.H. (2015). A review of survivability and remedial actions of tidal current turbine. *Renewable and Sustainable Energy Reviews*, 43, 891-900. (ISI-Cited)

Papers Presented:

Chen, L., Lam, W.H., & Shamsuddin, A.H. (2013). Potential scour of marine current turbine based on experience of offshore wind turbine. *IOP Conference Series: Earth and Environmental Science 16.* (Scopus-Cited)

Chen, L., & Lam, W.H. (2014). Scour prediction of tidal-current turbine: inclusion of flow field generated by rotor.   *2nd Asian Wave and Tidal Energy Conference, 28-31, July, Tokyo*.